International Journal of Aerospace Engineering

Heat Transfer and Flow Dynamics in Advanced Propulsion Systems

Lead Guest Editor: Jian Liu
Guest Editors: Bengt Sunden, Yiheng Tong, and Qingfei Fu

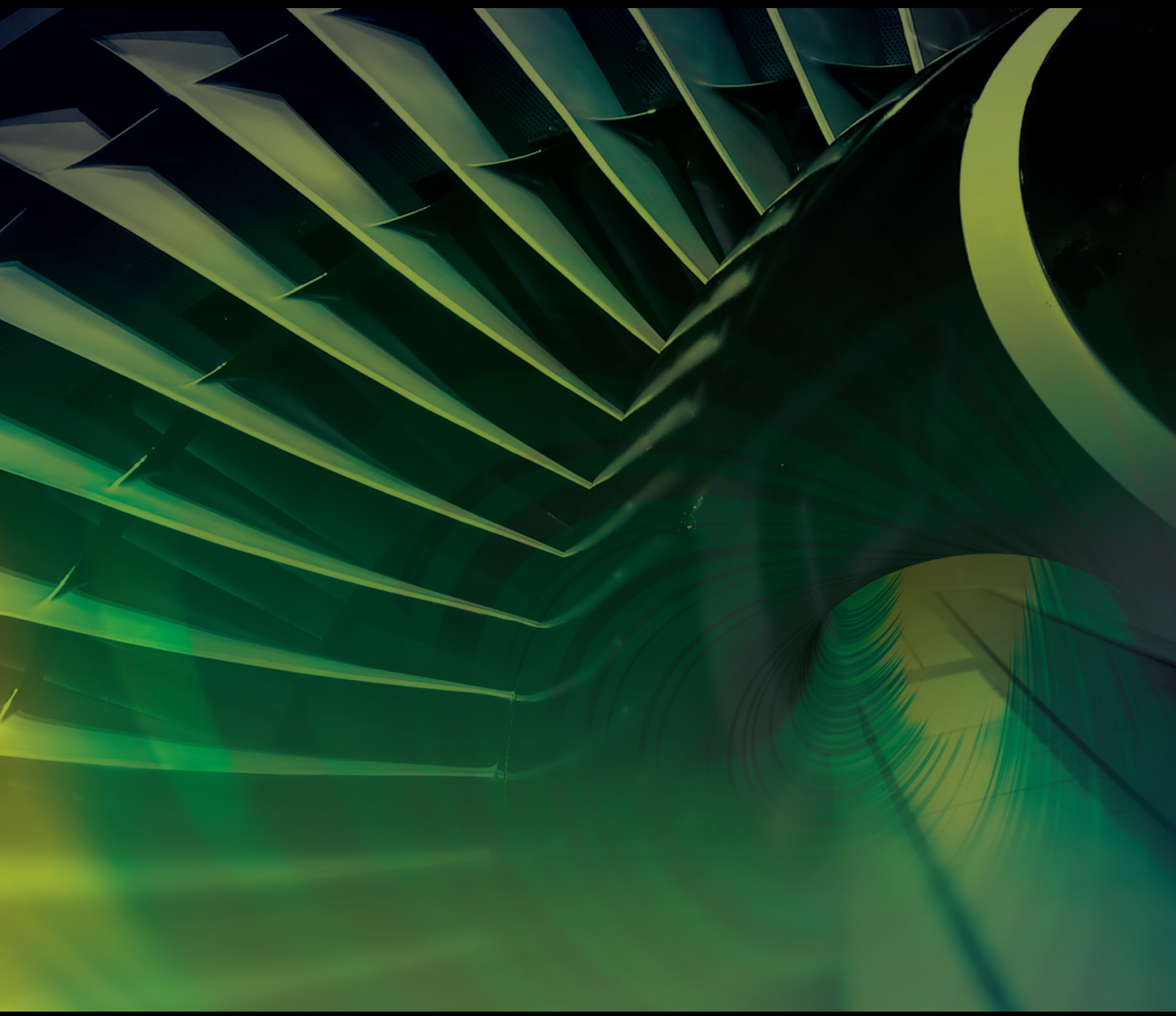

Heat Transfer and Flow Dynamics in Advanced Propulsion Systems

International Journal of Aerospace Engineering

Heat Transfer and Flow Dynamics in Advanced Propulsion Systems

Lead Guest Editor: Jian Liu
Guest Editors: Bengt Sunden, Yiheng Tong, and Qingfei Fu

Contents

Hindawi
International Journal of Aerospace Engineering
Volume 2023, Article ID 9088200, 22 pages
https://doi.org/10.1155/2023/9088200

Research Article

Characteristics of Flow Development and Boiling Transitions in the Liquid Oxygen Chill-Down Process in a Straight Horizontal Exit-Contracted Pipe

Lanwei Chen and Jiaqi Zhang

Science and Technology on Scramjet Laboratory, College of Aerospace Science and Engineering, National University of Defense Technology, Changsha 410073, China

Correspondence should be addressed to Jiaqi Zhang; amatyer_a@hotmail.com

Received 21 September 2022; Revised 12 October 2022; Accepted 24 November 2022; Published 7 February 2023

Academic Editor: Yiheng Tong

Liquid oxygen chill-down in a straight horizontal pipe was studied experimentally. The effect of the entrance corner was excluded, and much denser wall temperature sensors along the pipe have been set compared to the present studies. In this way, the chill-down process, as well as the development of the flow pattern, has been drawn for every test. As a result, the mechanism of LO_2 chill-down would be obtained for various pressure sections. For cases with stable pressure below 1.25 MPa, liquid rewetting in the pipe is controlled by the propagation of quenching fronts. For cases with a higher pressure, liquid rewetting in the second half of the pipe is controlled by the sudden liquid fill-in. Based on the transition points obtained, heat transfer coefficients on the Leidenfrost point and critical heat flux have been correlated for various pressure sections using new approaches. Conclusions show that the correlation equations are dependent on the chill-down mechanisms.

1. Introduction

Cryogenic nontoxic liquid rocket engine is a hot spot in aerospace power development, such as liquid oxygen/kerosene and liquid oxygen/methane engine [1, 2]. A cryogenic propellant has the characteristics of a low boiling point and low latent heat of evaporation, so it is easy to boil into a two-phase flow, resulting in an uncontrollable flow process. The chill-down process reduces the temperature of the pipeline system below the saturation temperature of the cryogenic propellant. For example, when the rocket engine is fired, it can ensure that the propellant flow in the pipeline rapidly changes from the gas phase to the liquid phase [3]. The chilling determines the spray characteristics of the engine injector and directly affects the engine starting process [4]. During the chill-down process, the temperature of the pipeline system drops sharply to obtain the chilling, and the cryogenic propellant completes the filling of the pipeline and establishes steady flow. In this process, the cryogenic propellant usually crosses several boiling transition points and finally turns into the liquid phase, experiencing film boiling, transition boiling, and nuclear boiling [5–7].

According to the different structure of the pipe exit, the filling process can be divided into the pipeline filling with the exit-closed, the exit-open, and the exit-contracted. The last type of pipeline filling has less related research but more research value. Normal temperature propellant does not involve strong heat exchange and phase change for pipeline filling. Zhou et al. [8, 9] studied the contracted standpipe and horizontal pipe at the end of water filling which show that the rapid filling process is dominated by gas-liquid two-phase interaction, resulting in strong water shock pressure oscillation, and high heat can be generated by instantaneous air compression in some conditions. The chill-down process of the cryogenic pipeline system with exit-contracted involves the intense heat transfer between the cryogenic propellant and the thermal pipeline, which leads

to phase transition. It involves the coupling of filling and chilling processes, and the physical process is more complex.

At present, a series of studies have been carried out on the chilling of cryogenic pipelines. Jin et al. [10–13] carried out a series of liquid nitrogen tests and simulation studies on long pipelines and proposed some heat transfer correlations. Hu et al. [14] carried out the observation of liquid oxygen chilling flow patterns in 8 mm vertical pipelines and captured several flow patterns and developments of the quenching front. Darr et al. [15–17] conducted a series of liquid nitrogen cooling pipeline tests, gave the influence law of pressure and flow parameter changes on heat flow and heat transfer coefficient at the boiling transition point, and proposed a series of correlation equations to predict T_{LFP} and q_{CHF}. Wang et al. [18, 19] carried out one-dimensional pipeline simulation research based on the existing heat transfer correlation and also studied the two-phase flow instability phenomenon in the liquid oxygen chilling process of long-distance pipeline transportation. Wang et al. [20] studied the influence of an inner microribbed pipeline, which showed that the structure enhanced the heat transfer at the film boiling stage and reduced the chilling time by half compared with the ordinary pipeline. Xu et al. [21, 22] studied the influence of coating materials on the chilling process. Chung et al. [6] studied the effect of pulse flow on the chilling process. Hartwig et al. [23] carried out tests with large pipe diameters for liquid oxygen and liquid methane. Darr et al. [24] presented one-dimensional simulation results of liquid nitrogen chilling in vertical pipelines, and the deviation between simulation and test results was within 25%. Chen et al. [25] conducted a CFD simulation study on the film boiling process in the chilling process of cryogenic pipeline and showed the distribution of cross-sectional flow patterns. Related chilling studies further revealed the heat transfer mechanism of the pipeline chilling process, but these studies usually have no contracted element on the pipeline exit, and low-pressure-drop elements are connected downstream of the pipeline. Because the overall pressure in the pipe is low (the pressure in the pipe is usually less than 1 MPa), the cryogenic propellant will be a two-phase flow state near the pipe outlet under some low-pressure conditions.

There are few studies on the chill-down process of pipeline exit-contracted. Corresponding actual scenarios include the following: During the engine hot-fire test, the propellant enters the rear pipeline from the main valve and reaches the combustor, and there is an injector at the end of the pipeline to throttle it. Accordingly, the throttling pressure drop may be as high as 3 MPa or more. A good chill-down process of the pipeline system after the valve determines the stability of the engine hot-fire starting [26, 27]. In the previous study, a horizontal liquid oxygen pipeline contracted at the outlet of $D_i = 15$ mm was tested, the test pressure was varied in the range of 0.5~0.9 MPa, and the suggested correlations of T_{LFP} and q_{LFP}, T_{CHF}, and q_{CHF} were given [28]. The influence of two contracted forms, the orifice and injector, was further studied, and the phenomenon of cooling first in the middle of the horizontal pipeline was found, and the propagation law of the cooling head and the influence of the instable wave were analyzed [29]. The horizontal liquid oxygen pipeline ($D_i = 20$ mm) with the exit contracted was studied, and the pressure range was extended to 0.6-3.5 MPa, indicating that pressure has an important influence on LFP and CHF [30]. Further analysis of the horizontal pipeline δ_{LFP} and q_{CHF} was carried out to obtain the improved correlation equation [31]. In conclusion, the preliminary experiment studies the chilling process of the exit contracted liquid oxygen pipeline, including horizontal and vertical pipes, and the process indicates that the center of the pipe will be the first to form the quenching front and then spread to the sides of the pipe, and through a series of experiments, the new correlation of the boiling change point LFP and CHF is obtained.

However, there are still some problems, including the following: (1) L-shaped and Z-shaped test tubes are used, and there is a corner, which leads to the change of flow. For the QF (quenching front) at the entrance, the effect is not obvious in the horizontal L-shaped tube but has a certain effect in the vertical Z-shaped tube. It is believed that the corner has an impact on the effect of QF at the entrance. (2) The measuring points are still not dense enough, which leads to insufficient understanding of the cooling mechanism and some contradictions, mainly including the following: in the horizontal L-shaped pipe, the main QF is first formed in the middle of the pipe, while in the vertical Z-shaped pipe, the main QF is formed at the outlet and then propagated downward. Based on the previous study [28–31], further experimental research was carried out, including the inlet of this test which will be a directly used straight pipe, excluding the influence of the inlet effect. More wall temperature measuring points are arranged along the upper and lower sides of the outer wall of the test pipe section to reproduce the cooling and filling process more clearly and completely. A wide pressure range from 0.5 to 3.5 MPa was constructed in this round of the test, and the influence of throttling pressure on precooled filling will be further analyzed.

2. Experimental Methodology

2.1. Platform. Figure 1 gives the experimental platform applied in the present study, which is the LO_2 branch of a typical experiment platform for a cryogenic engine, different from that in the previous studies [28–31]. The experimental platform in the present study is with the same front-to-back relationship between the components, but the tank volume is larger to 2 m^3, which can be used for LO_2 with a larger flow rate and longer.

Upstream of the pipeline, the LO_2 in the storage tank is pressurized and transported by the nitrogen decompressed by the pressure reducer, and the pressurized nitrogen pressure is maintained at about 5 MPa after multiple experiments. The LO_2 storage tank is a cylindrical structure with vacuum jacket, and the pipeline is equipped with a pneumatic valve (main valve), cryogenic mass flow meter, Venturi tube, and necessary temperature and pressure sensors. The LO_2 flow is controlled by the venturi tube, which can keep the flow into the experiment section constant.

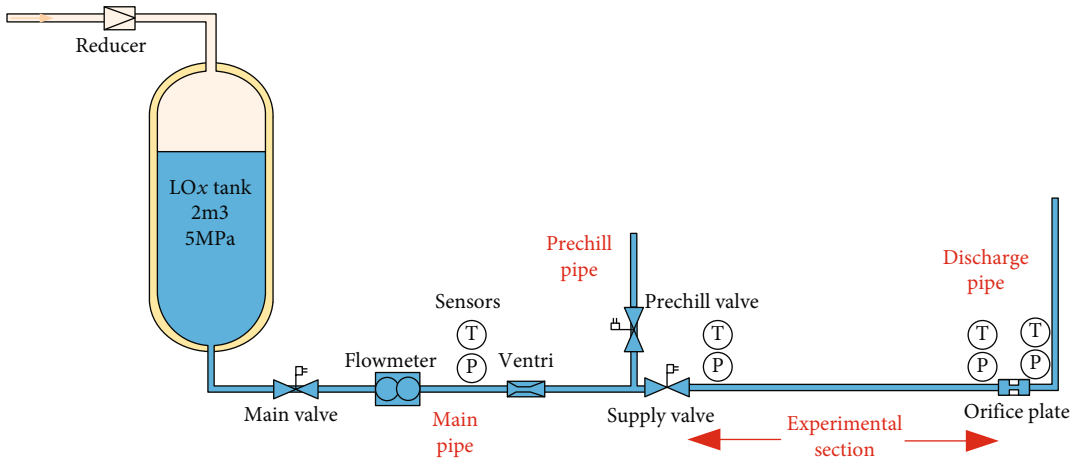

Figure 1: Experimental system of the present study.

Downstream line, including the precooling line and the experimental section could be shown in the figure. The precooling line is located in the front of the pneumatic valve (supply valve), and the experimental section is located behind the pneumatic valve (supply valve). During the experiment, the upstream line is cooled in advance by opening the precooling valve. Temperature and pressure sensors are also installed along the experimental section for the necessary data acquisition. A throttle orifice plate is installed at the outlet of the experimental section, and different experiments can provide different backpressure conditions by replacing the throttle orifice plate.

2.2. Experimental Section. Figure 2 gives the experimental section in detail. The size of the experimental section is 1200 mm in length; the inner diameter and wall thickness are 15 mm and 1.5 mm, respectively; and the material is stainless steel 316. Sensors for measuring fluid temperature and pressure are installed at the inlet and outlet of the experimental section. The temperature sensor is an insertion type, and the insertion depth of the measuring point is 5 mm. The experimental section is treated with polyurethane foam for thermal insulation, with a thickness of 20 mm, and the outer layer is also covered with aluminum foil tape to reduce the heat radiated from the outside.

14 T_o sensors (T-type thermocouples) were welded on the outer surface of the experimental section, and they were distributed over 7 sections as Figure 2(b) shows. Figure 2(b) gives the cross-section (vertical), where the 2 sensors were welded on the top and bottom of the pipe, respectively, which shows that for every section, 3 sensors were set up on the west, south, and east of the pipe in turn. All of the sensors are with the scan rate of 1000 Hz.

2.3. Experimental Measurement Method. Pressure, flow, and temperature are the main measurement parameters of the experiment. The pressure parameters are measured by piezoresistive sensors with a range of 0~10 MPa and a second-line output (4~20 mA) current signal. Fluid temperature measurement adopts thermal resistance temperature sensor (STT-100), the range is -200~50°C, and the temperature transmitter (STWB-TH-X100T) is a three-wire input and two-wire output (4~20 mA) current signal. The data scan rate used for these sensors is 1000 Hz.

The wall temperature was measured using a T-type thermocouple with a range of -200~50°C. LO_2 flow measurement adopts mass flowmeter, and the measurement range is 0~1 kg/s. The data scan rate used for these sensors is 100 Hz.

2.4. Experimental Procedure. Usually, a test is carried out according to the following process:

(1) *Filling of the LO_2 storage tank*. The maximum filling volume of the LO_2 storage tank is reserved for 20% of the gas space. When filling, the vent valve is fully opened and the filling flow is controlled so that the pressure in the storage tank is less than 0.5 MPa

(2) *Low-pressure precooling of the main pipeline*. Open the main valve and precooling valve, and use the pressure of the storage tank after filling to pressurize LO_2 to perform low-pressure precooling on the main pipeline. The precooling mass flow is 5-15 g/s, and the duration is usually more than 30 minutes. When there is continuous LO_2 flowing out of the outlet, and the mass flow and temperature are stable, it is considered that the low-pressure precooling meets the requirements

(3) *Pressurization of the LO_2 storage tank*. Before pressurizing the storage tank, the pressure in the storage tank should be less than 0.3 MPa. The storage tank is then pressurized by outputting nitrogen at a specific pressure by adjusting the pressure reducer

(4) *High-pressure chilling of the main pipeline*. The preparation process of pressurization and measurement and control sequence usually takes 3-5 min. The lack of flow of LO_2 in the pipeline will cause the temperature to rise to around -100°C. Therefore, in the test, the main pipeline was precooled at a high pressure

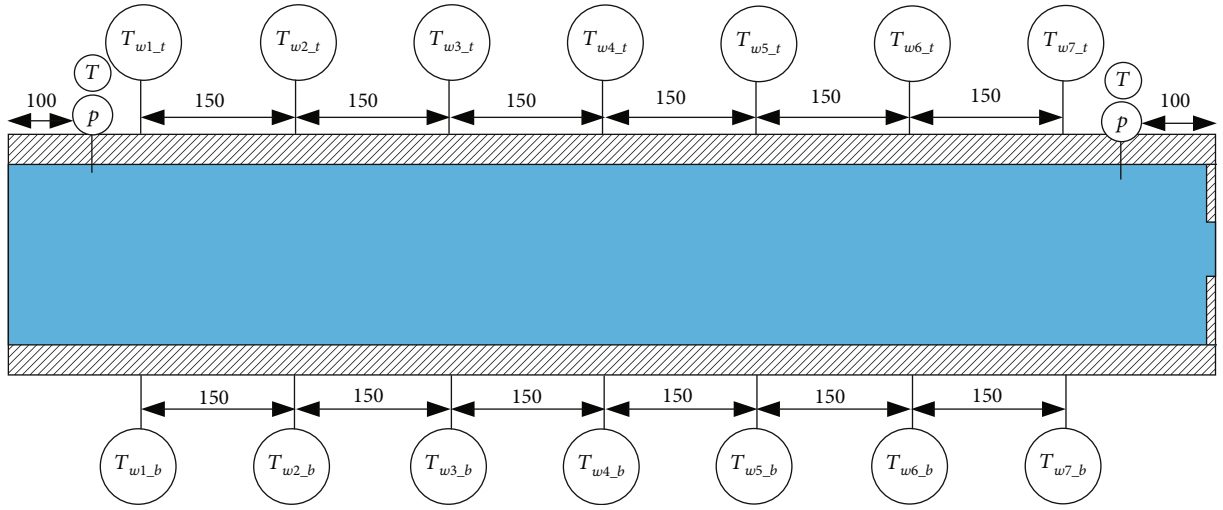

(a) Experimental section

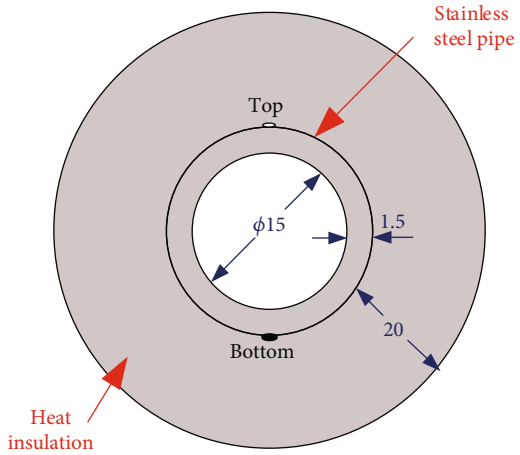

(b) Cross-section

Figure 2: Details on the experimental section, unit: mm.

for 40 s, and then, the LO_2 was switched from the precooling pipe to the experimental section

(5) *Chill-down test*. When the test section is precooled, a sufficient precooling test time should be ensured, and the LO_2 will be discharged into the atmosphere after passing through the experimental section

(6) *Rewarming of the experimental section*. The experimental section is blown out by an external nitrogen gas, and the pipe temperature is returned to normal temperature to wait for the next test

3. Experimental Results

3.1. Basic Results. Eight tests were carried out, and the test conditions and results are shown in Table 1. The tests were numbered according to the contracted orifice area A_{inj} from small to large, the corresponding contracted back pressure gradually increased from small to large, and the pressure in the pipe ranged from 0.57 to 3.49 MPa after stabilization.

These tests ranged from 0.549 to 0.564 kg/s after the liquid oxygen flow rate was stabilized, 332,150-364,457 after Re was stabilized, 107.5-108.9 K after the liquid oxygen outlet temperature (T_o) stabilized, and 7.1-108.9 K after the liquid oxygen outlet subcooling was stabilized. 36.9 K. During the test, when the supply valve is opened, when the liquid oxygen initially fills the pipeline, the pressure in the pipeline will appear as a pressure peak phenomenon, which will gradually increase with the reduction of the contracted area, and the range is 1.16-3.78 MPa.

3.2. Data Processing and Boiling Transition Points. Parameters in the pipe as well as T_o data were measured for all of the 8 tests. By processing the T_o data, T_i and q_i were obtained because most of the following discussions would be based on these 2 parameters. Here, T_i would be determined according to ref. [14], and q_i would be obtained by numerical methods introduced in the previous studies [28].

Based on T_i and q_i data, boiling curves could be drawn. In this way, the minimum q_i point and maximum q_i point would be determined. These two points are exactly the

Table 1: Experimental conditions and results.

Parameters	Exp. 1	Exp.2	Exp. 3	Exp. 4	Exp. 5	Exp. 6	Exp. 7	Exp. 8
A_{inj} (mm)	38.5	28.3	23.8	19.6	15.9	13.9	11.3	10.2
p_{ss} (MPa, end)	0.57	0.81	0.98	1.25	1.73	2.13	2.92	3.49
$\dot{m}$ (kg/s, start)	0.562	0.557	0.558	0.558	0.560	0.564	0.545	0.529
$\dot{m}$ (kg/s, end)	0.568	0.559	0.561	0.562	0.564	0.567	0.549	0.558
G (kg/(m^2•s), end)	3216	3166	3174	3180	3191	3206	3109	3159
Re (end)	336,904	364,457	358,647	356,428	352,989	346,567	332,150	342,916
T_p (K, end)	105.4	108.9	108.4	108.3	108.1	107.5	107.5	108.4
$T_{sat} - T_p$ (K, subcooling, end)	5.2	7.1	10.8	15.3	21.7	26.6	33.5	36.9
p_{peak} (MPa, start)	1.086	1.16	1.41	1.75	2.33	3.05	3.55	3.78

Table 2: Statistical t_{LFP}/t_{CHF} data (unit: s).

Position	Exp. 1	Exp. 2	Exp. 3	Exp. 4	Exp. 5	Exp. 6	Exp. 7	Exp. 8
0.15-T	4.4/6.7	3/4.8	2.8/4.2	2.2/3.6	1.6/2.8	1.4/2.3	1.3/2.1	1.8/2
0.15-B	4.9/6.1	4/5	3.5/4.2	2.2/3.7	1.9/2.9	1.4/2.3	2/2.1	1.7/2
0.30-T	16/18.9	11.6/13.6	7.1/9	4.7/7.5	3.1/5.4	2.5/4.1	3/3.3	3/3.3
0.30-B	15/17.6	12.6/13	7.1/8.9	6.6/7.3	4.2/5.4	2.6/4.1	3/3.5	1.8/3.3
0.45-T	23/26.1	13/16.9	8/10.7	8.2/9	6/6.6	1.5/5.2	2.5/4.2	1.9/4
0.45-B	23/28.6	9/16.4	9/11.2	8.2/9.8	0/6.8	0/5.2	0/3.4	0/3.1
0.60-T	17/23.1	15/19.4	8/12.8	5/10.4	1.9/7.4	1.3/5.7	1.1/4.7	1.2/4.4
0.60-B	23/24.6	15/16.7	10/11.1	8.8/9.3	1.9/7.1	1.3/5.5	1.1/4.6	1.2/4.3
0.75-T	23/28.7	16/20.9	12/14	6/11.2	1.7/8.2	1.6/6.2	1.4/5.1	1.3/4.7
0.75-B	20/23.4	15/16.3	10/10.9	9/9.4	2/7.4	1.4/5.9	1.2/5	1.3/4.5
0.90-T	24/31.1	15/22.4	12/15.1	6/12	2.2/9	1.4/7.2	1.3/5.7	1.3/5.3
0.90-B	24/27.8	17/19	11/12.7	6/10.5	1.4/8.4	1.4/6.6	1.2/5.4	1.6/5
1.05-T	2.9/5.3	4/5.8	2.3/4.5	2.1/3.6	2.1/4.1	1.4/3.8	1.3/3.6	1.4/3.4
1.05-B	3.1/9.5	4/9.7	2.3/6	2.2/5.2	2/5.7	1.6/5.1	1.4/4.9	1.5/4.3

so-called boiling transition points, which are denoted as LFP and CHF, respectively. As a result, basic data including p, T_i, q_i, and t on these boiling transition points could be obtained, which could be denoted as T_{LFP}, q_{LFP}, t_{LFP}, T_{CHF}, q_{CHF}, and t_{CHF}, etc.

Here, all of the t_{LFP} and t_{CHF} data could be collected and listed in Table 2, where t_{LFP} indicates the liquid rewetting (LFP) time from the chill-down start and t_{CHF} indicates the bubble separation time (CHF) from the chill-down start.

3.3. Uncertainty. The present study focuses on the comparison between experimental values and predicted values for T_{LFP}, q_{LFP}, T_{CHF}, and q_{CHF}. The experimental values depend mainly on the T_o measurement and physical properties as well as the geometric parameter of the pipe. On the other hand, as shown in the correlations, the predicted values depend mainly on the measured pressure and geometric parameter of the pipe. These factors are shown in Table 3.

Table 3: Summary of the uncertainties.

Parameters	Uncertainty
Fluid pressure (%)	0.5
Fluid temperature (K)	1
Outer wall temperature (K)	1
Pipe D_i and D_o (mm)	0.01
Mass flow rate (%)	1
T_o (K)	1
T_i (K)	2
q_i (%)	5

4. Chill-Down Process

In the previous study, the chill-down process has not been well defined. In the present study, it is necessary to denote that the chill-down process should be well described here. It is well known that the chill-down process starts from the time when the LO_2 first flows into the experimental section, and it finishes when the whole pipe (inner wall) gets to T_{sat}. However, in the present study, the nucleate boiling section will not be discussed. As a result, CHF is usually treated as the end of the chill-down process in the present study.

For a certain point with the T-type thermocouple on the outer surface of the wall, T_o could be measured and T_i could

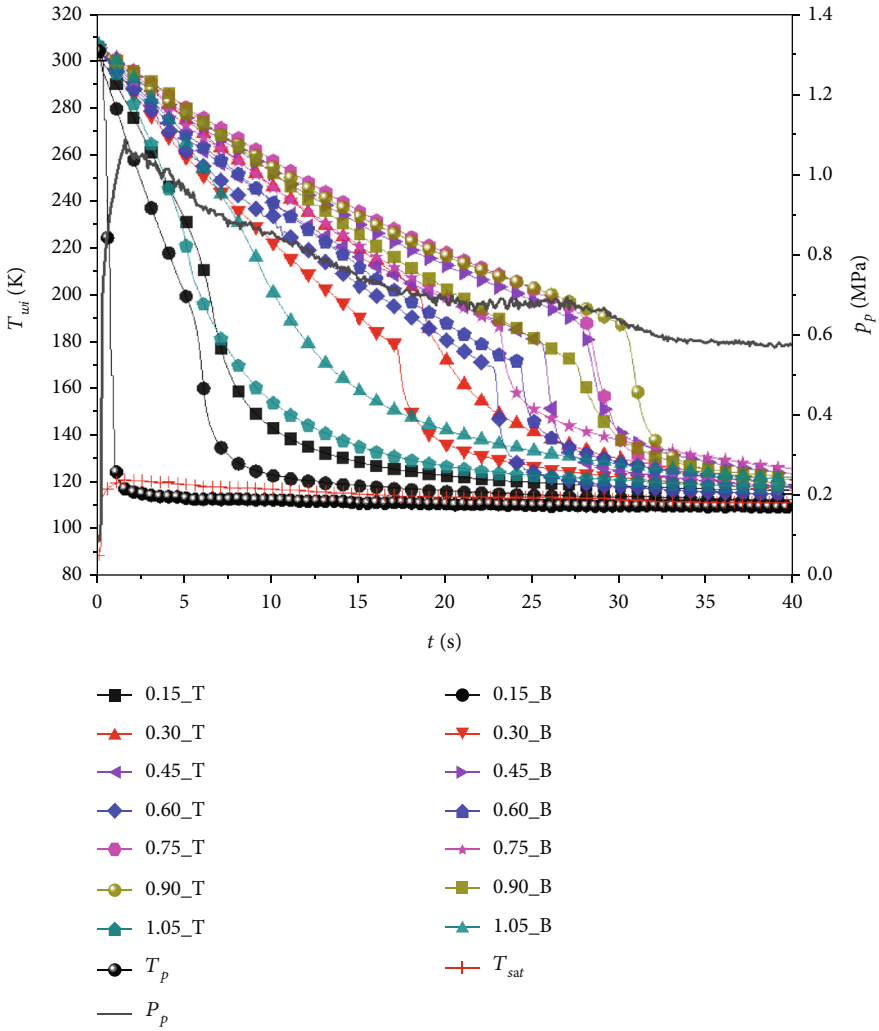

Figure 3: Data curves for Exp. 1 ($\dot{m} = 0.568$ kg/s, $p_{ss} = 0.57$ MPa).

be obtained. In this way, the basic history of the decreasing T_i as well as the q_i curve could be drawn, and the boiling transition points on this point could be obtained. For the whole pipe, based on the T_i data at various points, the historical T_i distribution could be drawn. However, this distribution is difficult to be drawn, and it could not play a significant role on analysis. In this way, for analysis, boiling transition points are extremely significant, by which the development of the flow pattern in the experimental pipe could be drawn.

As a result, in the present study, the chill-down process would be described by two items, the development of basic curves (all measured T_i and other parameters) and, more importantly, the development of the flow pattern in the experimental section. In most cases, the latter item is equal to the chill-down process.

As shown in Table 2, all of the eight tests could be classified into two groups roughly, the low-pressure condition, for Exp. 1~4, and the high-pressure condition, for Exp. 5~8. Apparently, the chill-down processes for these two groups are different from each other, according to the t_{LFP} and t_{CHF} data listed in Table 2. In the present section, the chill-down process for these two groups will be given in detail.

4.1. Chill-Down Process of Exp. 1. As the basic case, the chill-down process for Exp. 1 will be given in detail to show its basic manner.

4.1.1. Basic Curves Recorded. Figure 3 gives the data curves for Exp. 1. It shows that, as the LO_2 flows into the experimental section, because of the flash vaporization, pressure in the experimental section pipe increases sharply. On the other hand, temperature in the experimental section undergoes a sharp decrease. This is one of the primary characteristics of the cryogenic chill-down in the exit-contraction pipe for both the horizontal direction [30] and the vertical direction [31].

As shown in Figure 3, during the chill-down process, all of the wall temperature values show the typical manner of low-pressure chill-down. The T_i data curves show the obvious linear manner on the film boiling section, and a typical sharp decrease on the transition boiling and nucleate boiling section. As shown in the figure, T_i values on the $L_{se} = 0.15$ m

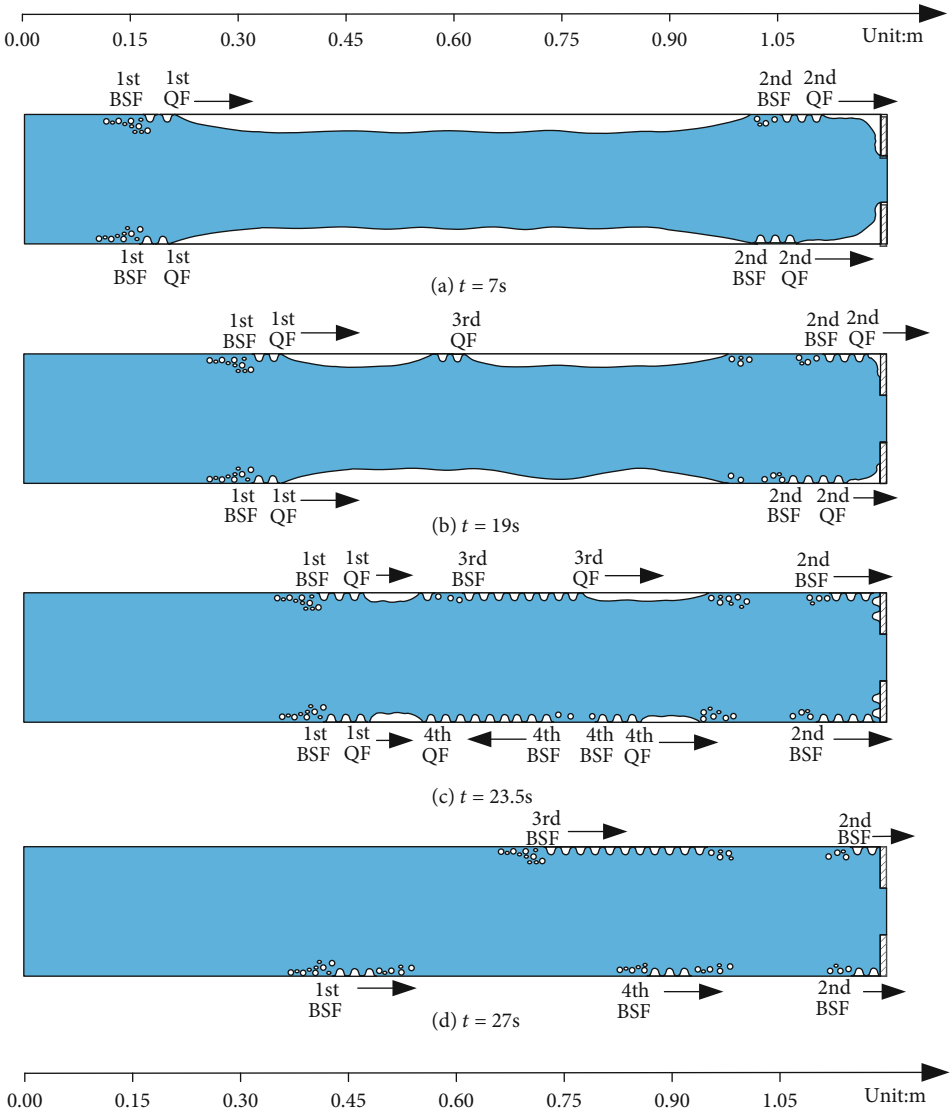

Figure 4: Flow patterns in the experimental section during the chill-down process for Exp. 1.

cross-section (0.15 m cross-section next for simplification) decrease at first with the lowest slope on the film boiling section, followed by 1.05 m, 0.3 m, and 0.6 in turn, and followed by the other sections including 0.45 m, 0.75 m, and 0.9 m, on which T_i values decrease by the similar slopes.

4.1.2. Development of Flow Pattern in the Experimental Section. As shown in Table 2, for Exp. 1, by considering the average values, LFP happens on the 1.05 m cross-section at first, followed by 0.15 m, 0.3 m, 0.6 m, 0.75 m, 0.45 m, and 0.9 m in turn. This sequence is very similar with the sequence of CHF happening, and the sequence of T_i slope discussed in Section 4.1.1.

Based on Table 2, the development of the flow pattern in the experimental section could be drawn as shown in Figure 4. For drawing these figures, the thickness of the vapor film for every sensor point instantaneously has been checked. This is the basic foundation to describe the chill-down process. As shown in the figures and table, for Exp. 1, as the LO_2 flows into the experimental section, which is the horizontal straight pipe, flash vaporization happens. The flow pattern in the whole pipe is immediately changed to a boiling film, by which the liquid core is surrounded by the vapor layer, which is in contact with the pipe wall.

Before 5.3 s, the inlet quenching front (QF), denoted as the 1st QF, has been formed and gets to the 0.15 m cross-section. Simultaneously, the exit QF (2nd QF) has been formed on the 1.05 m cross-section. A few seconds later, the inlet bubble separation front (the 1st BSF) is formed following the 1st QF and the 2nd BSF following the 2nd QF. All of these fronts propagate forward. As shown in Figure 4 and Table 2, it is evident that the 1st QF and the 1st BSF dominate the chill-down of the upper section of the experimental pipe, from the inlet to around 0.45 m cross-section. Similarly, the 2nd QF and the 2nd BSF dominate the chill-down of the end section of the experimental pipe, from around 1.05 m cross-section to the exit. After that, as shown in the figures and Table 2, the 3rd QF and the 4th QF have

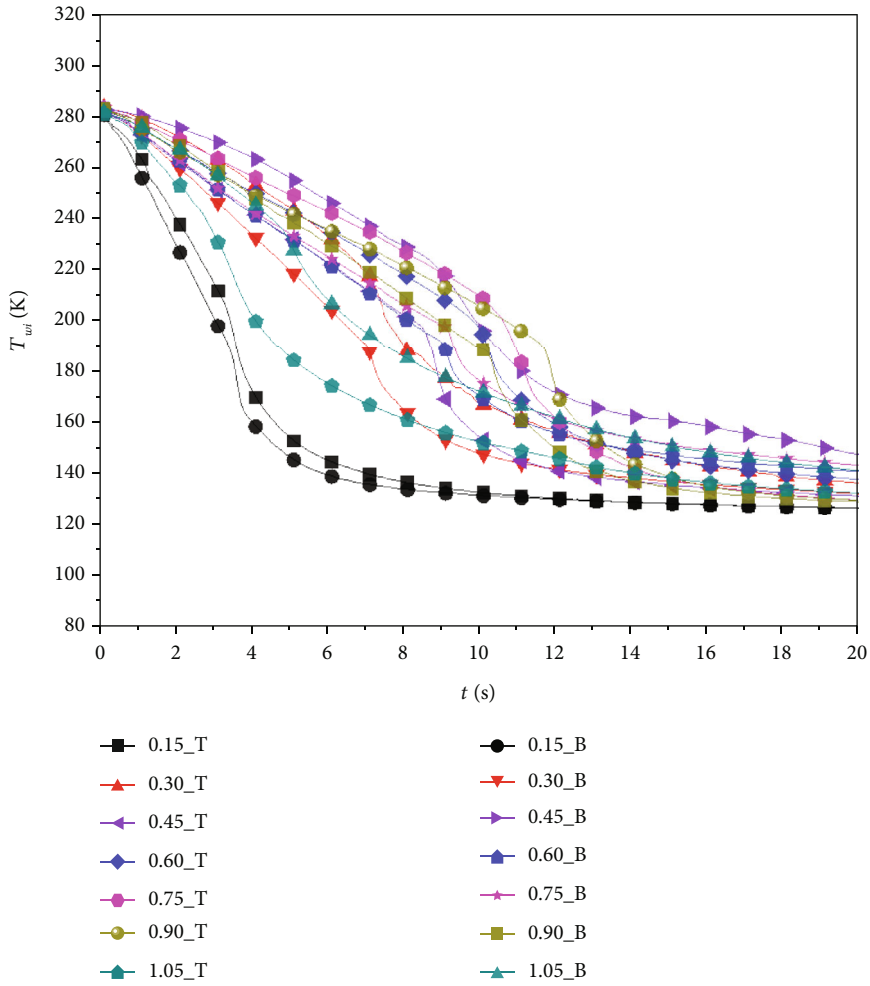

FIGURE 5: Data curves for Exp. 4 ($\dot{m} = 0.562$ kg/s, $p_{ss} = 1.25$ MPa).

been formed on 0.6-T and 0.75-B at 17 s and 20 s, respectively. After that, the 3rd BSF and the 4th BSF are formed on 0.6-T and 0.75-B at around 23.1 s and 23.4 s, respectively. The 3rd QF and BSF propagate forward, and the 4th QF and BSF propagate both forward and backward. As a result, it is evident that the chill-down of the section, from $L_{se} = 0.6$ m to $L_{se} = 0.9$ m is controlled by the 3rd and 4th fronts (QF and BSF).

4.2. Chill-Down Process for Low-Pressure Condition. Similarly, Figure 5 gives the basic T_i curves for Exp. 4, the $p_{ss} = 1.25$ MPa case. Comparison between Figures 3 and 5 shows that, for Exp. 4, during the chill-down process, most T_i curves show similar traits with those for Exp. 1. The primary difference is that the slopes of the linear section on the T_i curves in Figure 5 are much sharper than those in Figure 3. As a result, as shown in Table 2, t_{LFP} and t_{CHF} values for Exp. 4 are much lower than those for Exp. 1.

The flow patterns in the experimental pipe during the chill-down process for Exp. 4 can be shown in Figure 6. As shown in the figure, at 5 s, the 1st BSF gets to the 0.15 m cross-section, following the 1st QF at 0.3-T. Simultaneously, the 2nd BSF gets to the $L_{se} = 1.05$ m section (almost for 1.05-T), and the 3rd QF has been formed on 0.6-T. At 6 s, the section from 0.6-T to 0.9-T is rewetted because of the propagation of the 3rd QF, and the 4th QF has been formed on 0.9-B. At 8.2 s, the top surface of the experimental section has been rewetted completely because of the propagation of both the 1st QF and the 3rd QF. Furthermore, at 9 s, the bottom surface of the experimental section has been rewetted completely because of the propagation of both the 1st QF and the 4th QF. After that, it could be found that the CHF of the top surface of the experimental pipe is the propagation of the 1st BSF control, where the 3rd BSF has disappeared on the transitioned boiling section. On the other hand, similar to Exp. 1, the bubble separations of the bottom surface on the upper section (inlet to 0.45-T) and the section from 0.6-T to 0.9-T are controlled by the 1st BSF to the 4rd BSF, respectively.

Comparison shows that the so-called low-pressure condition includes Exp. 1~4, which is with both the similar manner of T_i curves and the development of the flow pattern in the experimental pipe.

4.3. Chill-Down Process for High-Pressure Condition. The T_i curves for Exp. 5 and Exp. 7 can be shown in Figures 7 and 8, respectively. As shown in the figures, the decrease of T_i curves is in the same manner, which is much different

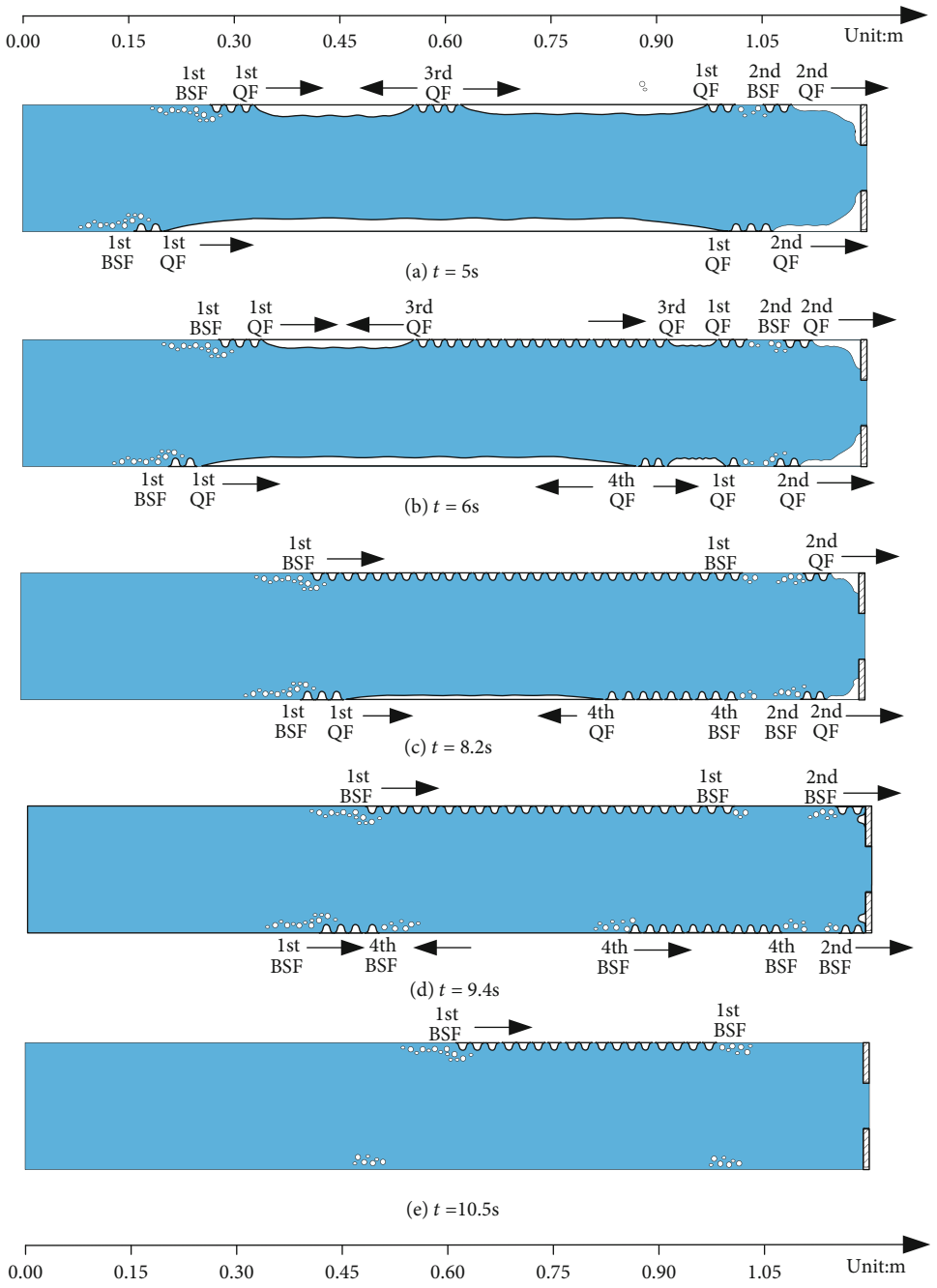

Figure 6: Flow patterns in the experimental section during the chill-down process for Exp. 4.

from that for the low-pressure condition. The T_i curves here are with the basic decreasing manner of linear-accelerated, followed by the gradual. As a result, the basic characteristics include that, at first, the linear section is extremely short, which indicates the shortened film boiling. On the other hand, the accelerated decrease section on the curve expands the long period, which indicates the relatively longer period of transition boiling.

Based on the figures and Table 2, the development of the flow pattern in the experimental section could be drawn as shown in Figure 9. Similarly, this figure could be also drawn for Exp. 7, which is similar with Exp. 5 and could not be drawn again. As shown in Figure 9(a), at around 2.2 s, the 1st QF gets to the 0.15 m cross-section, and on the other hand, the length from 0.6 m to 1.05 m of the experimental pipe has been rewetted almost simultaneously. The latter fact is obviously caused by the liquid fill-in. It could be supposed that two QFs would be formed here, the 2nd QF around the 1.05 m cross-section and the 3rd QF between the 0.45 m and 0.6 m cross-sections. After that, liquid rewetting happens on the 0.3 m and 0.45 m cross-sections in turn at 5.4 s and 6.6 s, respectively. This indicates that the liquid rewetting on the section from the inlet to 0.45 m is controlled by the propagation of the 1st QF, and the liquid rewetting on the section

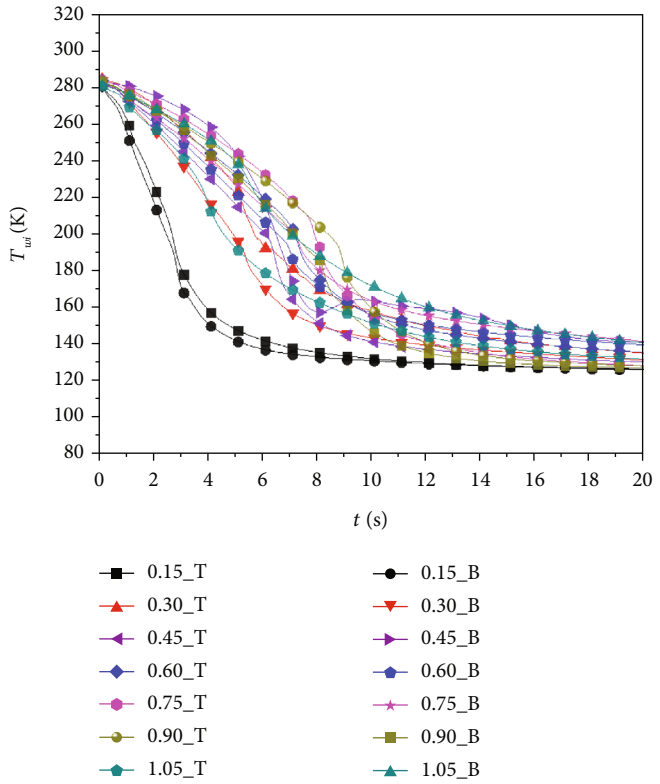

Figure 7: Data curves for Exp. 5 ($\dot{m} = 0.564$ kg/s, $p_{ss} = 1.73$ MPa).

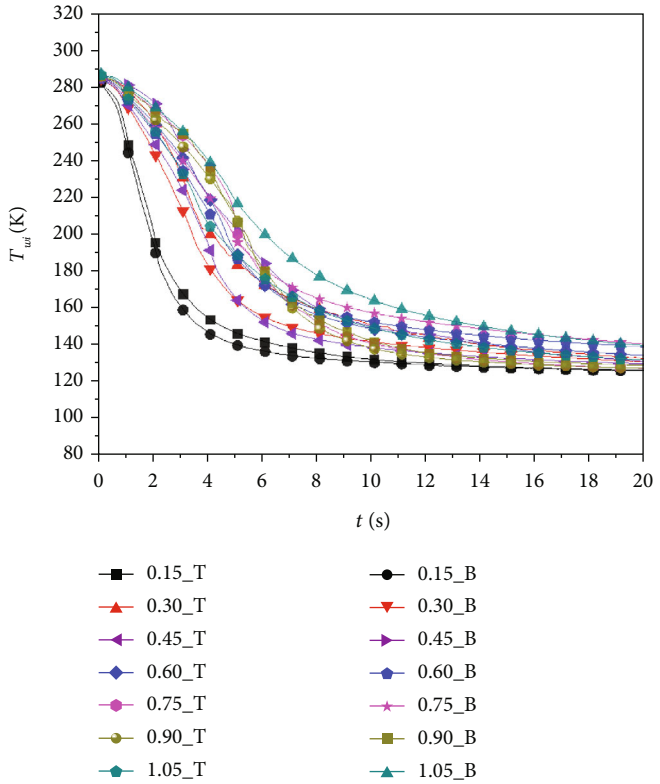

Figure 8: Data curves for Exp. 7 ($\dot{m} = 0.549$ kg/s, $p_{ss} = 2.92$ MPa).

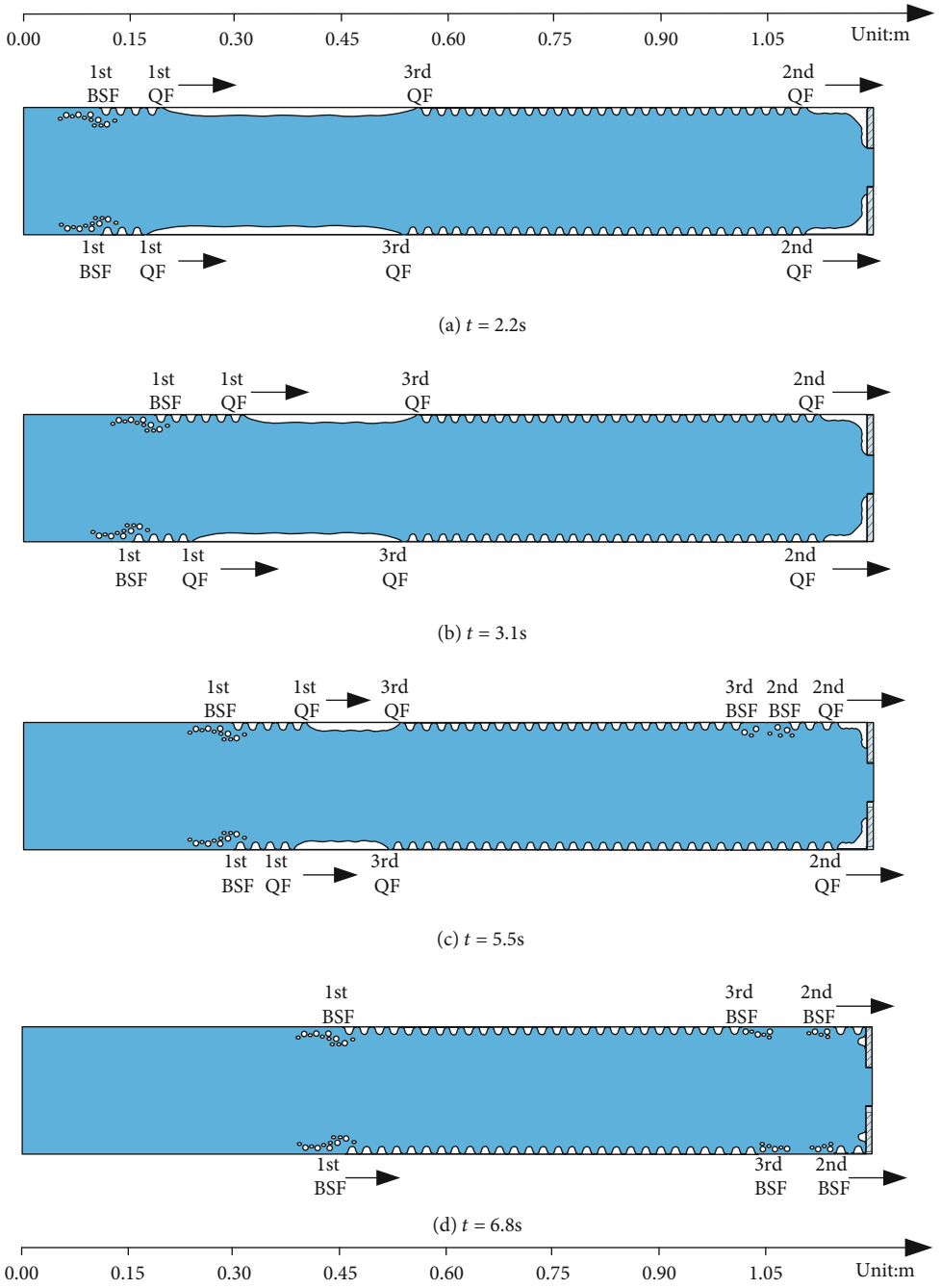

Figure 9: Flow patterns in the experimental section during the chill-down process for Exp. 5.

from 1.05 m to the exit is controlled by the propagation of the 2nd QF. However, the liquid rewetting on the section from 0.6 m to 1.05 m is controlled by the liquid fill-in, which is different from that for the low-pressure condition. With the increase of pressure, this section would be enhanced in length as shown in Table 2.

4.4. Chill-Down Process

4.4.1. Low-Pressure Condition. For the low-pressure condition (Exp. 1~4), as shown in Figures 3 and 5, the decrease of the T_i curve shows the linear-sharp-gradual manner, with the long linear section, corresponding to the relatively long period of film boiling. The increase of pressure reduces the linear section primarily, which reduces the t_{LFP} values as shown in Table 2. The experimental pipe could be divided into three sections based on the dominant factors as shown in Figure 10.

For both the pool boiling and the flow boiling, on the film boiling section, with the decrease of the wall temperature, the vapor thickness (δ) would undergo a decrease and the magnitude of the instable wave (M_w) would undergo an increase. Once these two parameters get to the same value, liquid rewetting happens here [32], which could be

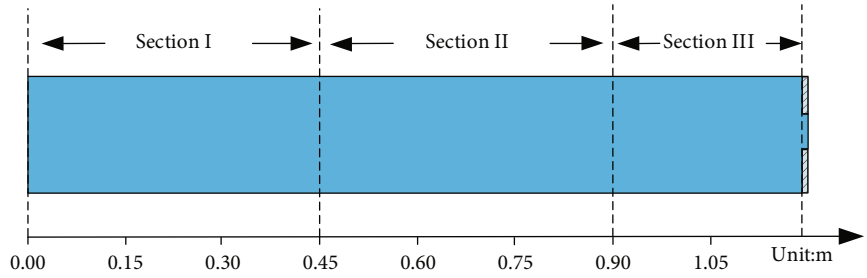

Figure 10: Sections divided in the experimental pipe.

denoted as LFP. This indicates two controlling factors of LFP, low δ or high M_w. The propagation of QF has been observed obviously in the studies on cryogenic chill-down in the transport pipe without exit-contraction [34].

Here, as shown in Figures 4 and 6, the liquid rewetting of the Section I and Section III would be always controlled by the 1st QF and the 2nd QF, respectively. On Section II, the extra QFs would be formed and propagated to control the liquid rewetting of this section during the chill-down process. For flow boiling, the area near QF has obviously the lowest δ and would get to LFP next, in which the development of flow is like the manner of "QF propagation." This could be denoted as the mechanism of QF propagation in the present study.

For the low-pressure condition (Exp. 1~4), with the development of chill-down, every QF concerned above would produce a BSF consistently, which would control the bubble separation on the corresponding section, and every BSF following QF has experienced adequately development. In this way, these BSFs would undergo the similar propagation with QF.

As shown in the ref. [14], bubble separation has been detected in cryogenic flow boiling. This point is denoted as CHF, or the bubble separation point, on which bubbles produced on the wall would flow into the main flow. This point is similar with LFP, which propagates downstream. In this way, BSF would be defined like QF. On BSF and its upstream, bubble separation would happen. Different from QF, the existence of BSF and its propagation are based on the fact that the heat flux that flows into the fluid is enough to vaporize the local liquid. This determined two characteristics of CHF or BSF. At first, it has to be following transition boiling. On the other hand, it is determined by the heat flux value (q_i), which has to be under adequately development before CHF.

4.4.2. High-Pressure Condition. For the high-pressure condition (Exp. 5~8), the decrease of the T_i curve shows the linear-accelerated-gradual manner as shown in Figures 7 and 8, with the long accelerated section, corresponding to the lengthened transition boiling section. It shows that the increase of pressure produces limited variations on both t_{LFP} and t_{CHF} as shown in Table 2. On the other hand, as shown in Figure 9, similar with the low-pressure condition, the liquid rewetting of Section I is always controlled by the 1st QF. However, the liquid rewetting of Section II and Section III is always suddenly obtained in a very short period, which indicates that it is controlled by the liquid fill-in during the chill-down process. This is controlled by another mechanism of LFP, high M_w, as mentioned above. With the increase of pressure, Section II would be prolonged.

With the LO_2 flows into the pipe, the vapor-liquid mixture could be blocked by the exit concentration. In this way, the mixture has to be accumulated on the second half of the pipe. For low pressure, this factor plays a weaker action. However, for high pressure, because of the low variations between the vapor phase and the liquid phase, the liquid is more likely to reach the inner wall here. On the other hand, h_{LFP} here is lower compared to the first half of the pipe, which indicates high δ_{LFP} and M_{LFP} here.

However, different from the low-pressure condition, for the high-pressure condition (Exp. 5~8), the bubble separation in Sections I and II is always controlled by the propagation of the 1st BSF, and the bubble separation in Section III is always controlled by the propagation of the 2nd BSF. CHF could not happen following the QFs on the second half of tube because both q_i (heat flux) and h_i (heat transfer coefficient) here have not experienced enough development. Or in other words, both q_i and h_i here are not high enough to get CHF. In this way, BSF propagates from the inlet to the outlet.

4.4.3. Classification. Basically, as discussed above, the decreasing manner of T_i curves and the development of the flow pattern in the experimental pipe for the low-pressure condition are much different from those for the high-pressure condition. This indicates that the process and mechanism of chill-down are different for these two groups.

As a result, based on the dominant factors of liquid rewetting, Table 4 can be listed.

5. Film Boiling Section and Leidenfrost Point

5.1. Leidenfrost Point

5.1.1. Basic Data. Figures 11 and 12 plot the data of ΔT_{LFP} and q_{LFP} versus p_{LFP}, respectively, which shows the basic effects of pressure on these parameters. As shown in the figures, all of the seven L_{se} cross-sections could be classified by a few methods based on the effects of p_{LFP} on ΔT_{LFP} or q_{LFP}. However, based on Equations (1) and (2), as well as the discussions in the previous studies [30, 31], δ_{LFP}, which indicates the thickness of the vapor film on LFP, is the primarily dominant parameter indicating the physical process. Sometimes, h_{LFP} would be discussed instead. In this way, all of the cross-sections would be classified into Class I and

Table 4: L_{se} range schematically.

Exp.	Section I	Section II	Section III
1	0~0.45 (2nd type)	0.6~0.9 (3rd type)	1.05~1.2 (2nd type)
2	0~0.45 (2nd type)	0.6~0.9 (3rd type)	1.05~1.2 (2nd type)
3	0~0.45 (2nd type)	0.6~0.9 (3rd type)	1.05~1.2 (2nd type)
4	0~0.45 (2nd type)	0.6~0.9 (3rd type)	1.05~1.2 (2nd type)
5	0~0.45 (2nd type)	0.6~0.9 (1st type)	1.05~1.2 (1st type)
6	0~0.3 (2nd type)	0.45~0.9 (1st type)	1.05~1.2 (1st type)
7	0~0.3 (2nd type)	0.45~0.9 (1st type)	1.05~1.2 (1st type)
8	0~0.3 (2nd type)	0.45~0.9 (1st type)	1.05~1.2 (1st type)

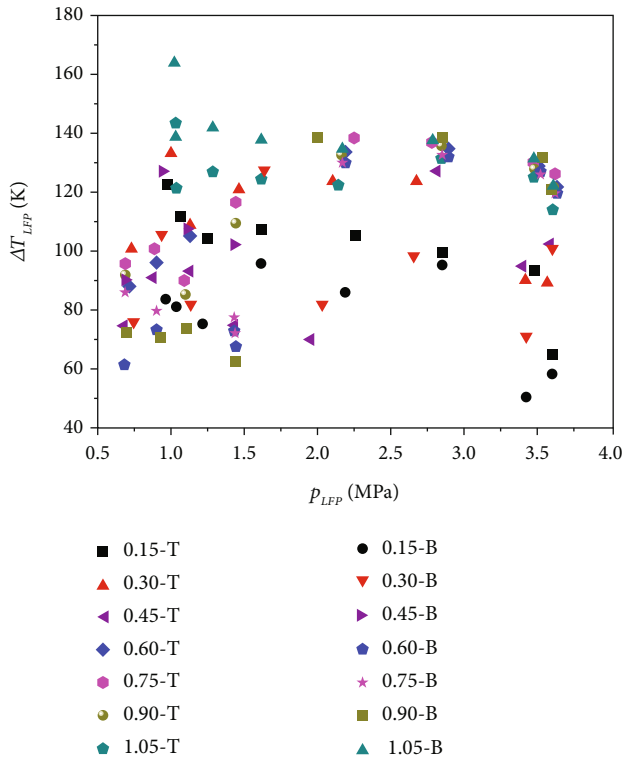

Figure 11: Experimental p_{LFP} versus ΔT_{LFP}.

Class II, according to the h_{LFP} data, which are consistent with the δ_{LFP} data.

$$h_{LFP} = \frac{q_{LFP}}{\Delta T_{LFP}}, \quad (1)$$

$$h_{LFP} = \frac{k_v}{\delta_{LFP}}. \quad (2)$$

5.1.2. Cross-Sections in Class I. Class I includes both 0.15 m and 0.3 m cross-sections. Parameters h_{LFP} and δ_{LFP} could be plotted versus p_{LFP} as shown in Figures 13 and 14, respectively. On these cross-sections, with the increase of pressure, h_{LFP} undergoes the increasing manner and δ_{LFP} undergoes the overall decreasing manner, which is the basic characteristic of this class. This basic characteristic is mainly caused by the fact that these sections are near to the inlet, the QF formation area. This is similar to the other cases in the previous studies, the so-called "heat transfer control" manner, $L_{se} = 0.75$ m for the L-shaped horizontal experimental section [30] and $L_{se} = 1$ m for the Z-shaped vertical experimental section [30]. The primary difference between the present study and the previous studies is the pressure range. In the present study, the p_{ss} tested ranges from 0.57 to 3.55 MPa. However, in the previous studies, the tested p_{ss} values were below 2 MPa [30, 31].

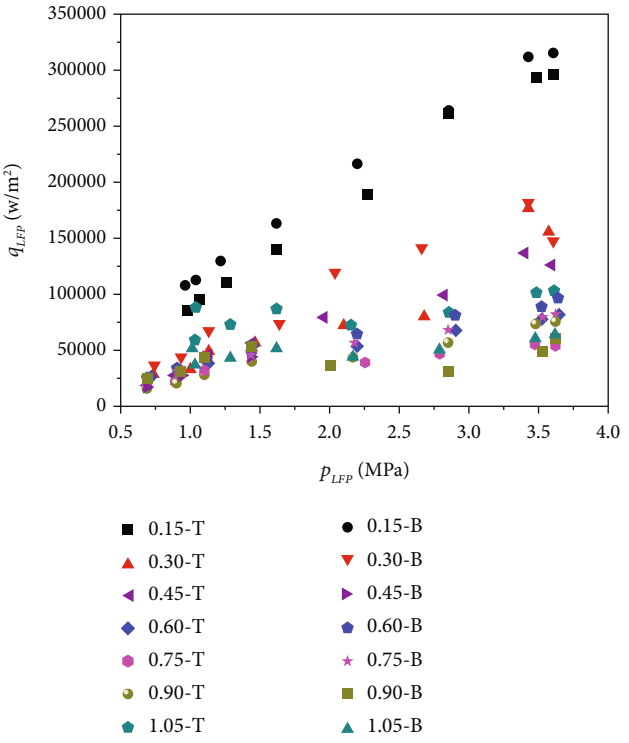

Figure 12: Experimental p_{LFP} versus q_{LFP}.

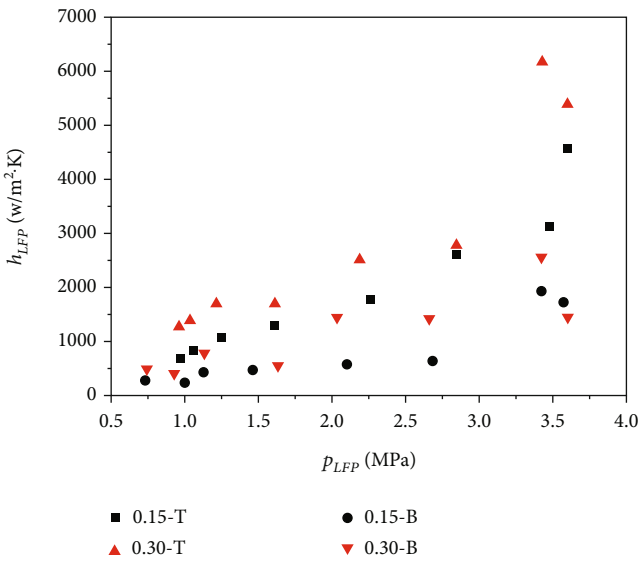

Figure 13: h_{LFP} versus p_{LFP} for class I.

As shown in Figures 13 and 14, the increase of pressure produces continuously increasing h_{LFP}, due to the decreasing

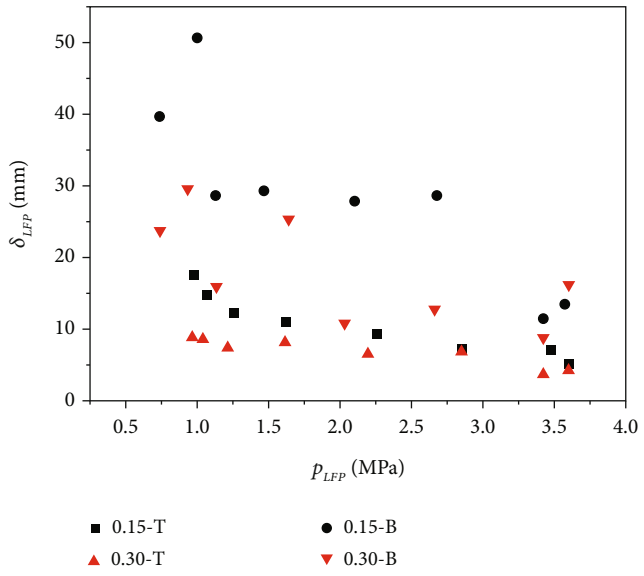

Figure 14: δ_{LFP} versus p_{LFP} for class I.

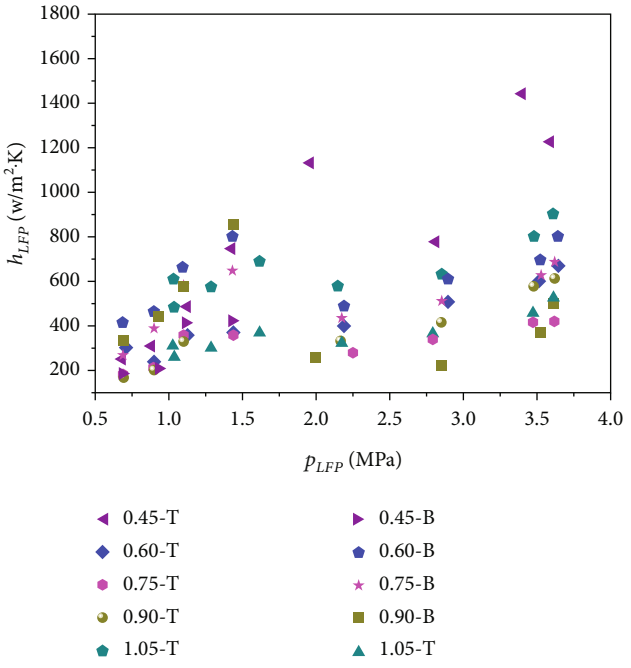

Figure 15: h_{LFP} versus p_{LFP} for class II.

δ_{LFP} and increasing k_{v} as shown in Equation (2). This is based on the fact that the increase of pressure would produce lower MLFP (magnitude of instable wave) in such a wide pressure range. Another fact is that throughout the pressure range in the present study, the basic mechanism of liquid rewetting has not been converted for Class I, which is always controlled by the propagation of the inlet QF as discussed in Section 4.4.

5.1.3. Cross-Sections in Class II. Class II includes all of the other cross-sections. Parameters h_{LFP} and δ_{LFP} could be plotted versus p_{LFP} as shown in Figures 15 and 16. With the increase of pressure, h_{LFP} shows the obvious "N" shape,

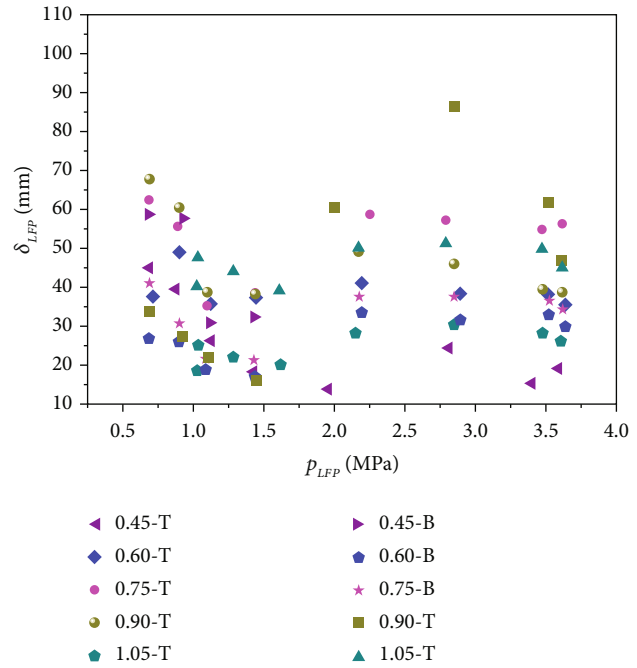

Figure 16: δ_{LFP} versus p_{LFP} for class II.

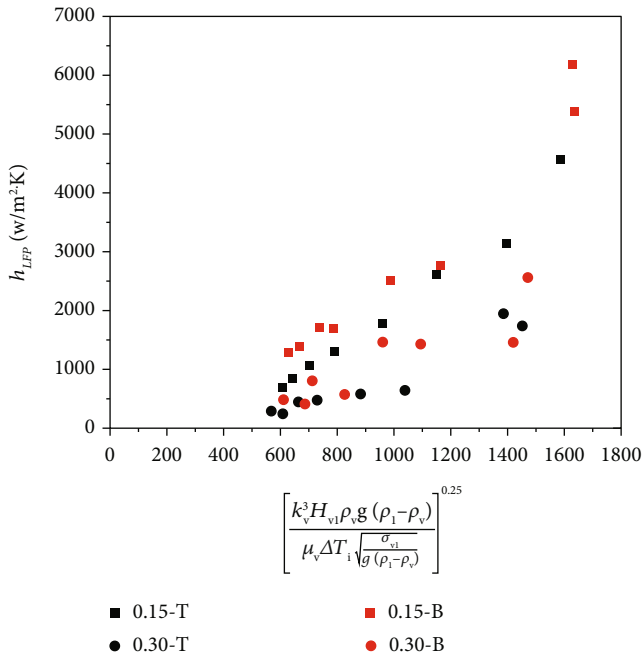

Figure 17: h_{LFP} versus $[k_{\mathrm{v}}^3 H_{\mathrm{vl}}\rho_{\mathrm{v}} g(\rho_{\mathrm{l}}-\rho_{\mathrm{v}})/\mu_{\mathrm{v}}\Delta T_{\mathrm{i}}\sqrt{\sigma_{\mathrm{vl}}/g(\rho_{\mathrm{l}}-\rho_{\mathrm{v}})}]^{0.25}$ for cross-sections in Class I.

and δ_{LFP} shows the inverted "N" shape. This is the primary characteristic here. For Class II, h_{LFP} shows the increasing manner from Exp. 1 to 4. After that, it undergoes a certain drop from Exp. 4 to 5 (from Exp. 5 to 6 for 0.45-T), followed by another section increase from Exp. 5 to Exp. 8. Likewise, the distribution of δ_{LFP} shows the consistent inverted manner, which undergoes a certain enhancement from Exp. 4 to 5 as shown in Figure 16.

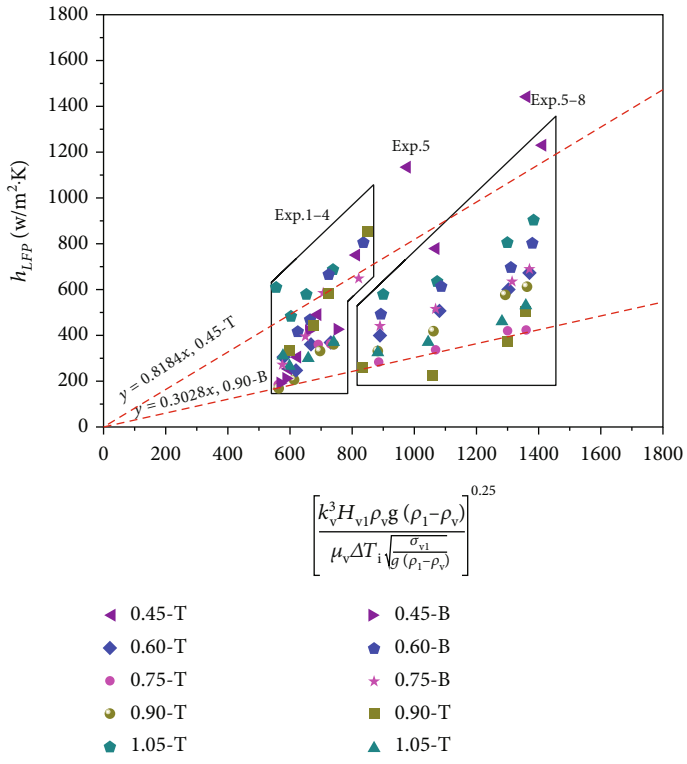

FIGURE 18: h_{LFP} versus $[k_v^3 H_{vl}\rho_v g(\rho_l-\rho_v)/\mu_v \Delta T_i \sqrt{\sigma_{vl}/g(\rho_l-\rho_v)}]^{0.25}$ for cross-sections in Class II.

This phenomenon is primarily caused by the conversion of the liquid rewetting mechanism as discussed in Section 4.4. On these cross-sections, liquid rewetting is controlled by the QF propagation for low-pressure cases (Exp. 1~4, or Type I discussed in Section 4.2). However, on the high-pressure cases (Exp. 5~8, or Type II discussed in Section 4.3), liquid rewetting is controlled by the local QF produced by liquid fill-in. This conversion on the liquid rewetting mechanism from Exp. 4 to Exp. 5 produces a certain increase of δ_{LFP}. This indicates that for these sections, M_{LFP} (magnitude of the instable wave, equal to δ_{LFP}) produced by the propagated QF is greater than that produced by the produced QF locally.

Obviously, this conversion is produced by the increase of p_{ss} from 1.25 to 1.73 MPa or the increase of p_{LFP} from 1.5 to 2.1 MPa. With the increase of pressure in this range, on the cross-sections from around 0.45 m to 1.05 m, the factor of liquid fill-in overcomes the factor of QF propagation as the dominant factor, which produces the dramatic reductions on t_{LFP} as shown in Table 2. In particular, for the L_{se} = 1.05 m section, the dominant factor of liquid rewetting converts from the propagation of the exit QF to the local QF produced by the liquid fill-in.

5.2. Correlation on Heat Transfer Coefficient. In the previous study, h_{LFP} could be well correlated by Equation (3), where C_2 could be various constants for various points [31].

$$h_{LFP} = C_2 \left[\frac{k_v^3 H_{vl}\rho_v g(\rho_l-\rho_v)}{\mu_v \Delta T_i \sqrt{\sigma_{vl}/g(\rho_l-\rho_v)}}\right]^{0.25}. \quad (3)$$

In the present study, we try to correlate h_{LFP} via Equation (3) for cross-sections of 0.15 m and 0.3 m as shown in Figure 17 and for other cross-sections as shown in Figure 18, where some exception points have been removed. As shown in the figures, for the points (Sections II and III for Exp. 5~8, as shown in Table 4) where liquid rewetting is controlled by the local QF produced by liquid fill-in, h_{LFP} could be well correlated via Equation (3), in which various C_2 can be shown in Table 5. It shows that reliable predictions could be obtained for these points.

However, for the other conditions, where liquid rewetting is controlled by the propagation of QF, the slopes of h_{LFP} increase are obviously greater than those predicted by Equation (3). In this way, for these conditions, we will try to prove a new correlation approach, and Equation (4) could be set up. By data fitting as shown in Figure 19, C_1 and C_2 could be determined for these points and listed in Table 5. As shown in the figure and table, for the points on 0.15 m, 0.3 m, and 1.05 m, C_1 has been determined to be 0.4326, and for other points, C_1 has been obtained to be 0.6926. It shows that h_{LFP} could be well predicted in this way.

$$h_{LFP} = C_2 \left[\frac{k_v^3 H_{vl}\rho_v g(\rho_l-\rho_v)}{\mu_v \Delta T_i \sqrt{\sigma_{vl}/g(\rho_l-\rho_v)}}\right]^{C_1}. \quad (4)$$

5.3. Discussions

5.3.1. Correlation Approaches. As shown in Table 4, data points could be classified into three types, which could be correlated by three equations, respectively. From the 1st type

Table 5: C_1 and C_2 values and deviations.

Position	Range	C_1 in Eq. (4)	C_2 in Eq. (4)	Error (%)	Range	C_2 in Eq. (3)	Error (%)
0.15-T	Exp. 1~8	0.4326	0.012187	-8.1~14.6			
0.3-T	Exp. 1~8	0.4326	0.005214	-26.8~34.6			
0.45-T	Exp. 1~5	0.6926	5.92×10^{-6}	-11.5~14.5	Exp. 6~8	0.8184	-5.9~12.2
0.6-T	Exp. 1~4	0.6926	4.72×10^{-6}	-11.9~8.7	Exp. 5~8	0.4712	-3.6~4
0.75-T	Exp. 1~4	0.6926	4.38×10^{-6}	-10.8~6.0	Exp. 5~8	0.3174	-1.6~1.7
0.9-T	Exp. 1~4	0.6926	4.03×10^{-6}	-7.8~6.3	Exp. 5~8	0.4269	-5.2~13.2
1.05-T	Exp. 1~4	0.4326	0.007574	-2.4~1.8	Exp. 5~8	0.6289	-3.5~6.2
0.15-B	Exp. 1~8	0.4326	0.016669	-10.9~21.1			
0.3-B	Exp. 1~8	0.4326	0.008878	-18.9~21.9			
0.45-B	Exp. 1~4	0.6926	4.94×10^{-6}	-23~9.6	—	—	—
0.6-B	Exp. 1~4	0.6926	7.23×10^{-6}	-9.4~11.9	Exp. 5~8	0.5577	-4.2~5.1
0.75-B	Exp. 1~4	0.6926	6.3×10^{-6}	-14.2~14.9	Exp. 5~8	0.4894	-2.8~2.1
0.9-B	Exp. 1~4	0.6926	6.6×10^{-6}	-5.4~3.7	Exp. 5~8	0.3028	-18.3~43.8
1.05-B	Exp. 1~4	0.4326	0.0040	-1.9~1.4	Exp. 5~8	0.3686	-4.7~4.1

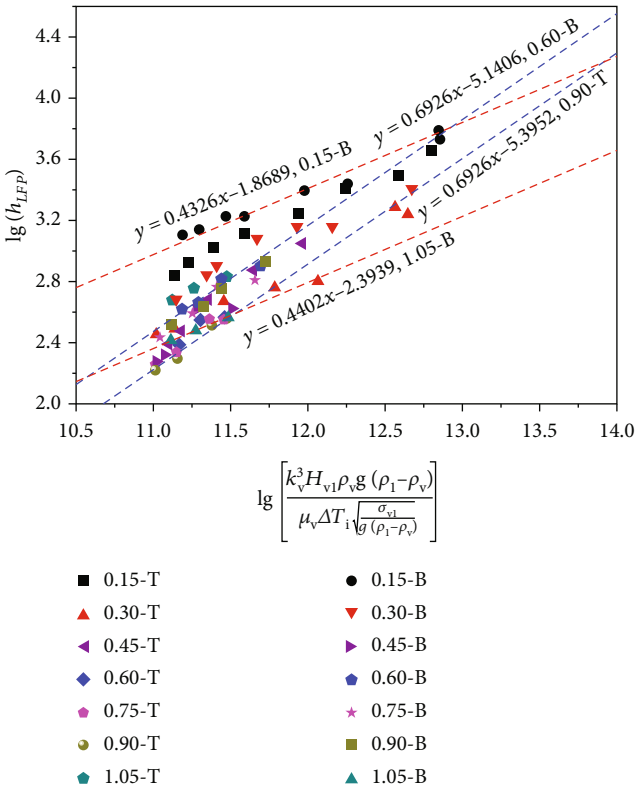

Figure 19: Correlation on h_{LFP}.

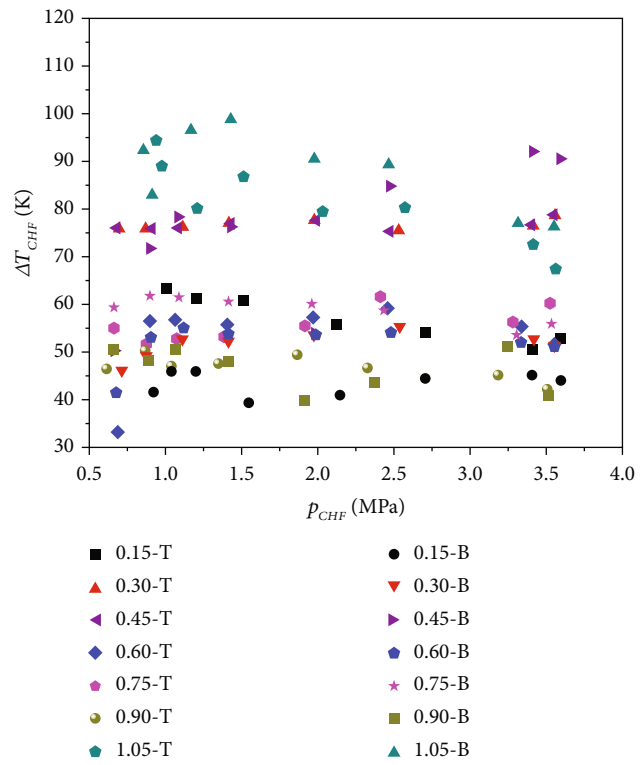

Figure 20: Experimental ΔT_{CHF} versus p_{CHF}.

to the 3rd type, the effect of pressure plays an increasing role on the increase of h_{LFP}.

For the 1st type, for Section II, Exp. 5~8 and Section III, Exp. 5~8 as shown in Table 4, h_{LFP} could be correlated via Equation (3). This equation is proven from film boiling originally [32]. The order of C_2 in Equation (3) as shown in Table 5 is similar with 0.425 in surface film boiling [32]. Here, because of liquid fill-in at high pressure, liquid rewetting would be obtained simultaneously on the various cross-sections in Sections II and III. This indicates that this sort of liquid rewetting is similar in mechanism with film boiling.

For the 2nd type, for Section I, Exp. 1~8 and Section III, Exp. 1~4 as shown in Table 4, h_{LFP} could be correlated via Equation (5). Here, cross-sections 0.15, 0.3, and 1.05 are similar with each other, on which the liquid rewetting is controlled by the propagation of the end (inlet or exit) QF. Both

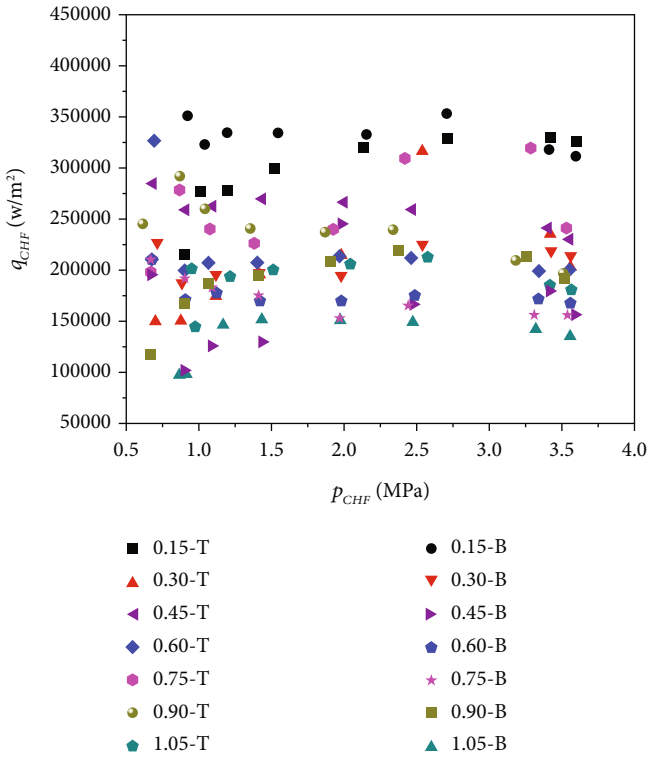

Figure 21: Experimental q_{CHF} versus p_{CHF}.

the inlet QF and the exit QF could be detected in the previous study [31].

$$h_{\mathrm{LFP}} = C_2 \left[\frac{k_{\mathrm{v}}^3 H_{\mathrm{vl}} \rho_{\mathrm{v}} g(\rho_{\mathrm{l}} - \rho_{\mathrm{v}})}{\mu_{\mathrm{v}} \Delta T_{\mathrm{i}} \sqrt{\sigma_{\mathrm{vl}} / g(\rho_{\mathrm{l}} - \rho_{\mathrm{v}})}} \right]^{0.4326}. \quad (5)$$

For the 3rd type, for Section II, Exp. 1~4 in Table 4, h_{LFP} could be correlated via Equation (6). Here, on these cross-sections, the liquid rewetting is controlled by the propagation of the 3rd QF and the 4th QF, which could be called the central QFs. They are always formed in Section II independently.

$$h_{\mathrm{LFP}} = C_2 \left[\frac{k_{\mathrm{v}}^3 H_{\mathrm{vl}} \rho_{\mathrm{v}} g(\rho_{\mathrm{l}} - \rho_{\mathrm{v}})}{\mu_{\mathrm{v}} \Delta T_{\mathrm{i}} \sqrt{\sigma_{\mathrm{vl}} / g(\rho_{\mathrm{l}} - \rho_{\mathrm{v}})}} \right]^{0.6926}. \quad (6)$$

5.3.2. The Effect of Factors. As shown in Figures 13 and 15, except the cross-sections of 0.45 m and 1.05 m, h_{LFP} values at the bottom are always higher than those at the top as shown in the figures. This indicates the effect of gravity, in which, for most cases, δ_{LFP} at the bottom is thinner than that at the top.

Basically, along the direction of QF propagation, h_{LFP} would undergo a decreasing manner. As shown in the figure, comparison shows that because of the propagation of the 1st QF, h_{LFP} values show the decreasing manner from cross-sections 0.15 m to 0.3 m. On the other hand, because of the

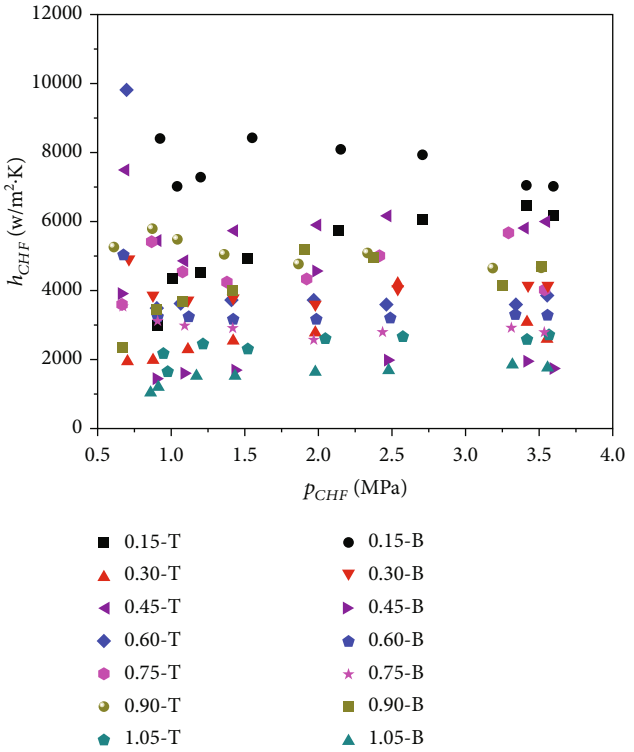

Figure 22: Experimental h_{CHF} versus p_{CHF}.

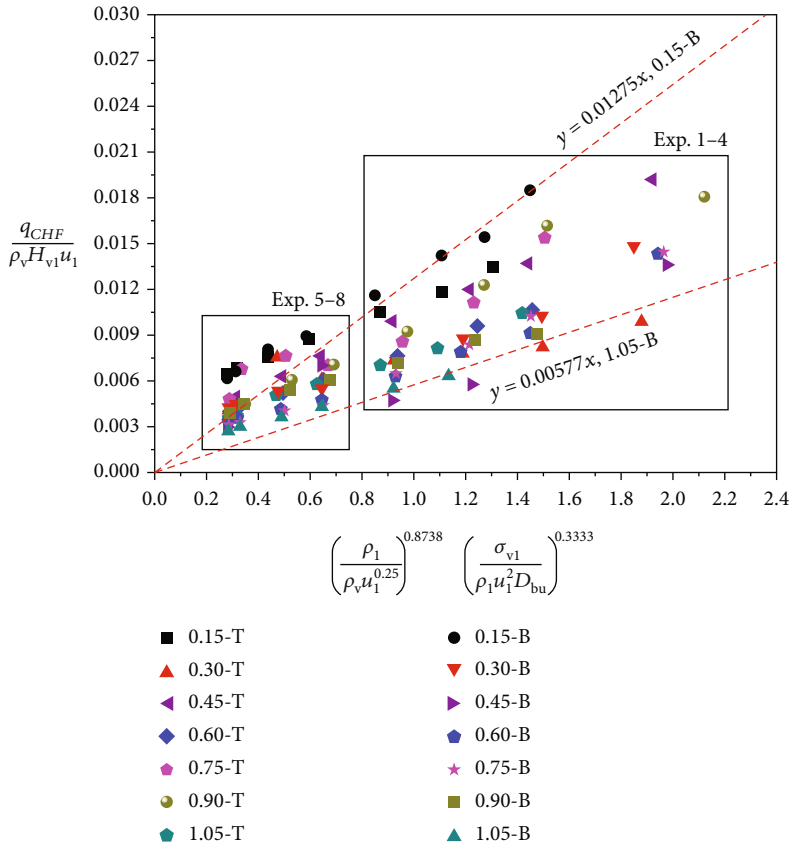

FIGURE 23: Correlation on q_{CHF} by Equation (7).

propagation of the 3rd and the 4th QF, h_{LFP} values show the decreasing manner from cross-sections 0.6 m to 0.75 m.

6. Critical Heat Flux

6.1. Basic Data. Figures 20–22 plot the data of ΔT_{CHF}, q_{CHF}, and h_{CHF} versus p_{CHF}, respectively, which show the basic effects of pressure on these parameters. As shown in the figures, with the increase of pressure, all of the parameters ΔT_{CHF}, q_{CHF}, and h_{CHF} show the overall constant manner, except for a few special points.

For LFP, the liquid rewetting is caused by the magnitude of the instable wave increase to the thickness of the vapor film. As a result, h_{LFP} is the dominant parameter compared to q_{LFP} and ΔT_{LFP}. However, for CHF, the basic bubble separation mechanism is that q_{CHF} supplied to the fluid could be completely used to supply the latent heat of the bubble vapor flow out from the inner wall. This indicates that q_{CHF} is the dominant parameter compared to h_{CHF} and ΔT_{CHF}. As shown in Figure 21, the effect of p_{CHF} on q_{CHF} in the present study is similar with that in the previous studies [30, 31].

Basically, with the increase of pressure, q_{CHF} values undergo the constant-decreasing manner for most of the points. The exceptions include the following.

(1) From Exp. 1 to Exp. 2, the variations that q_{CHF} values undergo do not show an obvious manner on some points. This is because Exp. 1 has been performed on different seasons from other tests. In this way, from the point of view of correlation, some points would be excluded

(2) For 0.9-B and 1.05-B, with the increase of pressure, q_{CHF} values undergo the constant-decreasing manner, which is different from the primary manner

(3) For 0.3-T, 0.45-B and 0.75-T, some q_{CHF} values are extremely higher than the others

6.2. Correlations on the Critical Heat Flux. In the previous studies, Equation (7) has been proven to predict q_{CHF} in the exit-contracted pipe. This equation has been validated for both horizontal and vertical pipes below around 2 MPa [30, 31]. In the present study, q_{CHF} data could be plotted versus the right side of Equation (7) as shown in Figure 23, where a few exception data have been excluded. As shown in the figure, it is evident that Equation (7) could give reliable predictions on the q_{CHF} data for the low-pressure condition (Exp 1~4) as discussed above, where the C_3 data is listed in Table 6. However, this equation could not give reliable predictions on q_{CHF} for the high-pressure condition as shown in Figure 23. As shown

Table 6: C_3 values and deviations.

Point	C_3 in Eq. (7)	Deviation (%)	C_3 in Eq. (9)	Deviation (%)
0.15-T	0.01086	-10.83~4.5	0.05248	-5.55~5.52
0.30-T	0.00586	-25.35~10.87	0.03551	-8.53~5.62
0.45-T	0.00997	-7.84~4.39	0.03996	-4.12~2.82
0.60-T	0.00765	-7.36~4.55	0.03300	-2.1~1.61
0.75-T	0.00962	-6.05~6.92	0.03917	-3.4~3.6
0.90-T	0.00937	-12.33-9.72	0.03494	-6.75~6
1.05-T	0.00755	-7.15~2.38	0.03148	-3.12~3.16
0.15-B	0.01275	-6.74~4.95	0.05278	-2.53~2.71
0.30-B	0.00759	-5.43~10.11	0.03415	-5.79~12.49
0.45-B	0.00616	-10.7~29.71	0.02968	-22.82~16.21
0.60-B	0.00694	-6.02~9.52	0.02735	-3.08~4.57
0.75-B	0.0072	-2.64~3.63	0.02523	-3.86~4.57
0.90-B	0.00677	-12.65~9.87	0.03334	-2.88~2.72
1.05-B	0.00577	-4.7~3.22	0.02312	-1.83~1.26

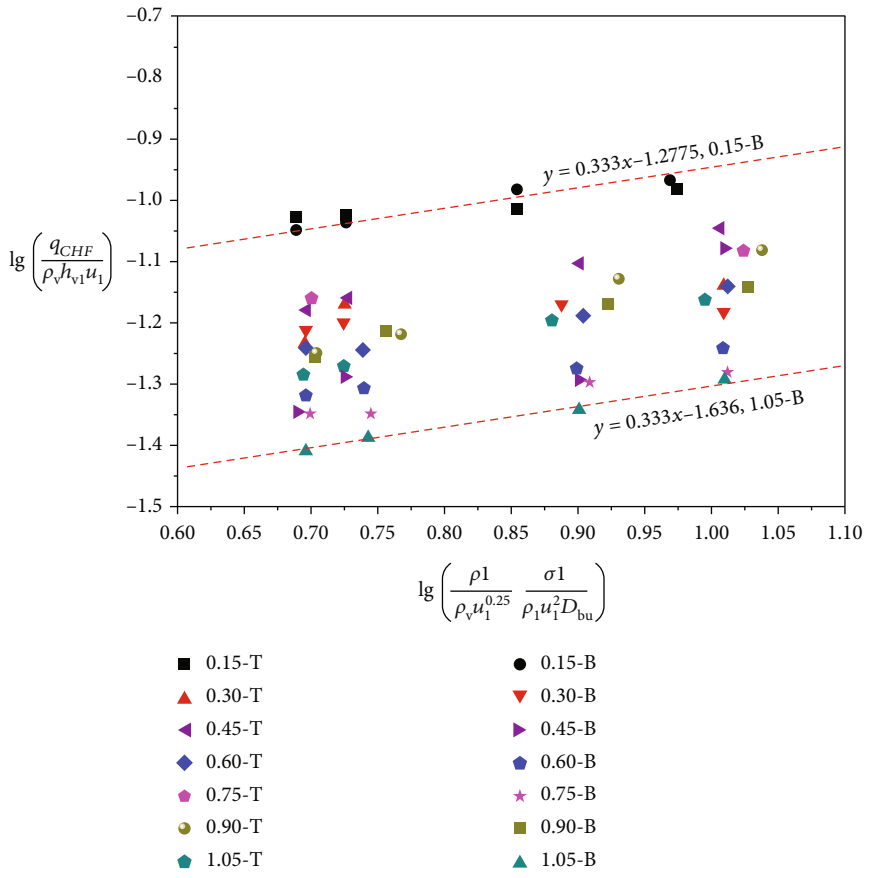

Figure 24: High-pressure condition.

in the figure, for the high-pressure condition, the slope is lower.

$$\frac{q_{\mathrm{CHF}}}{\rho_{\mathrm{v}} H_{\mathrm{vl}} u_{\mathrm{l}}} = C_3 \left(\frac{\rho_{\mathrm{l}}}{\rho_{\mathrm{v}} u_{\mathrm{l}}^{0.25}}\right)^{0.8738} \left(\frac{\sigma_{\mathrm{vl}}}{\rho_{\mathrm{l}} u_{\mathrm{l}}^2 D_{\mathrm{bu}}}\right)^{0.3333}. \quad (7)$$

In this way, the basic correlation on q_{CHF} proven in reference [30] should be given in Equation (8). For the high-pressure condition, the experimental q_{CHF} data could be correlated by Equation (8) as shown in Figure 24. Here, the exponent m has been correlated to be 0.333, and C_3 is correlated and listed in Table 6.

It shows that by Equation (9), q_{CHF} could be well predicted.

$$\frac{q_{CHF}}{\rho_v h_{vl} u_l}\left(\frac{\sigma_l}{\rho_l u_l^2 D_{bu}}\right)^{-1/3} = C_3\left(\frac{\rho_l}{\rho_v u_l^{0.25}}\right)^m, \quad (8)$$

$$\frac{q_{CHF}}{\rho_v h_{vl} u_l} = C_3\left(\frac{\rho_l}{\rho_v u_l^{0.25}}\right)^{0.333}\left(\frac{\sigma_l}{\rho_l u_l^2 D_{bu}}\right)^{0.333}. \quad (9)$$

6.3. Discussions

6.3.1. Correlation Approaches. Compared to h_{LFP}, the correlation of q_{CHF} is based on the pressure range. For the low-pressure condition (Exp. 1~4), q_{CHF} could be correlated by Equation (7), and for the high-pressure condition (Exp. 5~8), q_{CHF} could be correlated by Equation (9), where the constant is listed in Table 6.

6.3.2. The Effect of Factors. As shown in Figure 21, basically, q_{CHF} values on the top surface are higher than those on the bottom surface. This is because bubble separation is more difficult on the top surface [33].

Based on the discussions above, basically, along the propagation of BSF, q_{CHF} would undergo continuous decrease. As shown in Figure 21, on the low-pressure condition, q_{CHF} values undergo the obvious decreasing manner from cross-sections 0.15 m to 0.3 m. After that, on the low-pressure condition, q_{CHF} values undergo continuous increase on two sections, from 0.6-T to 0.9-T and from 0.45-B to 0.75-B. This is probably caused by the BSFs followed by the 3rd and 4th QFs.

For the high-pressure condition, q_{CHF} values undergo continuous decrease from 0.15-B to 0.9-T primarily, which is also consistent with the propagation of BSF as discussed in Section 4.4.

7. Conclusion

In the present study, the LO_2 chill-down in a straight horizontal pipe was studied experimentally. Compared to the previous studies, the effect of the entrance corner was excluded, and more dense wall temperature sensors along the pipe have been set. In this way, the chill-down process, as well as the development of the flow pattern, has been drawn for every test. As a result, the mechanism of the LO_2 chill-down would be obtained for various pressure sections. Based on the transition points obtained, h_{LFP} and q_{CHF} could be correlated by new approaches, where the basic parameter combinations are the same with the previous studies. Conclusions show that the correlation equations are dependent to the chill-down mechanisms. Detailed conclusions could be listed as follows.

(1) On the low-pressure condition (Exp. 1~4, $p_{ss} \le 1.25$ MPa), the decrease of T_i curves shows the linear-sharp-gradual manner, with the long linear (film boiling) section. In addition, the liquid rewettings in Sections I and III are controlled by the propagation of the end QF, and the liquid rewetting in Section II is controlled by the propagation of the QF produced in the present section. Every QF would produce the corresponding BSF, which controls the bubble separation in the present section

(2) On the high-pressure condition (Exp. 5~8, $p_{ss} \ge 1.25$ MPa), the decrease of the T_i curve shows the linear-accelerated-gradual manner, with the long accelerated (transition boiling) section. In addition, the liquid rewetting in Section I is controlled by the propagation of the inlet QF, and the liquid rewetting in other sections is controlled by the sudden fill-in of the liquid. Bubble separation in Section III is obviously caused by the exit BSF following the exit QF. However, in other sections, it is controlled more likely by the propagation of the inlet BSF following the inlet QF

(3) For Sections II and III, Exp. 5~8 as shown in Table 4, h_{LFP} could be correlated by Equation (3), which is consistent to the liquid rewetting mechanism, which is a sudden liquid fill-in. For Section I, Exp. 1~8 and Section III, Exp. 1~4 in Table 4, h_{LFP} could be correlated by Equation (5), which corresponds to the related controlling factor, the propagation of the end QFs. For other cases, h_{LFP} could be predicted by Equation (6), which is consistent with the controlling factor, the propagation of the central QFs

(4) Based on the previous correlation format [30], Equations (7) and (9) are proven to predict q_{CHF} for the low-pressure condition and high-pressure condition, respectively. Both the present q_{CHF} data and constant C_3 for the low-pressure condition show obvious consistency with those from the L-shaped horizontal pipe and Z-shaped vertical pipe

Nomenclature

A: Area, m^2
B: Parameter combination in correlations
C: Constant in correlations
c: Specific heat, $J \cdot kg^{-1} \cdot K^{-1}$
D: Diameter, m
E: Parameter combination in correlations
G: Mass flux in the experimental section, $kg \cdot m^{-2} \cdot s^{-1}$
g: Gravity acceleration, $m \cdot s^{-2}$
H: Latent heat or enthalpy, $J \cdot kg^{-1}$
h: Heat transfer coefficient, $W \cdot m^{-2} \cdot K^{-1}$
k: Heat conductivity, $W \cdot m^{-1} \cdot K^{-1}$, or constant in k_{FZ}
L: Distance, m
$\dot{m}$: Mass flow rate, $kg \cdot s^{-1}$
N: Number of data
p: Pressure, Pa
Pr: Prandtl number, $c_p \cdot \mu \cdot k^{-1}$
q: Heat flux, $W \cdot m^{-2}$
Re: Reynolds number, $D_i G \cdot \mu_l^{-1}$
T: Temperature, K

t: Time, s
u: Velocity, m/s
V: Variables mainly represent T_{LFP}, q_{LFP}, T_{CHF}, and q_{CHF} data.

Subscripts

bu: The bubble
CHF: Critical heat flux point
cr: Critical properties
exp: Experimental data
FZ: Forster-Zuber parameter
FB: Film boiling
i: The inner wall of the pipe
inj: Injector on the pipe exit
LFP: Inner wall data of the Leidenfrost point
l: Liquid phase
NB: Nuclear boiling
o: The outer wall of the pipe
p: Fluid in the experimental section or constant pressure in c_p
peak: Value of the pressure peak
pre: Predicted data by correlations
s: The solid material
sat: Saturation condition
se: From main valve to outer wall temperature sensors
si: Saturation parameter on inner wall temperature
ss: Steady-state condition, the chill-down finishes
v: Vapor phase
vl: From vapor phase to liquid phase.

Greek Symbols

μ: Viscosity, Pa·s
ρ: Density, kg·m^{-3}
σ: Surface tension, N·m^{-1}
δ: Thickness of film, m.

Data Availability

Data have been uploaded via "supplemental files" with the manuscript file.

Conflicts of Interest

The authors declare that they have no conflicts of interest.

Acknowledgments

This study was funded by the National Natural Science Foundation of China (grant number T2221002).

Supplementary Materials

In the "Supplementary files" section, a file named "Data_A," including the LFP and CHF data in the format of a table, has been uploaded with the manuscript. All the related data on boiling transition points, both LFP and CHF, are listed in Tables 1 and 2, respectively, of the file. In Table 1, p_{LFP} (pressure on LFP), q_{LFP} (inner wall heat flux on LFP), t_{LFP} (time spent from LFP to chill-down starting), T_{LFP} (inner wall temperature on LFP), T_{sat} (saturation temperature corresponding to p_{LFP}), and h_{LFP} (inner wall heat transfer coefficient on LFP) are listed for all of the 14 points for Exp. 1~8. In this way, both vapor properties and liquid properties could be determined for these points from Exp. 1~8. In Table 2, p_{CHF} (pressure on CHF), q_{CHF} (inner wall heat flux on CHF), t_{CHF} (time spent from CHF to chill-down starting), T_{CHF} (inner wall temperature on CHF), T_{sat} (saturation temperature corresponding to p_{CHF}), and h_{CHF} (inner wall heat transfer coefficient on CHF) are listed for all of the 14 points for Exp. 1~8. In this way, both vapor properties and liquid properties could be determined for these points from Exp. 1~8. *(Supplementary Materials)*

References

[1] D. Conte, D. Budzyn, H. Burgoyne et al., "Innovative Mars Global International Exploration (IMaGInE) mission-first place winning paper," in *AIAA SPACE*, p. 5596, Long Beach, California, 2016.

[2] E. A. Hurlbert, H. Ueno, L. Alexander et al., "International space exploration coordination group assessment of technology gaps for LOX/methane propulsion systems for the global exploration roadmap," in *AIAA SPACE 2016*, p. 5280, Long Beach, California, September 2016.

[3] P. Cui, Q. Li, P. Cheng, and L. Chen, "System scheme design for LOX/LCH4 variable thrust liquid rocket engines using motor pump," *Acta Astronautica*, vol. 171, pp. 139–150, 2020.

[4] L. Yin, E. Jiaqiang, J. Ding, and Y. Li, "An experimental study on the spray characteristics of splash platelet injector," *Acta Astronautica*, vol. 181, pp. 377–383, 2021.

[5] J. Hartwig, S. Darr, and A. Asencio, "Assessment of existing two phase heat transfer coefficient and critical heat flux correlations for cryogenic flow boiling in pipe quenching experiments," *International Journal of Heat and Mass Transfer*, vol. 93, pp. 441–463, 2016.

[6] J. N. Chung, J. Dong, H. Wang, S. R. Darr, and J. W. Hartwig, "Enhancement of convective quenching heat transfer by coated tubes and intermittent cryogenic pulse flows," *International Journal of Heat and Mass Transfer*, vol. 141, pp. 256–264, 2019.

[7] J. N. Chung, S. R. Darr, J. Dong, H. Wang, and J. W. Hartwig, "Heat transfer enhancement in cryogenic quenching process," *International Journal of Thermal Sciences*, vol. 147, article 106117, 2020.

[8] L. Zhou, T. Pan, H. Wang, D. Liu, and P. Wang, "Rapid air expulsion through an orifice in a vertical water pipe," *Journal of Hydraulic Research*, vol. 57, no. 3, pp. 307–317, 2019.

[9] L. Zhou, H. Wang, B. Karney, D. Liu, P. Wang, and S. Guo, "Dynamic behavior of entrapped air pocket in a water filling pipeline," *Journal of Hydraulic Engineering*, vol. 144, no. 8, p. 04018045, 2018.

[10] L. Jin, C. Park, H. Cho, C. Lee, and S. Jeong, "Experimental investigation on chill-down process of cryogenic flow line," *Cryogenics*, vol. 79, pp. 96–105, 2016.

[11] L. Jin, H. Cho, C. Lee, and S. Jeong, "Experimental research and numerical simulation on cryogenic line chill-down process," *Cryogenics*, vol. 89, pp. 42–52, 2018.

[12] L. Jin, H. Cho, and S. Jeong, "Experimental investigation on line chill-down process by liquid argon," *Cryogenics*, vol. 97, pp. 31–39, 2019.

[13] L. Jin, J. Lee, and S. Jeong, "Investigation on heat transfer in line chill-down process with various cryogenic fluids," *International Journal of Heat and Mass Transfer*, vol. 150, article 119204, 2020.

[14] H. Hu, J. N. Chung, and S. H. Amber, "An experimental study on flow patterns and heat transfer characteristics during cryogenic chilldown in a vertical pipe," *Cryogenics*, vol. 52, no. 4-6, pp. 268–277, 2012.

[15] S. R. Darr, H. Hu, N. G. Glikin et al., "An experimental study on terrestrial cryogenic transfer line chilldown I. Effect of mass flux, equilibrium quality, and inlet subcooling," *International Journal of Heat and Mass Transfer*, vol. 103, pp. 1225–1242, 2016.

[16] S. R. Darr, H. Hu, N. Glikin et al., "An experimental study on terrestrial cryogenic tube chilldown II. Effect of flow direction with respect to gravity and new correlation set," *International Journal of Heat and Mass Transfer*, vol. 103, pp. 1243–1260, 2016.

[17] S. R. Darr, J. W. Hartwig, J. Dong et al., "Two-phase pipe quenching correlations for liquid nitrogen and liquid hydrogen," *Journal of Heat Transfer*, vol. 141, no. 4, p. 4, 2019.

[18] J. Wang, Y. Li, L. Wang, K. Zhu, F. S. Xie, and C. Li, "Transient modeling of cryogenic two-phase flow boiling during chill-down process," *Applied Thermal Engineering*, vol. 143, pp. 461–471, 2018.

[19] J. Wang, Y. Li, L. Wang, H. Mao, Y. Ma, and F. S. Xie, "Experimental investigation on two-phase flow instabilities in long-distance transportation of liquid oxygen," *Cryogenics*, vol. 102, pp. 56–64, 2019.

[20] L. Wang, J. Wang, X. Huang et al., "Experimental investigation on cryogenic chilldown performance under high-Reynolds number condition and using interior micro-fin structure," *International Journal of Heat and Mass Transfer*, vol. 182, article 121979, 2022.

[21] W. Xu and P. Zhang, "Cryogenic quenching of a stainless steel rodlet with various coatings," *International Journal of Heat and Mass Transfer*, vol. 154, article 119642, 2020.

[22] W. Xu, C. Cheng, X. Song, and P. Zhang, "Experimental investigation of cryogenic flow quenching of horizontal stainless steel tubes," *Cryogenics*, vol. 117, article 103327, 2021.

[23] J. Hartwig, P. Meyerhofer, B. Stiegemeier, and R. Morehead, "Liquid methane and liquid oxygen horizontal chilldown experiments of a 2.54 and 11.43 cm transfer line," *Applied Thermal Engineering*, vol. 205, article 118042, 2022.

[24] S. R. Darr, H. Hu, R. Shaeffer, J. Chung, J. W. Hartwig, and A. K. Majumdar, "Numerical simulation of the liquid nitrogen chilldown of a vertical tube," in *53rd aiaa aerospace sciences meeting*, Kissimmee, Florida, 2015.

[25] J. Chen, R. Zeng, X. Zhang, L. Qiu, and J. Xie, "Numerical modeling of flow film boiling in cryogenic chilldown process using the AIAD framework," *International Journal of Heat and Mass Transfer*, vol. 124, pp. 269–278, 2018.

[26] J. C. Melcher and R. L. Morehead, "Combustion stability characteristics of the Project Morpheus liquid oxygen/liquid methane main engine," in *50th AIAA/ASME/SAE/ASEE Joint Propulsion Conference*, Cleveland, OH, 2014.

[27] M. Leonardi, F. Di Matteo, J. Steelant, F. Nasuti, and M. Onofri, "System analysis of low frequency combustion instabilities in liquid rocket engines," in *51st AIAA/SAE/ASEE Joint Propulsion Conference*, Orlando, FL, 2015.

[28] J. Zhang, K. Wang, and L. Chen, "Experimental study on liquid oxygen chilldown in the horizontal pipe with an injector on the exit," *Applied Thermal Engineering*, vol. 173, article 115212, 2020.

[29] J. Zhang, K. Wang, and L. Chen, "Characteristics of boiling transitions during liquid oxygen chill-down in a horizontal pipe with an injector on the exit," *Applied Thermal Engineering*, vol. 182, article 116068, 2021.

[30] J. Zhang, K. Wang, and L. Chen, "Experimental study on liquid oxygen chill-down in a horizontal exit-contracted pipe," *Cryogenics*, vol. 120, article 103387, 2021.

[31] J. Zhang, K. Wang, and L. Chen, "Fill-in and boiling transition characteristics during the liquid oxygen chill-down process in a vertical exit-contracted pipe," *International Journal of Aerospace Engineering*, vol. 2022, Article ID 5899199, 22 pages, 2022.

[32] P. J. Berenson, "Film-boiling heat transfer from a horizontal surface," *Journal of Heat Transfer*, vol. 83, no. 3, pp. 351–356, 1961.

[33] D. D. Hall and I. Mudawar, "Critical heat flux (CHF) for water flow in tubes–I. Compilation and assessment of world CHF data," *International Journal of Heat and Mass Transfer*, vol. 43, no. 14, pp. 2573–2604, 2000.

[34] K. Yuan, Y. Ji, and J. N. Chung, "Numerical modeling of cryogenic chilldown process in terrestrial gravity and microgravity," *International Journal of Heat and Fluid Flow*, vol. 30, no. 1, pp. 44–53, 2009.

Hindawi
International Journal of Aerospace Engineering
Volume 2022, Article ID 2152543, 8 pages
https://doi.org/10.1155/2022/2152543

Research Article

Effect of Hydrophilicity/Hydrophobicity of the Injector Wall on Atomization Performance

Xiaoyu Zhang[1], **Xiaolei Zhang**[1], **Runze Duan**[1,2] **and Lujia Liu**[3]

[1]*School of Energy and Environmental Engineering, Hebei University of Technology, Tianjin 300401, China*
[2]*Hebei Key Laboratory of Thermal Science and Energy Clean Utilization, Tianjin 300401, China*
[3]*Institute of Fundamental Technological Research, Polish Academy of Sciences, Pawińskiego 5b, 02-106 Warsaw, Poland*

Correspondence should be addressed to Runze Duan; duanrunze@hebut.edu.cn

Received 17 June 2022; Accepted 23 August 2022; Published 4 October 2022

Academic Editor: Yiheng Tong

Hydrophilicity/hydrophobicity is a common physical property of the material. Water droplets roll on lotus leaf, and a lot of dust and dirt on the surface of the lotus leaf will be taken away, playing a certain cleaning role. The hydrophobic surface has drag reduction effect that would produce slip on the hydrophobic wall. There are some studies on hydrophilicity/hydrophobicity in channels, most of which focus on the effect of surface drag reduction and heat transfer on microchannels. However, few people pay attention to the effect of the hydrophilicity/hydrophobicity of the injector inner wall on the atomization performance. In this paper, three groups of the open-end swirl injector with different tangential channels were designed to study the effect of hydrophilicity/hydrophobicity on atomization performance. The hydrophobic coating was prepared and used on the inner wall of the injector, and the atomization experimental system was built. In the experiment, the liquid film thickness was measured using the conductance method. Details of the liquid film breakup and spray development were recorded with a high-speed camera. The average droplet diameter was measured by the Malvern particle size analyzer. The atomization performance of injectors with different tangential channels on the hydrophilicity/hydrophobicity was compared, and the effect of the velocity profile on the jet stability is discussed.

1. Introduction

The hydrophilicity/hydrophobicity of the solid wall reflects the different characteristics of the liquid and the solid contact. The liquid will fit better on the hydrophilic wall with the solid wall but the liquid will slip on the hydrophobic wall. When the liquid droplet rolls on the solid wall, it will remove stains on the solid wall, which make that hydrophobic wall has self-cleaning property. The hydrophobic surface has drag reduction effect, which causes a slip flow at the solid-liquid interface, and the velocity gradient at the interface is reduced, so that the laminar flow state of the attachment surface is kept more stable and the shear force at the solid-liquid interface is reduced. Some chemical reactions on the substrate will make the substrate hydrophobic [1–4], thus achieving the purpose of the artificially preparing a hydrophobic coating. Yamashita et al. [5] firstly prepared the superhydrophobic surfaces and carried out the experimental research. They sprayed a layer of the photocatalyst with TiO_2 as the main material on the surface of the polytetrafluoroethylene (ordinary hydrophobic material) and finally obtained a superhydrophobic surface. The surface has the "automatic cleaning" feature, and the liquid can roll freely on the surface and carry away stains. Cremaldi and Bhushan [6] used a chemical etching method to create a micro-nanostructure on the surface of the stainless steel, which hydrophobizes the surface of the stainless steel. Vilaio and Yague [7] conducted a hydrophobic surface preparation experiment for the copper sheets. This experiment used a chemical etching method to etch a micron-scale roughness on the surface of the copper, and the coating can effectively

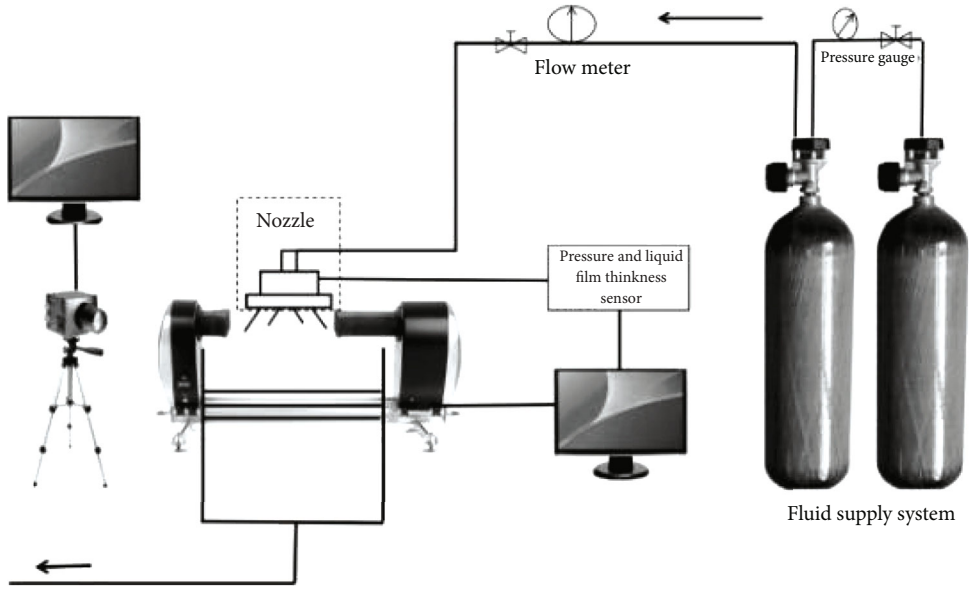

Figure 1: Experimental system.

Table 1: Properties of experimental equipment.

Equipment	Measurement range	Precision
Flow meter	0–0.4 m^3/h	±1%
Pressure gauge	0–1 MPa	0.5%

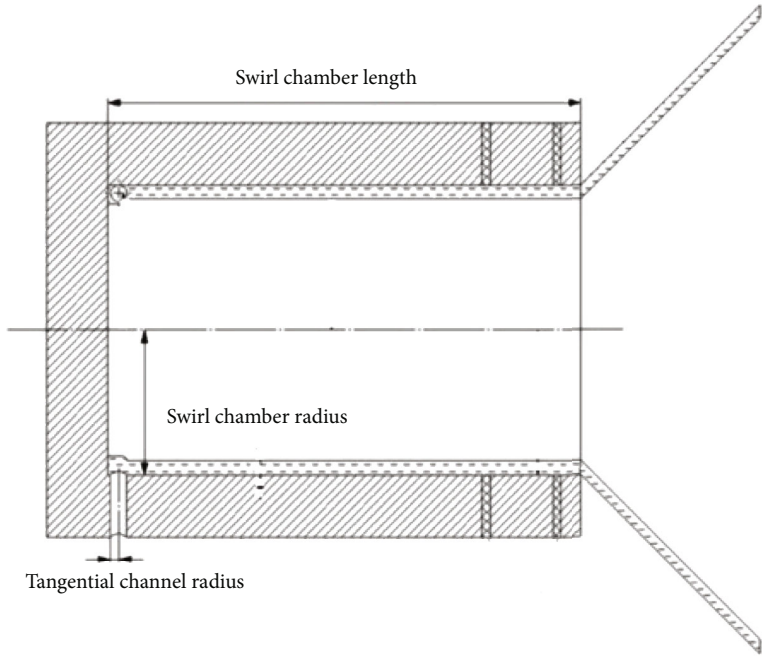

Figure 2: Open-end swirl injector.

protect the copper substrate and the display excellent corrosion resistance. Nine et al. [8] developed a new type of the composite hydrophobic coating, which was mainly prepared by mixing polydimethylsiloxane (PDMS), diatomaceous earth, and reduced graphene oxide (rGO). Sungnam et al. [9] found that the surface of the conventional channel can exhibit an obvious flow drag reduction effect after $Re < 200000$ on the surface after the superhydrophobic treatment. Using the drag reduction characteristics of the superhydrophobic surfaces, Rosengarten et al. [10] studied the effects of the contact angle

Table 2: Injector structure parameters.

Number	Tangential channel radius (mm)	Swirl chamber radius (mm)	Swirl chamber length (mm)
Injector 1	1.35	8.00	43.5
Injector 2	1.10	8.00	43.5
Injector 3	0.90	8.00	43.5

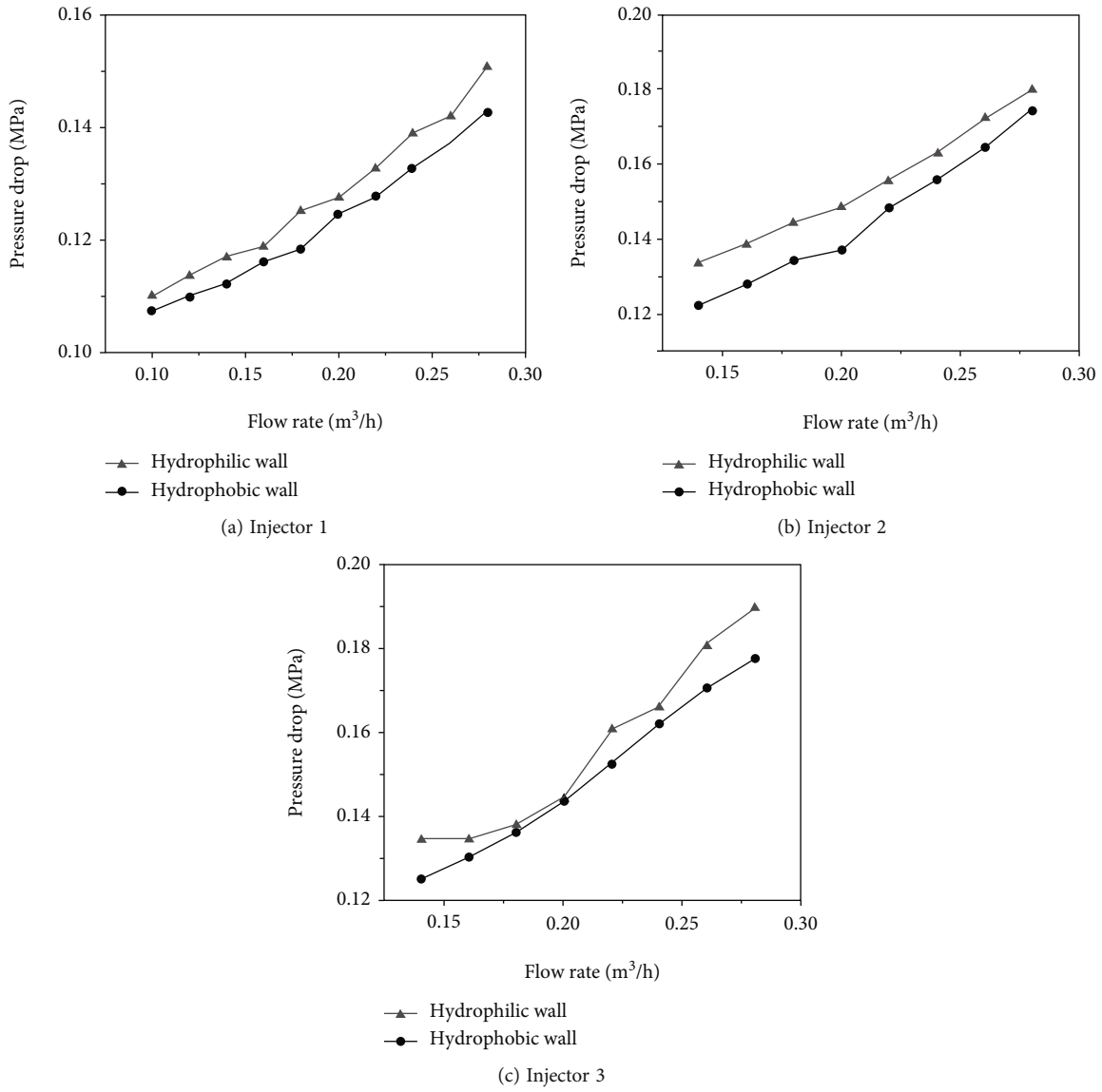

Figure 3: Effect of the flow rate on the injector pressure drop in different injectors.

Figure 4: Extraction of the spray cone angle.

on the inner wall of the microchannels on the single relative flow heat transfer and water flowing. Studying the performance of the hydrophobic surfaces requires consideration of the effect of the surface roughness on the hydrophobic properties with two different models, the Wenzel model [11] and the Cassie model [12] which show different contact states between the droplet and the solid surface.

Many designs of the rocket engines have high requirements on the drag reduction performance of the material surface

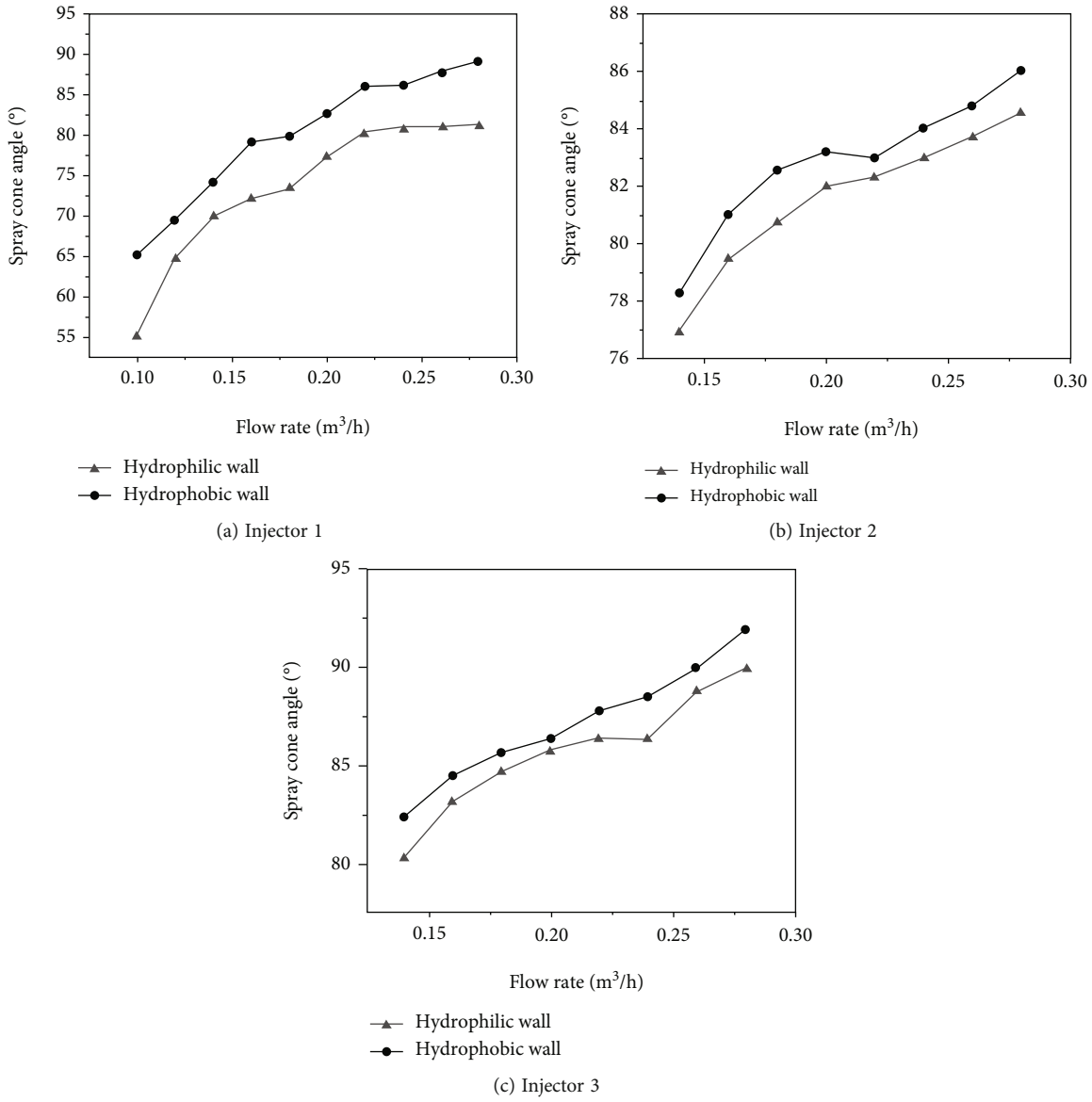

Figure 5: Effect of the flow rate on the injector spray cone angle in different injectors.

[13–15], but the application of the hydrophobic surfaces on the engine has not been carried out. Many studies focus on the liquid film breaking mechanism and the atomization characteristics of the normal surface, but the effect of the hydrophobic surfaces on the atomization has not received much attention. In this paper, three groups of the open-end swirl injectors with different tangential channels were designed to study the effect of the hydrophilicity/hydrophobicity on the atomization performance.

2. Experimental System

In this paper, a superhydrophobic nanoclear coating solution [16, 17] is used as a raw material for the hydrophobic coating. Inorganic nanoparticles, dispersant, crosslinking agent, etc. are sequentially added in an organic solvent and ultrasonically dispersed to obtain the hydrophobic coating. Hydrophobic coating is prepared by immersing the injector in a uniformly mixed coating solution. The contact angle reflects the hydrophobic properties of the hydrophobic wall, and the larger the surface contact angle is, the better the hydrophobic properties are. The surface contact angle of the injector treated with the above hydrophobic solution was 117.76°, which was considered to meet the hydrophobic requirements.

The experimental system is shown in Figure 1. In this experiment, the flow rate was adjusted by the valve near the flow meter and pressure drop was measured by the pressure gauge, which was the pressure difference between the injector inlet and outlet. The picture of the spray field during the atomization process was taken by the high-speed camera and saved to the computer. At the same time, the data was collected by the data acquisition system. The data acquisition system includes the pressure sensor, the voltage signal, and the liquid film thickness sensor connected to the injector. The average

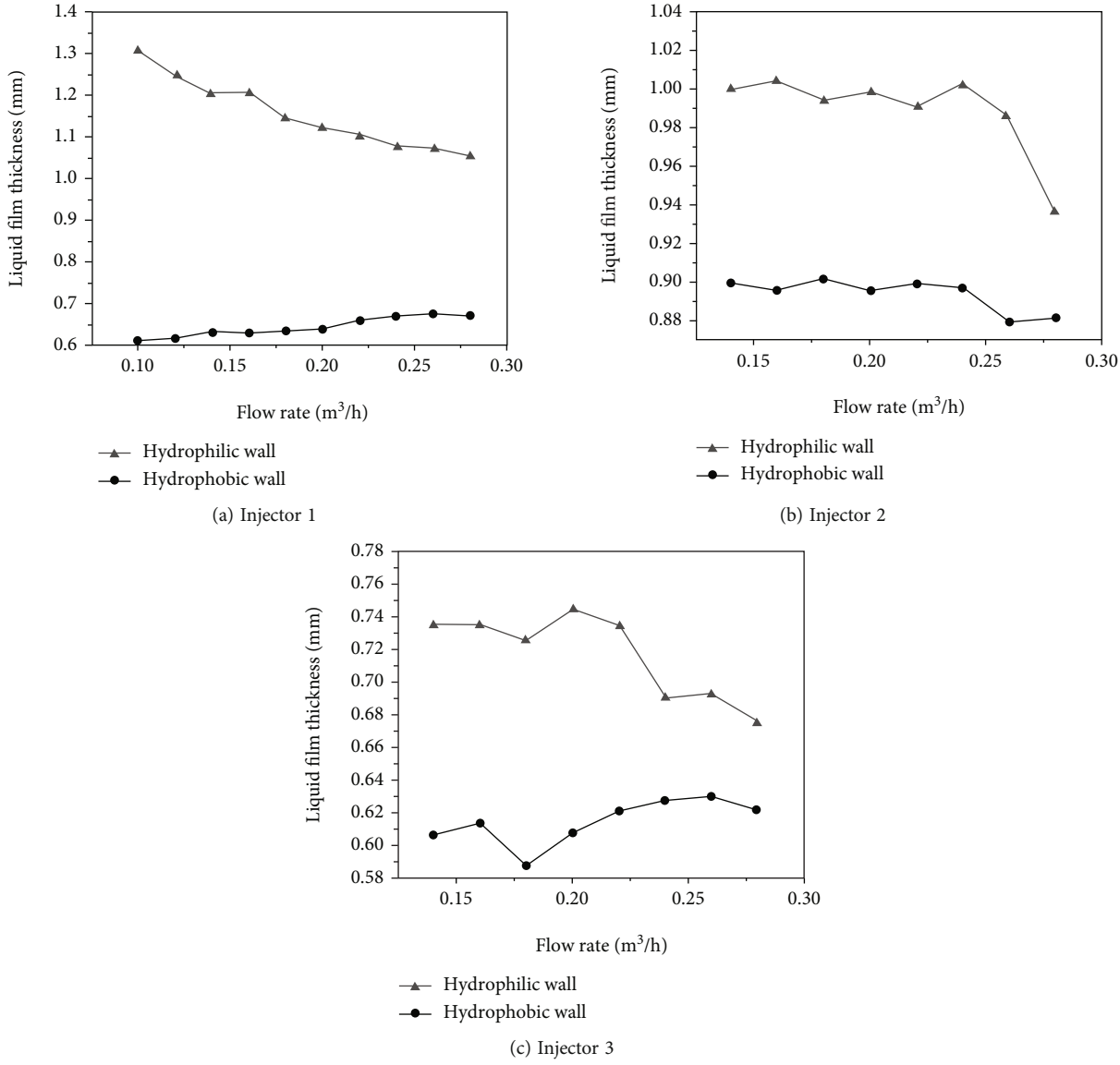

Figure 6: Effect of the flow rate on liquid film thickness in different injectors.

droplet diameter was measured by the Malvern particle size analyzer. The parameters of the flowmeter and the pressure gauge are shown in Table 1. When the flow rate reached 0.3 m^3/h in the experiment, the hydrophilic/hydrophobic wall pressure signal began to converge and the hydrophobic coating was considered to be detached, so the maximum flow rate of the hydrophobic coating is 0.3 m^3/h. The flow range in the paper is 0.1 m^3/h–0.3 m^3/h.

Figure 2 shows the test injector that is an open-end swirl injector with three different tangential channels, and the geometric parameters are shown in Table 2. The swirl intensity of the injectors was changed by the variety of the tangential channel radius.

3. Results and Discussion

3.1. Effect of the Flow Rate on the Injector Pressure Drop. Figure 3 shows the change in injector pressure drop for different tangential channels. It can be seen that the pressure drop inside the injector increases with the increase of the flow rate of the liquid. While comparing the hydrophobic the pressure drop with the hydrophilic pressure drop, it can be found that the pressure drop inside the hydrophobic injector will be smaller than that of the hydrophilic injector under the same conditions. The hydrophobic coating can cause the fluid flowing through the inner wall surface of the injector to slip and reduce the resistance, thereby decreasing the pressure drop inside the injector. The pressure drop increases with the decrease of the tangential channel radius of the injector for three different injectors in Figure 3.

3.2. Effect of the Flow Rate on the Injector Spray Cone Angle. The atomization process was photographed with a high-speed camera to obtain a photograph of the spray field, as shown in Figure 4. The shooting frame rate is 2000 fps,

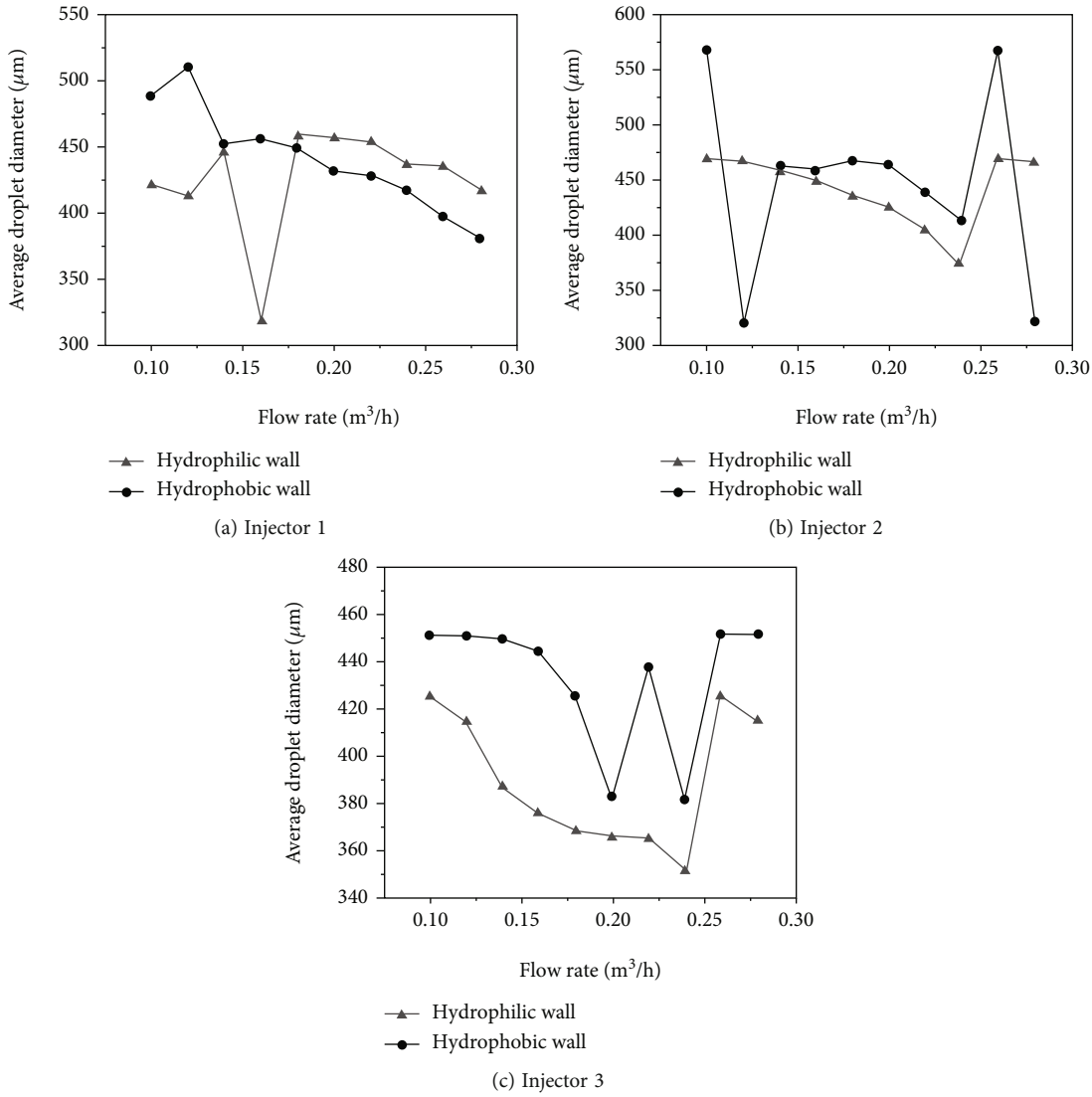

Figure 7: Effect of the flow rate on the average droplet diameter in different injectors.

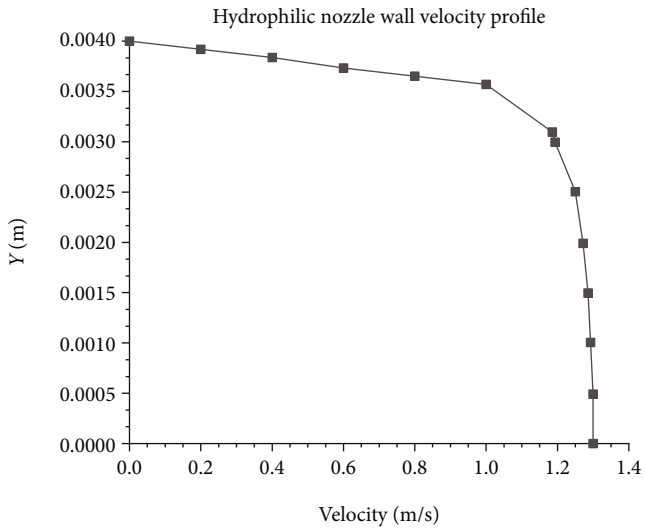

Figure 8: Hydrophilic wall velocity profile.

and the minimum exposure time is 20 μs. The image in the stable interval during the atomization process was obtained. The obtained image was binarized to obtain a spray angle boundary, thereby obtaining a spray cone angle. The effect of the flow rate on the injector spray cone angle for different tangential channels is shown in Figure 5. It shows that the spray cone angle of the hydrophilic injector and the hydrophobic injector increase with the increase of the flow rate, and the spray cone angle of the hydrophobic injector comparing the angle with the hydrophilic injector, it can be found that the spray cone angle of the hydrophobic injector becomes larger than that of the hydrophilic injector as wall surface slips.

3.3. Effect of the Flow Rate on Liquid Film Thickness. The conductance measurement method was used to determine the thickness of the liquid film [18–21]. The effect of flow rate on liquid film thickness at different flow rates was shown in Figure 6. It can be seen that the liquid film thickness of three injectors decreases with the increase of the flow rate. The liquid film thickness of the hydrophobic injector is

smaller than that of the hydrophilic injector under the same working condition as the hydrophobic inner wall surface reduces the velocity loss of the fluid.

3.4. Effect of the Flow Rate on the Average Droplet Diameter. The Malvern particle sizer is used to measure the average diameter of the droplets during the atomization, which can measure particles with a diameter in the range of 0–900 μm. The change in the diameter of the droplet determines whether the hydrophobic coating will have an effect on atomization. The effect of the flow rate on the average droplet diameter was investigated in Figure 7. By comparing the experimental results of three injectors, it can be found that the average droplet diameter of the hydrophobic injector is larger than that of the hydrophilic injector in the range of 0.1 m^3/h~0.18 m^3/h in injector 1 (the tangential channel diameter is 2.7 mm), but in the range of 0.18 m^3/h~0.28 m^3/h, the average diameter of the droplets of the hydrophobic injector is smaller than that of the hydrophilic injector; injector 2 (the tangential channel diameter is 2.2 mm) and injector 3 (the tangential channel diameter is 1.8 mm) can be seen that the droplet diameter of the hydrophobic injector is substantially larger than that of the hydrophilic injector. It is found that the average diameter of the droplets decreases with the increase of the flow rate, indicating that the increase of the flow rate reduces the average diameter of the droplet and increases the total surface area of the droplet.

3.5. Velocity Profile of the Liquid Film on the Hydrophilic Wall. The velocity profile of the injector wall affects the stability of the jet [22], [23]. The difference of the velocity profile of the hydrophilic walls was investigated by numerical simulation in Figure 8. The velocity profile of the hydrophilic wall is similar to the parabolic jet velocity profiles as the jet velocity of the hydrophobic wall is very gentle. Flowing with a fully developed parabolic velocity profile, the kinetic energy of the fluid is exactly twice what it would be if the fluid was ideal (plug flow) and flowing at the same average velocity. The velocity profile of the hydrophobic wall surface will make the jet more stable than that of the hydrophilic wall surface. As the result, for the average diameter of the droplets, the hydrophobic wall has different effects on the atomization performance in different flow ranges.

4. Conclusions

In this paper, the atomization experiments of the hydrophilic/hydrophobic injectors were carried out using three different tangential channel centrifugal injectors. The following can be found:

(1) The injector pressure drop after the hydrophobic treatment is decreased, the spray cone angle is increased, and the liquid film thickness is decreased

(2) The average diameter of the droplets has different changes at different flow rates

(3) The effect of the velocity profile on jet stability is discussed. The velocity profile of the hydrophobic wall surface will make the jet more stable than that of the hydrophilic wall surface

Data Availability

The data that support the findings of this study are available from the corresponding author upon reasonable request.

Conflicts of Interest

The authors declare that they have no conflicts of interest.

Acknowledgments

This research was supported by the National Natural Science Foundation of China (Support no. 12042211), Natural Science Foundation of Hebei (nos. A2022202010 and E2019202460), Tianjin Science and Technology Program (nos. 22YDTPJC00200 and 19YFZCSF00850), Key Research Program Projects of Hebei Province (no. 19274502D), and Industrial Technology Research of Hebei University of Technology (no. ZBYJY201902) which are gratefully acknowledged.

References

[1] M. Drouin, J. L. Arenas, and J. F. Paquin, "Incorporating a monofluoroalkene into the backbones of short peptides: evaluating the impact on local hydrophobicity," *ChemBioChem*, vol. 20, no. 14, pp. 1817–1826, 2019.

[2] A. V. Rao, M. M. Kulkarni, and S. D. Bhagat, "Transport of liquids using superhydrophobic aerogels," *Journal of Colloid and Interface Science*, vol. 285, no. 1, pp. 413–418, 2005.

[3] H. M. Shang, Y. Wang, S. J. Limmer, T. P. Chou, K. Takahashi, and G. Z. Cao, "Optically transparent superhydrophobic silica-based films," *Thin Solid Films*, vol. 472, no. 1-2, pp. 37–43, 2005.

[4] M. Karthika, H. Chi, T. D. Li, H. J. Wang, and S. Thomas, "Super-hydrophobic graphene oxide-azobenzene hybrids for improved hydrophobicity of polyurethane," *Composites Part B: Engineering*, vol. 173, article 106978, 2019.

[5] H. Yamashita, H. Nakao, M. Takeuchi, Y. Nakatani, and M. Anpo, "Coating of TiO_2 photocatalysts on superhydrophobic porous teflon membrane by an ion assisted deposition method and their self- cleaning performance," *Nuclear Instruments and Methods in Physics Research Section B: Beam Interactions with Materials and Atoms*, vol. 206, pp. 898–901, 2003.

[6] J. Cremaldi and B. Bhushan, "Fabrication of bioinspired, self-cleaning superliquiphilic/phobic stainless steel using different pathways," *Journal of Colloid and Interface Science*, vol. 518, pp. 284–297, 2018.

[7] I. Vilaio and J. L. Yague, "Superhydrophobic copper surfaces with anticorrosion properties fabricated by solventless CVD methods," *ACS Applied Materials & Interfaces*, vol. 9, no. 1, pp. 1057–1065, 2017.

[8] M. J. Nine, M. A. Cole, L. Johnson, D. N. H. Tran, and D. Losic, "Robust superhydrophobic graphene-based composite coatings with self–cleaning and corrosion barrier properties," *ACS Applied Materials & Interfaces*, vol. 7, no. 51, pp. 28482–28493, 2015.

[9] L. Sungnam, C. N. Dang, and K. Dongseob, "Experimental drag reduction study of super-hydrophobic surface withdual-scale structures," *Applied Surface Science*, vol. 286, pp. 206–211, 2013.

[10] G. Rosengarten, J. Cooper-White, and G. Metealfe, "Experimental and analytical study of the effect of contact angle on liquid convective heat transfer in microchannels," *Heat and Mass Transfer*, vol. 49, no. 21-22, pp. 4161–4170, 2006.

[11] M. Aevizeh, A. Darvizehv, and H. Rajabi, "Free vibration analysis of dragonfly wings using finite element method," *The International Journal of Multiphysics*, vol. 3, no. 1, pp. 101–110, 2009.

[12] A. Khila, E. Abouheif, and L. Rowe, "Evolution of a novel appendage ground plan in water striders is driven by changes in the hox gene Ultrabithorax," *PLoS Genetics*, vol. 5, no. 7, article e1000583, 2009.

[13] P. H. Li, L. J. Yang, and Q. F. Fu, "Effect of surface contact angle on the wall impingement of a power-law liquid jet," *Physics of Fluids*, vol. 33, no. 4, article 043105, 2021.

[14] A. A. Ibrahim and M. A. Jog, "Nonlinear instability of an annular liquid sheet exposed to gas flow," *International Journal of Multiphase Flow*, vol. 34, no. 7, pp. 647–664, 2008.

[15] L. H. Liu, Q. F. Fu, and L. J. Yang, "Linear stability analysis of liquid jet exposed to subsonic crossflow with heat and mass transfer," *Physics of Fluids*, vol. 33, no. 3, article 034111, 2021.

[16] Q. F. Fu, F. Ge, W. D. Wang, and L. J. Yang, "Spray characteristics of gel propellants in an open-end swirl injector," *Fuel*, vol. 254, article 115555, 2019.

[17] K. Y. Law, "Definitions for hydrophilicity, hydrophobicity, and superhydrophobicity: getting the basics right," *Journal of Physical Chemistry Letters*, vol. 5, no. 4, pp. 686–688, 2014.

[18] C. J. Choi and H. K. Cho, "Investigation on emergency core coolant bypass with local measurement of liquid film thickness using electrical conductance sensor fabricated on flexible printed circuit board," *International Journal of Heat and Mass Transfer*, vol. 139, pp. 130–143, 2019.

[19] Q. F. Fu, L. J. Yang, Y. Y. Qu, and B. Gu, "Geometrical effects on the fluid dynamics of an open-end swirl injector," *Journal Propulsion and Power*, vol. 27, no. 5, pp. 929–936, 2011.

[20] Q. F. Fu, Y. X. Zhang, C. J. Mo, and L. J. Yang, "Molecular dynamics study on the mechanism of nanoscale jet instability reaching supercritical conditions," *Applied Sciences*, vol. 8, no. 10, p. 1714, 2018.

[21] Q. F. Fu, Z. X. Fang, Y. X. Zhang, and L. J. Yang, "Molecular dynamics simulation of a jet in a binary system at supercritical environment," *Molecules*, vol. 24, p. 31, 2019.

[22] A. Lozano, F. Barreras, G. Hauke, and C. Dopazo, "Longitudinal instabilities in an air-blasted liquid sheet," *Journal of Fluid Mechanics*, vol. 437, pp. 143–173, 2001.

[23] E. A. Ibrahim, "Instability of a liquid sheet of parabolic velocity profile," *Physics of Fluids*, vol. 10, no. 4, pp. 1034–1036, 1998.

Hindawi
International Journal of Aerospace Engineering
Volume 2022, Article ID 4633333, 15 pages
https://doi.org/10.1155/2022/4633333

Research Article

Effects of Flow Coefficient on Turbine Aerodynamic Performance and Loss Characteristics

Shaoyun Yang, Wei Du, Lei Luo, and Songtao Wang

School of Energy Science and Engineering, Harbin Institute of Technology, Harbin, China

Correspondence should be addressed to Wei Du; hitdw9211@outlook.com

Received 7 July 2022; Accepted 5 September 2022; Published 16 September 2022

Academic Editor: Hao Chen

The effects of flow coefficient on the gas flow and loss characteristics inside the high-pressure turbine is investigated using a numerical simulation. In this paper, the midspan of the first stator of the "Lisa" 1.5 stage high-pressure turbine is used as a prototype to obtain different flow coefficients by changing the stagger angle and the exit angle. The boundary conditions of all cases are consistent with the experimental data of "Lisa". The results show that the flow coefficient is decreased from 0.478 to 0.374 as the stagger angle is varied from 44.2° to 56.2° and from 0.630 to 0.341 as the exit angle is varied from 63° to 75°. Large stagger angle or large exit angle both cause an increase in turbine aerodynamic losses. The similarity between the two is that both cause enhanced effect of transverse secondary flow in the passage. The difference is that with large stagger angle, the adverse pressure gradient affects a large area, resulting in large boundary layer losses; with large exit angle, the passage vortex is weakened but with a large influence area.

1. Introduction

Improving the thrust-to-weight ratio of engines has been a long-standing goal of researchers [1, 2]. On the one hand, the turbine inlet temperature can be increased to increase the thrust, and the turbine inlet temperature has now reached over 1800 K, which requires reliable high temperature resistant materials and effective cooling techniques [3–9]. On the other hand, the turbine load can be increased to reduce the number of blades to reduce the turbine weight [10, 11], but this brings problems related to blade strength. When both methods are difficult to achieve, increasing the flow rate can be used to increase the engine thrust, which means that the turbine has a high flow coefficient. Therefore, it is necessary to study the aerodynamic characteristics and loss distribution inside the turbine for different flow coefficients.

In the early studies, flow coefficient φ and loading coefficient ψ were considered as key design parameters. Smith experimentally established a simple correlation equation between turbine efficiency and flow coefficient and loading coefficient [12]. As the flow coefficient was increased, the turbine efficiency showed a tendency to be increased and then decreased. The efficiency was improved because the development of boundary layer and secondary flow was limited by the high velocity airflow. However, when airflow velocity exceeded a certain range, large dynamic pressure caused a decrease in efficiency.

The Smith chart provided a simple reference for turbine design. To ensure the rationality of the turbine design results, the researchers proposed a large number of loss models. Some of the famous models include Aineley and Mathieson [13], Craig and Cox [14], Kacker and Okapuu [15], etc. Coull et al. compared the completeness of each model's reproduction of the Smith chart and assessed the accuracy of the loss correlations [16]. The results showed that the profile loss model of Coull and Hodson, and the secondary loss model of Craig and Cox predict reasonable results. Coull et al. found higher profile loss at high stage loading coefficient and low flow coefficient, and higher secondary loss at high flow coefficient and low stage loading coefficient. At high flow coefficients, the profile loss showed a weak increasing trend due to increasing Reynolds number, and the secondary loss showed a significant increasing trend

due to higher outlet dynamic pressure. To investigate the influence of the selection of key parameters on the turbine aerodynamic design, researchers have conducted many studies based on the Smith chart through mean line analysis and experiments. Ivan et al. [17] found that the flow coefficient is one of the most critical design parameters affecting the turbine aerodynamic efficiency by mean-line multidimensional optimization. Vázquez et al. compared the advantages and disadvantages of high through-flow design(HTF) and low through-flow design(LTF) in loading low pressure turbines and refined the Smith chart based on the flow characteristics [18]. Vázquez concluded that HTF was similar to conventional blades, resulting in a large exit Mach number. The HTF reduced the blade length, while keeping the flow rate constant, to reduce engine weight and engine size.

Although the Smith chart gives the effects of flow coefficient on turbine efficiency, there is a lack of detailed description of the effects of flow coefficients on the high-pressure turbine flow field. Secondary flow losses are one of the main factors to affect the high-pressure turbine aerodynamic performance. Wang et al. visualized the generation and development of vortex structures such as passage vortices, horseshoe vortices, and shedding vortices by smoke tracing technique [19]. Qu et al. compared the differences of secondary flow structures in the passage of front-loaded and aft-loaded blades [20]. It was found that the transverse secondary flow in the front-loaded blade was stronger without the wake; the development of secondary flow was inhibited with the wake. Qu also discussed the interaction between wake and endwall secondary flow. They found that the wake reduced the end-wall secondary flow losses at higher Reynolds number [21]. Winhart et al. analyzed the complex interactions between the wake, the secondary flow structure and the boundary layer flow to determine the contribution of the secondary flow components to the turbulent kinetic energy [22, 23]. Darji studied the generation location of horseshoe vortices and the development pattern of endwall flow under different working conditions [24]. Tsujita found that the increase in exit Mach number reduced the transverse secondary flow on the endwall, causing weaker passage vortices [25]. Profile losses are also one of main reasons for turbine aerodynamic performance reduction. Simoni et al. studied the effects of wake on profile loss and found that the well-mixed wake caused low profile loss [26]. Kodama et al. proposed a method to estimate profile loss and demonstrated the accuracy of the method by RANS [27]. However, few studies have covered the effect of the flow coefficient on the loss distribution. In order to explain the reason for the decrease in efficiency at high or low flow coefficients, it is necessary to study the effect of flow coefficient on flow structure and loss distribution.

According to the existing literature, the flow coefficient is an important influencing parameter for turbine aerodynamic performance. Although the effect of flow coefficient on efficiency has been studied experimentally and by mean line analysis, there are few studies on the causes of efficiency decrease due to flow coefficient variation. It is necessary to study the effect of flow coefficient on high-pressure turbine secondary flow loss and lobe loss. Therefore, this paper hopes to compare the aerodynamic performance of high-pressure turbine with different flow coefficients by CFD simulation. The effect of the flow coefficient on the flow characteristics within the high-pressure turbine is investigated. Explain the reasons of efficiency decrease by analyzing the magnitude and distribution of losses.

Table 1: Profile geometry parameters.

Parameter	Value
Profile inlet angle	0.0°
Profile exit angle, β	72.0°
Stagger angle, α	50.2°
Axial chord	49.71 mm
Pitch	63.70 mm
Height	70 mm
LE radius	7.00 mm
TE thickness	1.30 mm

Table 2: Studies cases.

Parameter	Baseline	Variation range
Stagger angle, α	50.2°	44.2° to 56.2°
Exit angle, β	72°	63° to 75°

2. General Description of Physical Models

In this study, the differences in loss characteristics and flow structure in a high-pressure turbine guide vane with different flow coefficients are numerically investigated. Considering that the axial velocity at the exit of the turbine is the determining factor of the flow coefficient [28], it is necessary to study the geometrical parameters of the cascade that have an influence on the axial velocity. On the one hand, the stagger angle affects the passage shape, and on the other hand, the exit angle affects the flow rate. Therefore, the flow coefficient is varied by changing the stagger angle or the exit angle. A single row cascade model is used in the study. The model is based on the midspan of the first stator of the "Lisa" 1.5 stage high-pressure turbine. Table 1 shows the geometric parameters. The software Autoblade is used to change the stagger angle and the exit angle while other parameters, such as the axial chord, remain unchanged. Table 2 Shows the cases. Figure 1. shows the parameters definition and the cascade geometry of some cases.

3. Computational Details

3.1. Overview. The commercial software ANSYS CFX, which uses the element-based finite volume, is used to predict the flow structure in the cascade passage. The Shear Stress Transport $\gamma - \theta$ turbulence model is used to solve the three-dimensional constant turbulence flow. The grid is generated using Autogrid5. The boundary condition parameters are obtained from Behr [29].

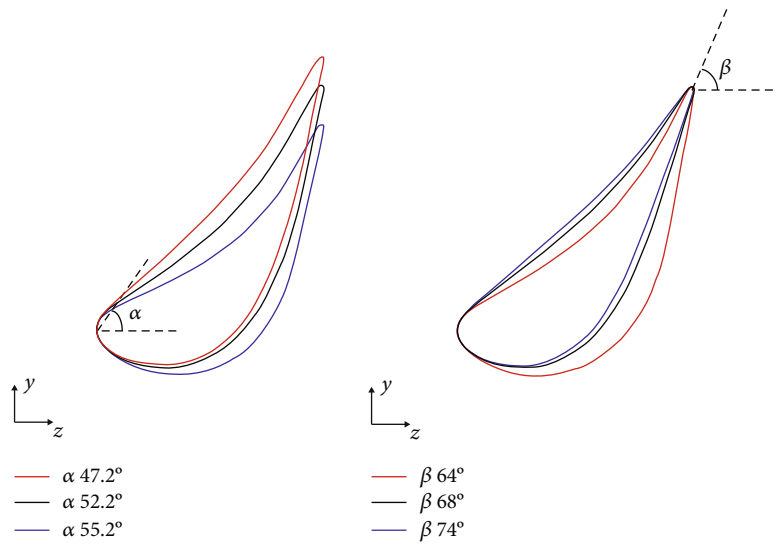

Figure 1: Parameters definition.

3.2. Control Equations. In this paper, the RANS model is used for the steady simulation, whose control equations are shown below.

$$\frac{\partial \rho}{\partial t} + \frac{\partial}{\partial x_j}\left(\rho \bar{u}_j\right) = 0 \tag{1}$$

$$\frac{\partial}{\partial t}\left(\rho \bar{u}_i\right) + \frac{\partial}{\partial x_j}\left(\rho \bar{u}_i \bar{u}_j\right) = -\frac{\partial p}{\partial x_i} + \frac{\partial}{\partial x_j}\left[\mu\left(\frac{\partial \bar{u}_j}{\partial x_i} + \frac{\partial \bar{u}_i}{\partial x_j}\right) - \rho\overline{u_i' u_j'}\right] - \frac{2}{3}\frac{\partial}{\partial x_j}\left(\mu\frac{\partial \bar{u}_j}{\partial x_i}\right) \tag{2}$$

$$\frac{\partial}{\partial t}\left(\rho c_p \bar{T}\right) + \frac{\partial}{\partial x_j}\left(\rho c_p \bar{u}_j \bar{T}\right) = \frac{\partial}{\partial x_j}\left[\frac{\mu}{\mathrm{Pr}}\frac{\partial}{\partial x_j}\left(c_p \bar{T}\right) - \rho c_p \overline{x_j' T'}\right] + S_E \tag{3}$$

3.3. Parameter Definitions. The flow coefficient is defined as [29]:

$$\varphi = \frac{\mathrm{c_x}}{\mathrm{u}} \tag{4}$$

where here c_x is the axial velocity of the airflow at the outlet of the guide vane, u is the blade velocity at midspan.

The aerodynamic performance of turbine blade is commonly measured by the total pressure loss coefficient. The total pressure loss coefficient is defined as:

$$\mathrm{Y} = \frac{\mathrm{p_{t,in}} - \mathrm{p_{t,out}}}{\mathrm{p_{t,out}} - \mathrm{p_{s,out}}} \tag{5}$$

Where here $p_{t,\mathrm{in}}$ is the inlet total pressure, $p_{t,\mathrm{out}}$ is the outlet total pressure, $p_{s,\mathrm{out}}$ is the outlet static pressure.

C_p is a commonly used result of the dimensionless treatment of static/total pressure, which is defined by

$$\mathrm{C_p} = \frac{\mathrm{p} - \mathrm{p_{s,out}}}{\mathrm{p_{t,inlet}} - \mathrm{p_{s,out}}} \tag{6}$$

In the case of the total pressure coefficient C_{pt}, the pressure is taken as the measured value of the total pressure, and in the case of C_{ps}, the pressure is taken as the static pressure.

The dissipation function ϕ characterizes the irreversible loss of mechanical energy during fluid flow and is defined by the following equation [30]:

$$\frac{\phi}{\mu} = 2\left[\left(\frac{\partial u}{\partial x}\right)^2 + \left(\frac{\partial v}{\partial y}\right)^2 + \left(\frac{\partial w}{\partial z}\right)^2 + \left(\frac{\partial v}{\partial x} + \frac{\partial u}{\partial y}\right)^2 + \left(\frac{\partial w}{\partial y} + \frac{\partial v}{\partial z}\right)^2 + \left(\frac{\partial u}{\partial z} + \frac{\partial w}{\partial x}\right)^2\right] - \frac{2}{3}\left(\frac{\partial u}{\partial x} + \frac{\partial v}{\partial y} + \frac{\partial w}{\partial z}\right)^2 \tag{7}$$

Where here μ is the dynamic viscosity.

The boundary layer momentum thickness θ is defined as the thickness of the mainstream corresponding to momentum loss of the boundary layer, which approximates the loss caused by the boundary layer, and the definition equation is shown below.

$$\theta = \int_0^{\delta} \frac{\rho \mathrm{u}}{\rho_e \mathrm{u_e}}\left(1 - \frac{u}{u_e}\right) dy \tag{8}$$

Where here δ is the thickness of the boundary layer, ρ is the local density of the boundary layer, u is the local tangential velocity in the boundary layer, ρ_e is the mainstream density, u_e is the mainstream velocity.

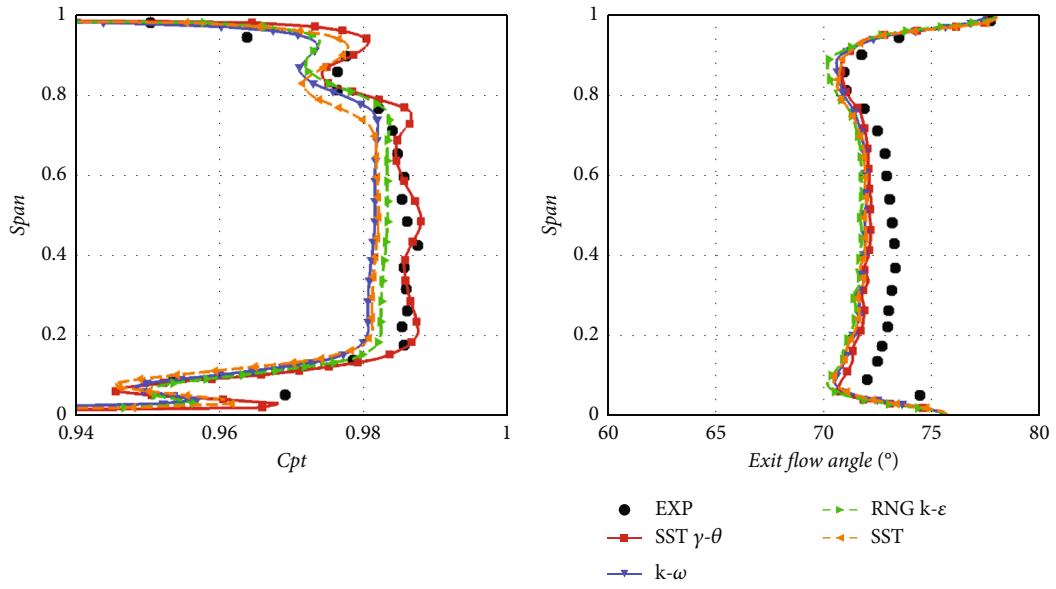

(a) Total pressure coefficient (b) Exit Flow Angle

Figure 2: Comparison between the numerical results and experimental results.

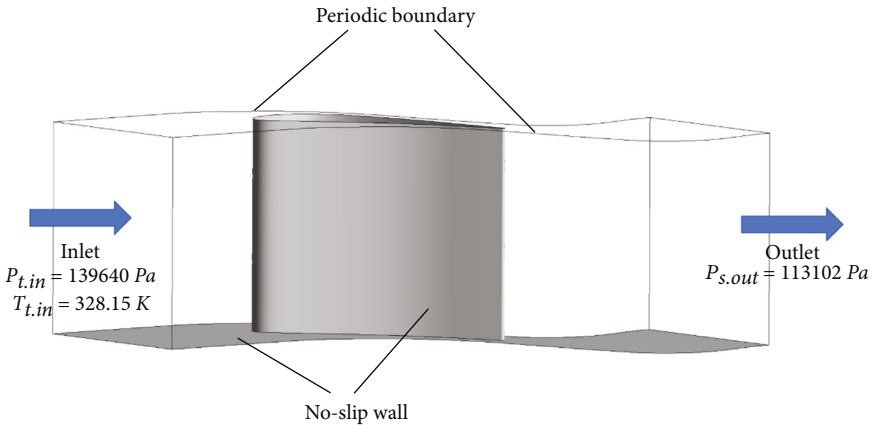

Figure 3: Computational domain and boundary conditions.

3.4. Turbulent Model Selection. The experimental results from the Behr [29] are compared with the numerical results, which is obtained by four different turbulence models, as shown in Figure 2. The boundary conditions of the four cases, such as the total inlet pressure, the total inlet temperature and the static outlet pressure, are consistent with the experimental boundary conditions given in the reference [29]. Figure 2(a) shows that the trends of the total pressure coefficient along the blade predicted by these four turbulence models are similar to the experimental results. The shear-stress-transport (SST), $k-\omega$ and RNG $k-\varepsilon$ turbulence under-predict the total pressure coefficient. The predicted value of SST $\gamma-\theta$ turbulence model is more accurate compared to the other models. Figure 2(b) shows that all models under-predict the exit airflow angle compared to the experimental results, but the trends of the predicted results are consistent with the experimental ones. And it is found that the exit airflow angle predicted by SST $\gamma-\theta$ turbulence

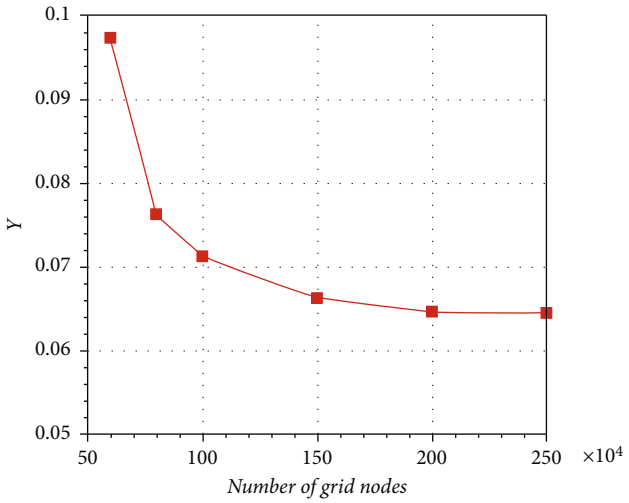

Figure 4: Mesh independence.

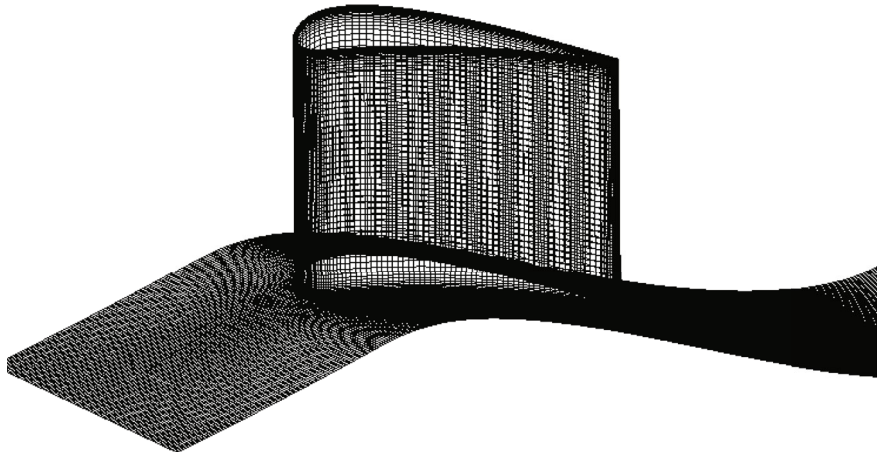

Figure 5: Detail of mesh.

model is closet to the experimental value. By comparing the accuracy of the predicted total pressure coefficient and exit airflow angle, SST $\gamma - \theta$ is found to be the best choice for predicting the aerodynamic performance of the studied blades. Therefore, the SST $\gamma - \theta$ is used to predict the flow state and loss variation in the turbine passage at different flow coefficients in this study.

3.5. Boundary Conditions. Considering the low velocity and pressure in the calculation, ideal gas with constant specific heat capacity and viscosity is used in this study. The boundary conditions for the numerical calculations are obtained from Behr [29]. The total inlet temperature is 328.15 K, the total inlet pressure is 139640 Pa and the static outlet pressure is 113102 Pa. As shown in Figure 3, no-slip boundary conditions are used for the endwall and blade wall. Periodic boundary conditions are used.

3.6. Grid Details and Independent Solutions. In this study, the structured meshes are generated by Autogrid5. This is an automatic turbomachine mesh generation program provided by Numeca. The grid adopts O4H topology. The main flow passage grid adopts H-type topology and the grid around the blade adopts O-type topology. The y plus on the end wall is about 1 to capture the detailed flow structure. To ensure the accuracy of the calculation results while also minimizing the calculation time, the grid independence is carefully evaluated and the results are shown in Figure 4. The results show that the total pressure loss remains almost constant when the number of grids exceeds 2 million. Therefore, the grid number is chosen to be 2 million for all cases. The grid details are shown in Figure 5.

4. Results and Discussion

4.1. Stagger Angle Effects. Figure 6 shows the effects of the stagger angle variation on turbine flow coefficient and total pressure loss coefficient. The results show that the flow coefficient exhibits a downward trend from 0.478 to 0.374 as the stagger angle is increased from 44.2° to 56.2°. This indicates that the stagger angle has important effects on the flow coefficient. It is also seen that the total pressure loss coefficient is increased with increased stagger angle, from 0.033 to 0.059. According to the previous experience, high flow coefficient causes high profile loss, which deteriorates the turbine efficiency. However, the results in Figure 6 show that low flow coefficient also leads to high total pressure loss.

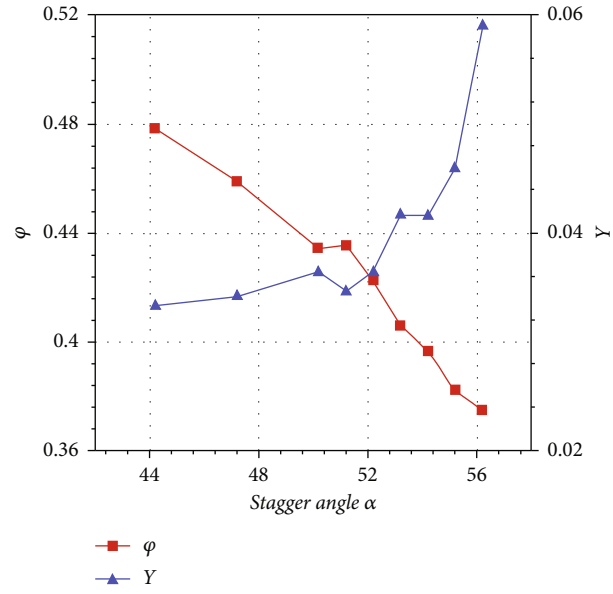

Figure 6: Flow coefficient and total pressure loss coefficient for different stagger angles.

Figure 7 shows the comparison of the static pressure coefficients distribution near the mid-span of the turbine cascades with different stagger angles. As the stagger angle is changed rom 47.2° to 52.2°, the lowest static pressure point moves downstream and the lowest pressure value increases, indicating a decrease in the adverse pressure gradient. This leads to a weak transverse. Then, the lowest static pressure point moves toward the middle and the lowest pressure value gradually decreases as the stagger angle is changed

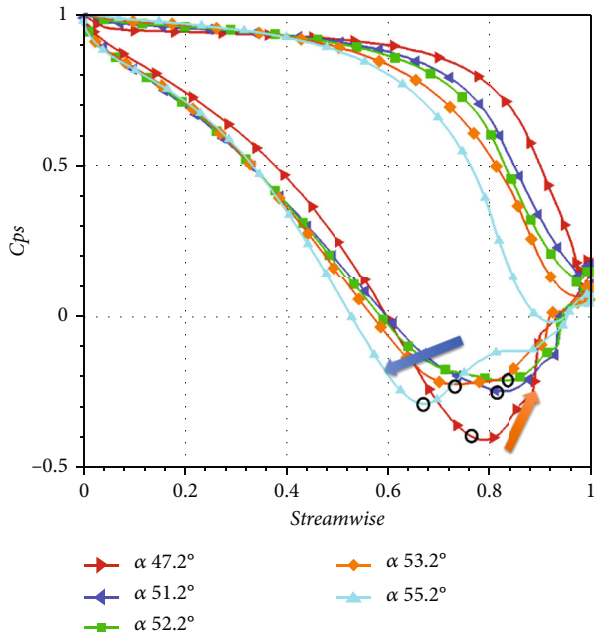

Figure 7: Comparison of static pressure coefficient near the midspan of the blade for different stagger angles.

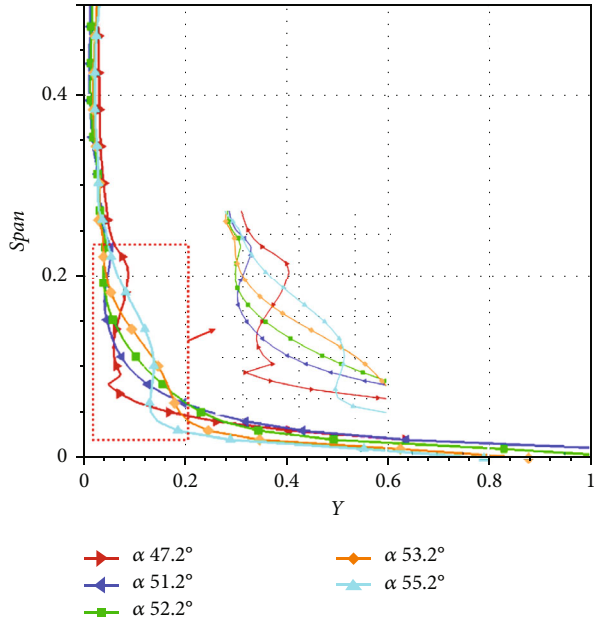

Figure 8: Comparison of total pressure loss coefficient for different stagger angles.

from 52.2° to 55.2°.It shows that the influence range of transverse secondary flow increases. The distribution position of the load does not move backward all the time with the increase of the stagger angle, but moves downstream to a certain position first and then moves to the middle. In addition, the blade load is reduced as the stagger angle is increased.

Figure 8 shows the comparison of the total pressure loss coefficient distribution at the outlet along the span with different stagger angles. The total pressure loss remains constant from 30% to 50% span, then changes due to the passage vortex and endwall secondary flow within the 30% span from the endwall. The loss peak and the influence area of the passage vortex are reduced as the stagger angle is increased from 47.2° to 55.2°. Also, the loss area of the passage vortex moves upward along the span. In contrast, the loss area due to endwall secondary flow is increased as the stagger angle is increased. When the stagger angle is 55.2°, only the influence of the endwall secondary flow is seen. The results show that the increase in the stagger angle

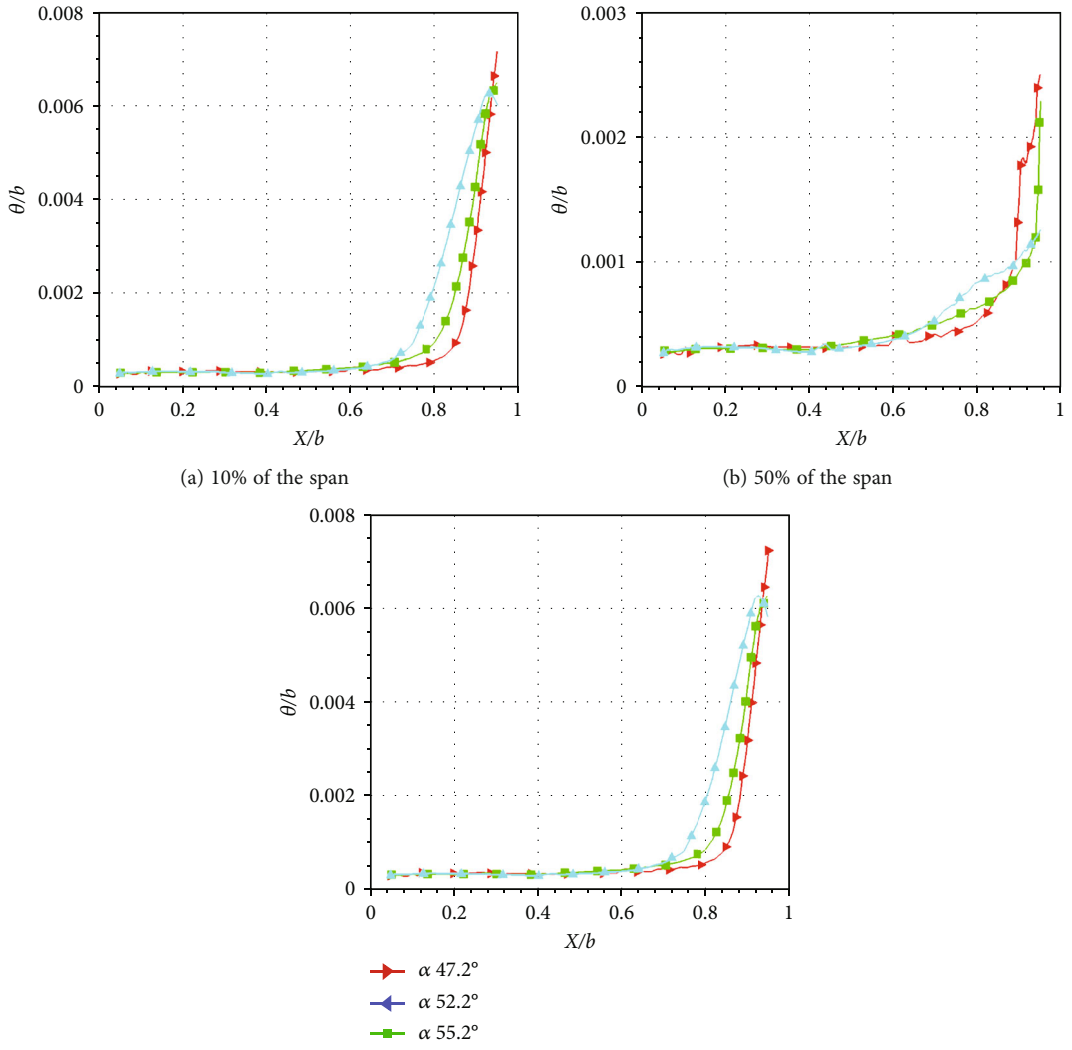

(a) 10% of the span

(b) 50% of the span

(c) 90% of the span

Figure 9: Comparison of boundary layer momentum thickness for different stagger angles.

weakens the passage vortex and enhances the endwall secondary flow.

Figure 6 has shown that the increase in the stagger angle would cause a decrease in the turbine flow coefficient and an increase in the total pressure loss. In order to further analyze the effects of stagger angle variation on the aerodynamic performance of the turbine and the distribution of turbine loss at different flow coefficients, α47.2°, α52.2° and α55.2° are selected to compare the differences in boundary layer momentum thickness, dissipation function, end wall flow lines and total pressure loss at the outlet.

The momentum thickness approximates the loss of boundary layer [31, 32]. Figure 9 compares the boundary layer momentum thickness at different spans for α47.2°, α52.2° and α55.2°. As shown in Figure 9(a), there is no significant change in the boundary layer momentum thickness until 0.6b at 10% span. At 0.6b, the momentum loss of α55.2° is increased under the effect of the adverse pressure gradient, leading to a significant increase in the momentum thickness. α52.2° at 0.75b, α47.2° at 0.8b. In the range from 0.6b to 0.9b, the momentum thickness of α55.2° is the largest among the three cases, indicating that its boundary layer loss is the largest. After 0.9b, the momentum thickness of α47.2° is the largest, indicating that the boundary layer loss near the trailing edge is decreased with increased stagger angle. According to Figure 9(b), the locations where the momentum thickness starts to change significantly are α47.2° at 0.78b α52.2° at 0.8b and α55.2° at 0.65b, which are consistent with the locations of the adverse pressure gradient shown in Figure 7. Figure 9(c) shows similar results to Figure 9(a). The increase in the stagger angle enhances the boundary layer loss in the middle and rear of the cascade and weakens the boundary layer loss near the trailing edge.

The dissipation function is often used to measure the loss of mechanical energy [30]. Figure 10 shows the dissipation function from 0.2b to 0.95b cross sections at α47.2°, α 52.2° and α55.2°. The profile losses near the surface of the

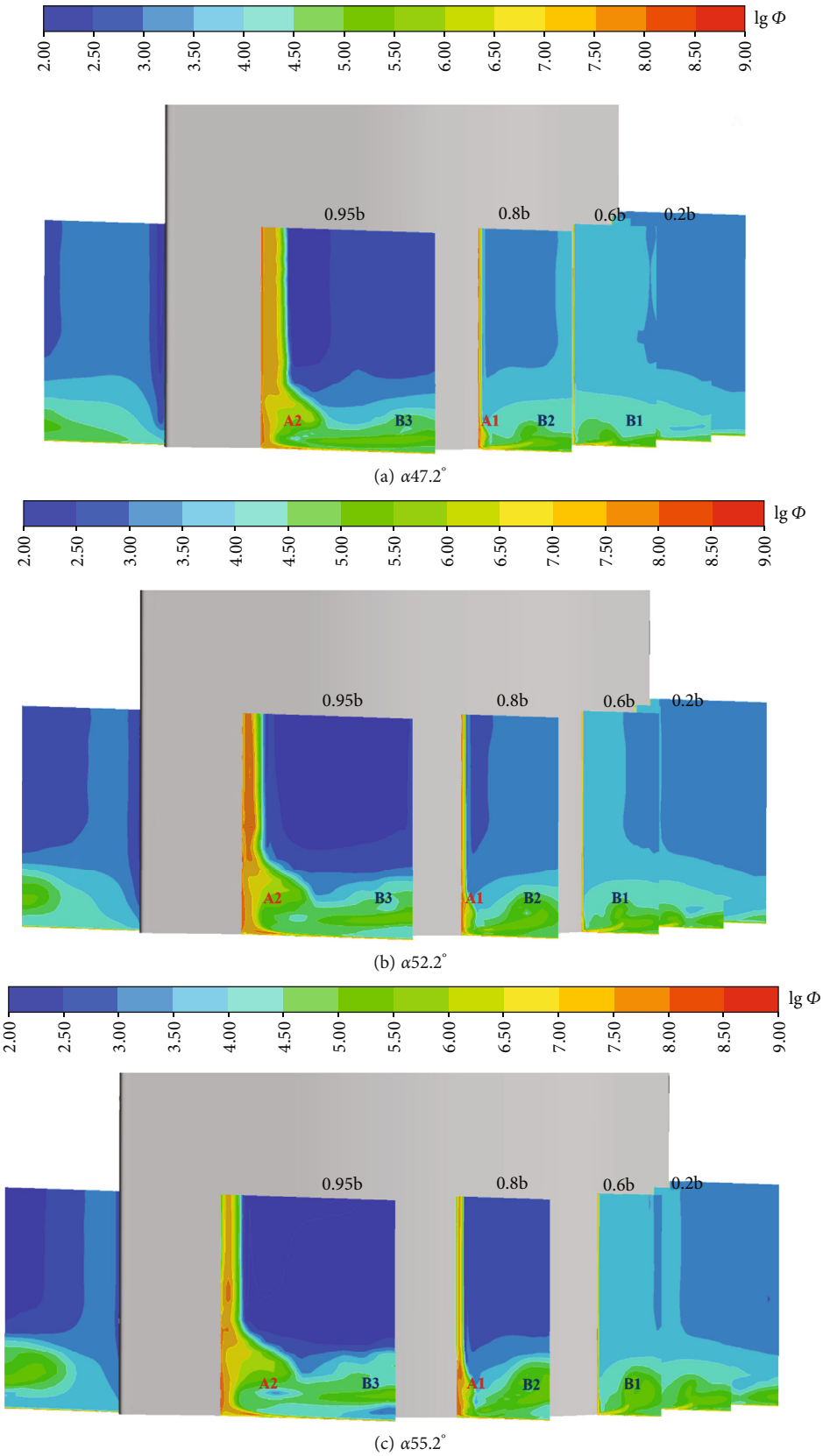

Figure 10: Comparison of dissipation functions for different stagger angles.

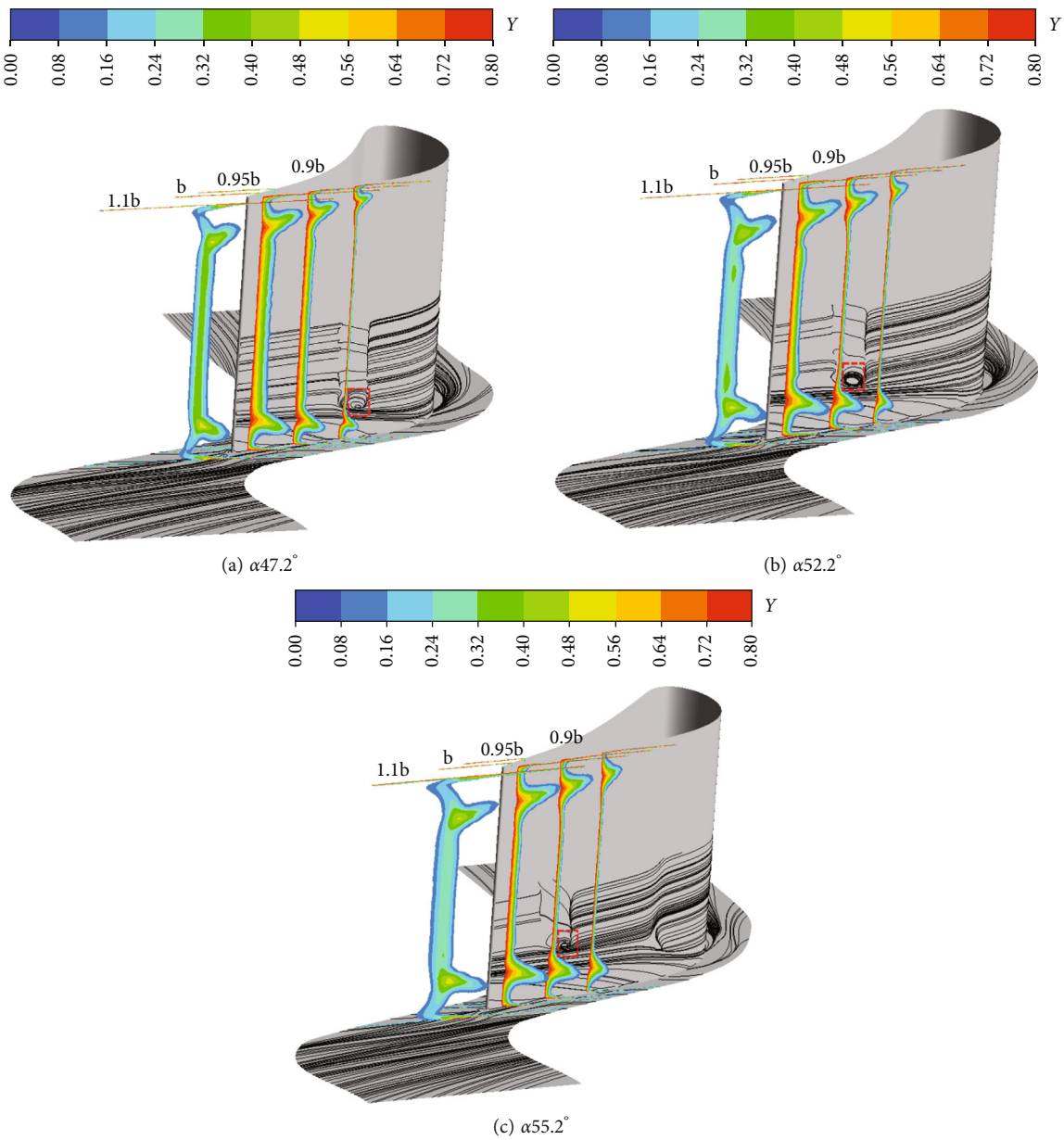

Figure 11: Comparison of total pressure loss and endwall streamline for different stagger angles.

blade body, the losses caused by the passage vortex near the end wall, and the losses caused by the transverse secondary flow in the middle of the passage can be found. The values and distribution characteristics of the dissipation functions vary with the stagger angle. First, the dissipation coefficient near the blade is decreased as the stagger angle is increased at 0.95b, indicating that the profile loss near the trailing edge is decreased. This is consistent with the results of the boundary layer momentum thickness variation shown in Figure 9. The high loss areas of passage vortex and endwall secondary flow loss are indicated by A1 and A2, and the high loss areas of transverse secondary flow are indicated by B1, B2 and B3. Compared with $\alpha 47.2^{\circ}$ and $\alpha 52.2^{\circ}$, $\alpha 55.2^{\circ}$ has relatively larger values of the dissipation function at A1 and A2, indicating that the increase of the stagger angle enhances the losses caused by the passage vortex. Similarly, the dissipation functions at B1, B2, and B3 indicate that increasing the stagger angle also enhances the effect of transverse secondary flow. The high loss region caused by the transverse secondary flow is increased and moved up toward the center of the passage.

Figure 11 shows the total pressure loss coefficient from 0.9b to 1.1b cross sections and the endwall streamline for different stagger angles. The results show that the influence area of passage vortex is reduced with increased stagger angle. Considering that the cascade at $\alpha 47.2^{\circ}$ has a larger flow coefficient, the increase of axial velocity suppress the effect of passage vortices. The distribution of endwall streamline shows that flow separation occurs at the suction surface, whose location gradually moves

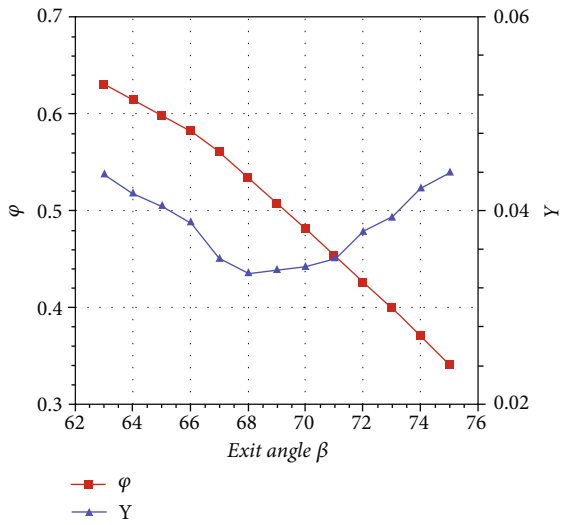

Figure 12: Flow coefficient and total pressure loss coefficient for different exit angles.

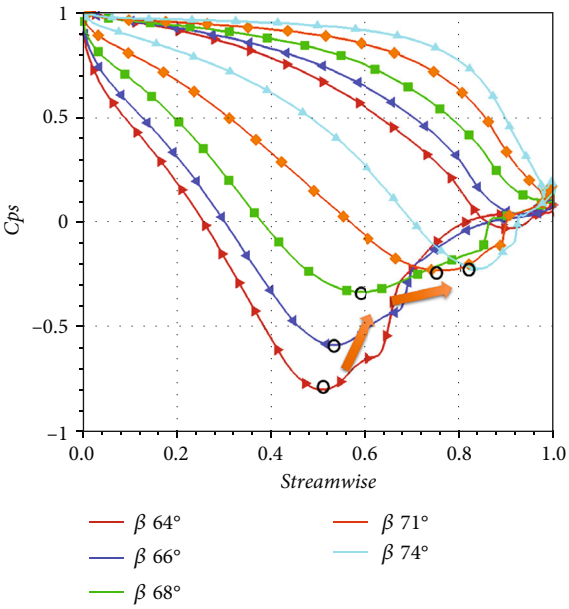

Figure 13: Comparison of static pressure coefficient near the midspan of the blade for different exit angles.

backward with increased stagger angle. This is consistent with the location of boundary layer separation shown in Figure 9(b). In addition, the radial migration of the fluid at the suction surface occurs at α55.2°. The appearance of radial pressure gradients indicates the accumulation of low-energy fluids at the end walls, which enhances secondary flow losses.

4.2. Exit Angle Effect. The axial velocity at the exit of the guide vane is the determining parameter of the flow coefficient, while the exit velocity is determined by the exit angle. In order to analyze the effect of flow coefficient variation on turbine efficiency more comprehensively, the aerodynamic performance of cascade with different exit angles is investigated. Figure 12 shows the variation of the flow coefficient and total pressure loss of the cascade with different exit angles. Comparing with Figure 6, it is found that the flow coefficient is more sensitive to the variation of the exit angle. The flow coefficient is decreased from 0.630 to 0.341 as the exit angle is increased from 63° to 75°. Also, different from the effect caused by the increased stagger angle, the total pressure loss coefficient is first decreased and then increased with the increased exit angle.

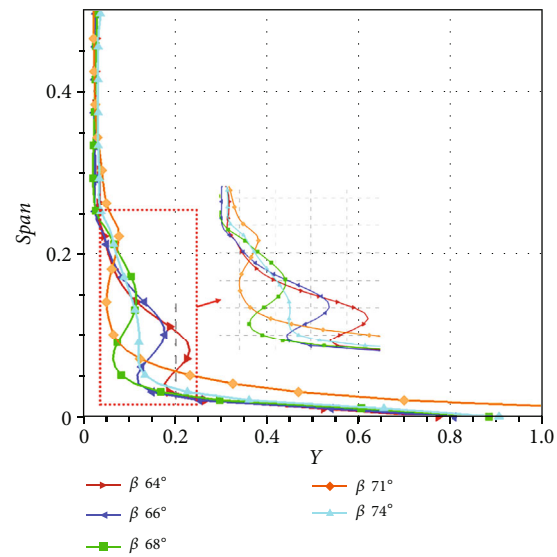

Figure 14: Comparison of total pressure loss coefficient for different exit angles.

Figure 13 shows the comparison of the static pressure coefficients distribution near the mid-span of the turbine cascades with different exit angles. The adverse pressure gradient is decreased and the position of the lowest pressure point at the suction moves from 0.5b to 0.85b as the exit angle is increased from 64° to 74°. When the exit angle is 64°, the suction surface is under the influence of a large adverse pressure gradient from the middle to the trailing edge. It shows that at large exit angle, there is not only strong transverse secondary flow in the passage but also large scale separation at the suction surface.

Figure 14 shows the comparison of the distribution of the total pressure loss coefficient at the outlet along the span for different exit angles. The effects of the change in exit angle on the passage vortex and the endwall secondary flow are different. The loss caused by the passage vortex is decreased with the increase of the exit angle, while the spreading influence area of the endwall secondary flow is increased. When the exit angle is 74°, there is no obvious peak loss of passage vortex, and the endwall secondary flow has a large effect within the 30% span from the endwall. At small exit angle, the loss of passage vortex is large; at large exit angle, the loss of end wall secondary flow is large; when the exit angle is at the suitable value, the effects of both are

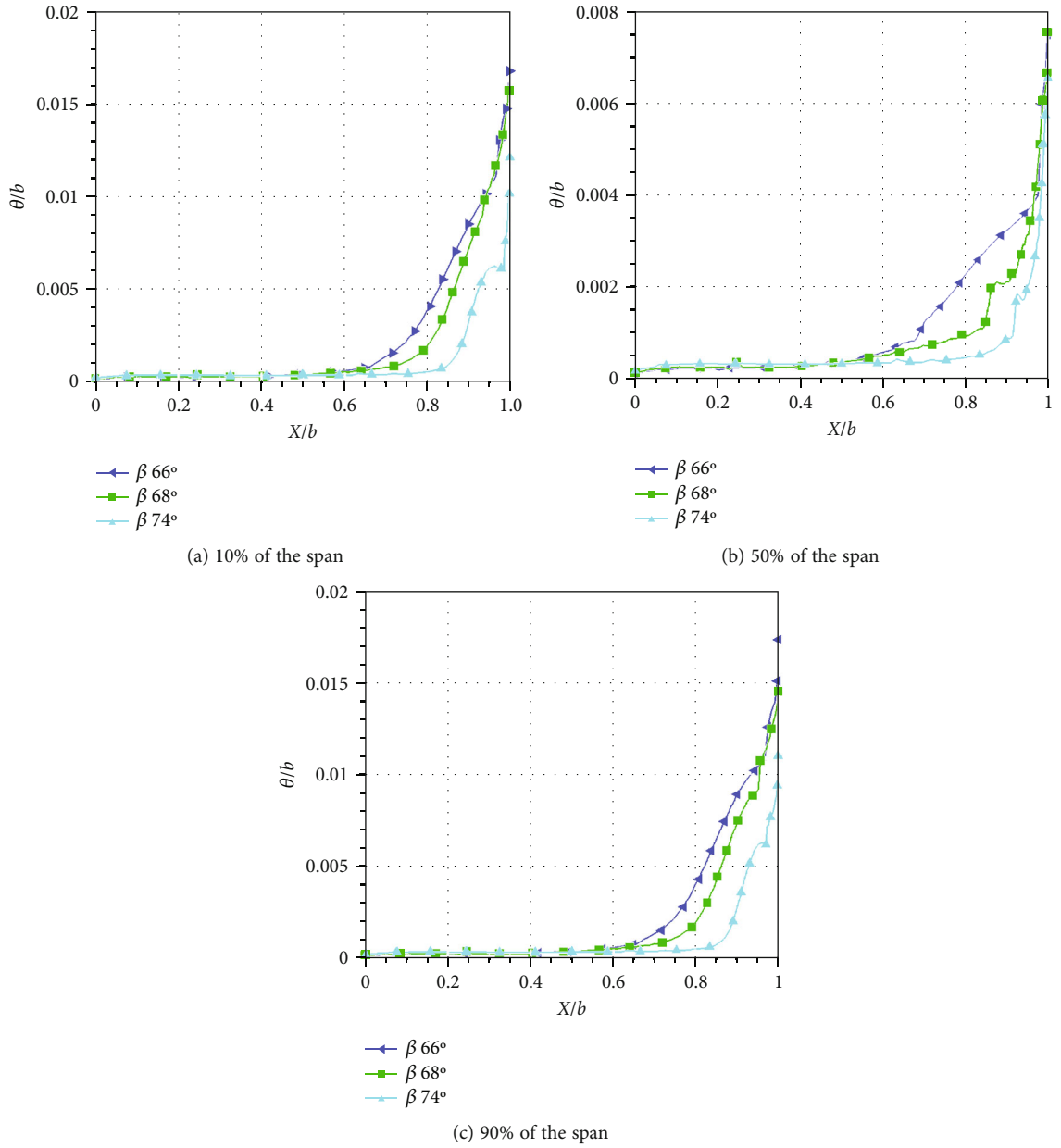

FIGURE 15: Comparison of boundary layer momentum thickness for different exit angles.

small. This corresponds to the variation of the total pressure loss in Figure 7.

Figure 15 compares the boundary layer momentum thickness at different spans for $\beta 66^\circ$, $\beta 68^\circ$ and $\beta 74^\circ$. As shown in Figure 15(a), there is no significant change in the momentum thickness until 0.6b at 10% span. The momentum thicknesses of $\beta 66^\circ$ and $\beta 68^\circ$ increase significantly due to the adverse pressure gradient at 0.6b, with $\beta 66^\circ$ having a faster growth rate. The momentum thickness of $\beta 74^\circ$ is increased at 0.85b. Therefore, the momentum thickness of $\beta 66^\circ$ is the largest among the three cases from 0.6b to 1b, indicating that it has the largest boundary layer loss. Figure 15(b) and Figure 15(c) show a similar pattern to Figure 15(a). Compared with Figure 13, it is found that the size and location of the adverse pressure gradient determine the boundary layer loss. The boundary layer loss is decreased as the exit angle is increased. Comparing the trend of boundary layer loss and secondary flow loss, and considering the trend of total pressure loss coefficient in Figure 12, it could be assumed that the secondary flow loss causes more influence.

Figure 16 shows the dissipation function from 0.2b to 0.95b cross sections at $\beta 66^\circ$, $\beta 68^\circ$ and $\beta 74^\circ$. A1, A2 indicate the high loss region of passage vortex and endwall secondary flow. B1, B2 and B3 indicate the high loss region of transverse secondary flow. By comparison, it is found that the passage vortex loss is decreased and the endwall secondary flow loss is increased with the increase of exit angle at A1. The loss region is reduced at A2. The variation of transverse secondary flow at B2 and B3 is

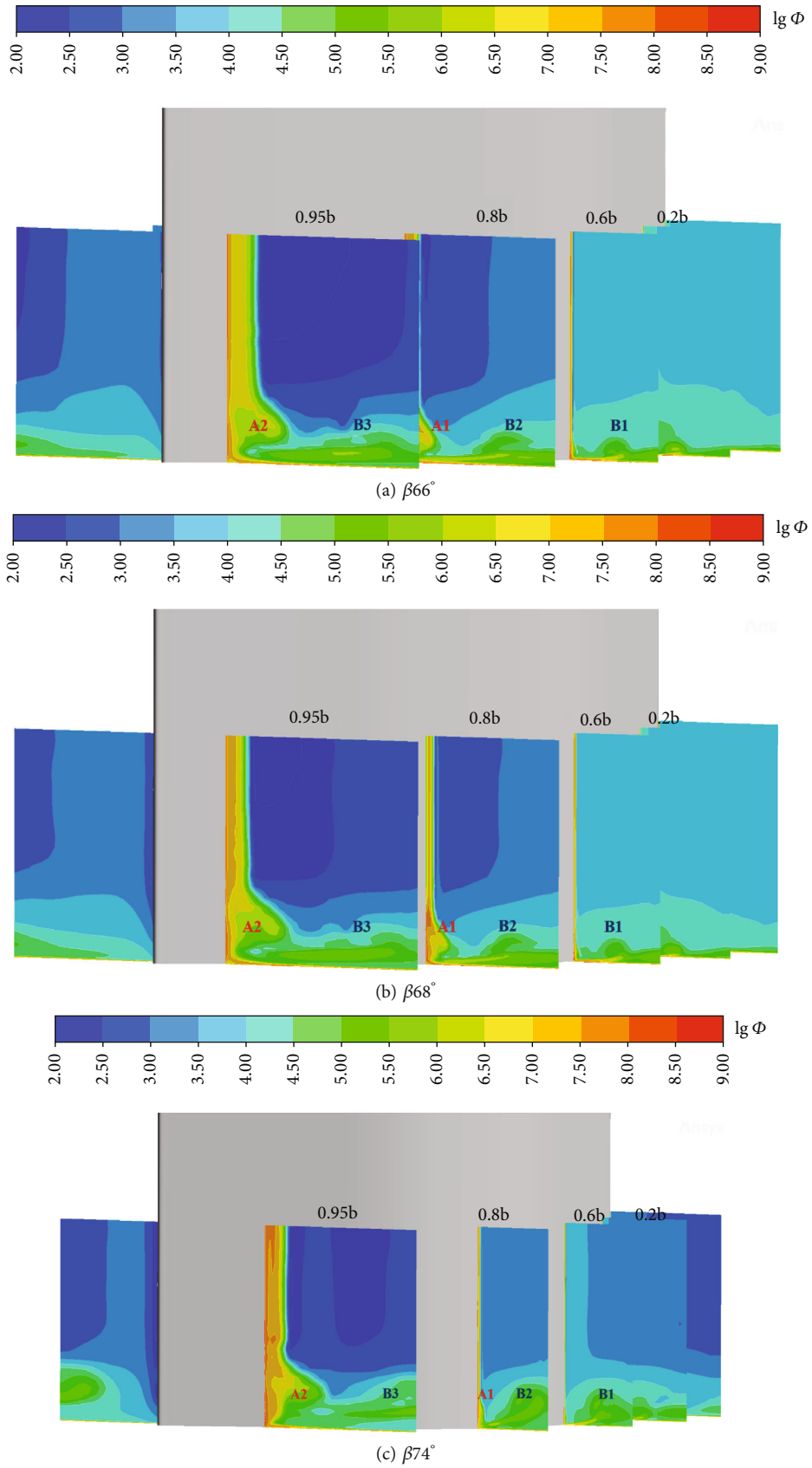

(a) $\beta 66^{\circ}$

(b) $\beta 68^{\circ}$

(c) $\beta 74^{\circ}$

Figure 16: Comparison of dissipation functions for different exit angles.

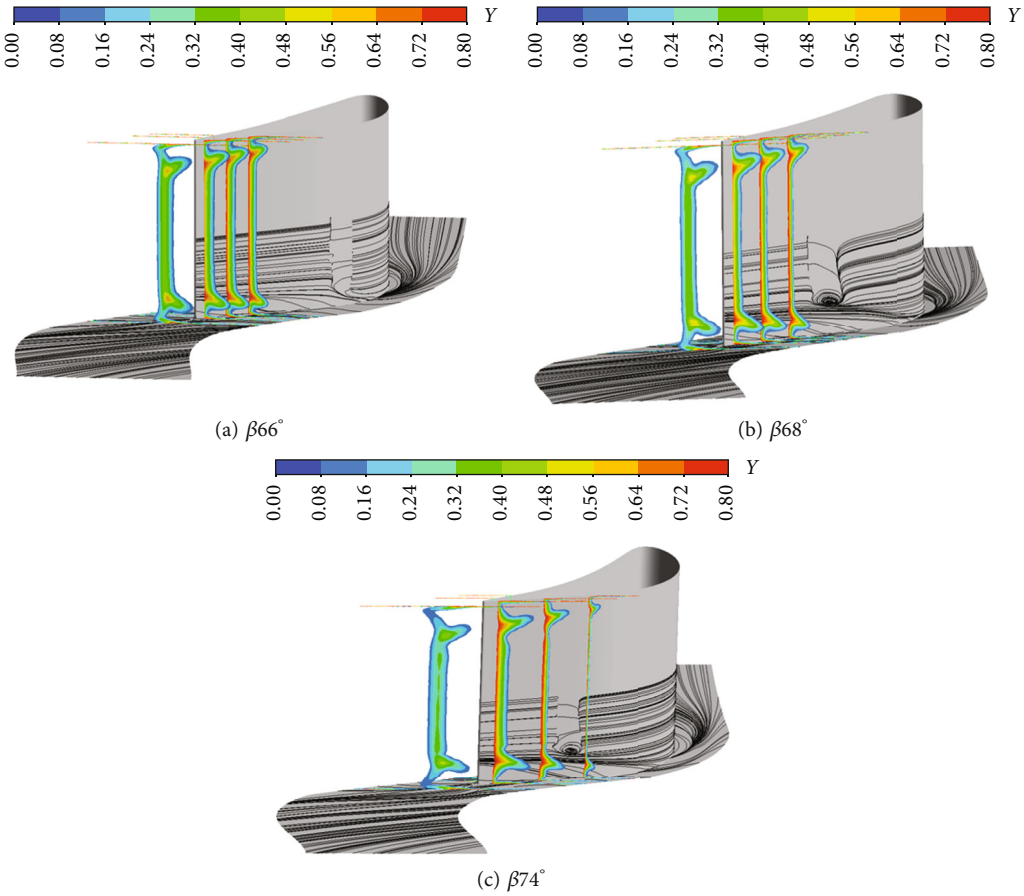

Figure 17: Comparison of total pressure loss and endwall streamline for different exit angles.

worth to note. $\beta 66^{\circ}$ has strong transverse secondary flow, with a small influence area near the endwall. $\beta 74^{\circ}$ has weak transverse secondary flow, with a large influence area away from the endwall. The resukts show that the increase of the exit angle weakens the transverse secondary flow and increases its influence area.

Figure 17 shows the total pressure loss coefficient from 0.9b to 1.1b cross sections and the endwall streamline for different exit angles. It is seen that the increase of the exit angle weakens the passage vortex and increases its influence area. The separation of the suction surface moves back with the increase of the exit angle. Compared with Figure 11, it is found that the common point is that the large flow coefficient limits the influence area of the passage vortex.

5. Conclusion

In this paper, the influence law of the variation of the stagger angle and exit angle of the cascade on the flow coefficient and loss coefficient is investigated by numerical simulant. The effects of flow coefficient on high-pressure turbine aerodynamic performance is analyzed. The main findings are as follows:

(1) The flow coefficient is influenced by the stagger angle and the exit angle. The flow coefficient is decreased from 0.478 to 0.374 as the stagger angle is changed from 44.2° to 56.2° and from 0.630 to 0.341 as the exit angle is changed from 63° to 75°. The flow coefficient is more sensitive to the exit angle

(2) The total pressure loss coefficient is decreased with the increase of the stagger angle. At large stagger angle, on the one hand, the adverse pressure gradient affects a large area, resulting in large boundary layer losses. On the other hand, the adverse pressure gradient is small, resulting in weak but large transverse secondary flow. In addition, the increase in stagger angle also enhances the influence of passage vortices and endwall secondary flow

(3) The total pressure loss coefficient is increased and then decreased with the increase of the exit angle. At large exit angle, the adverse pressure gradient is small with a small influence area, resulting in low boundary layer losses and weak but large transverse secondary flow. The strength of the passage vortex is decreased, while the influence area is increased

Nomenclature

α: Stagger angle (°)
B: Axial chord(m)
c_x: Axial velocity(m/s)

Y: Total pressure loss coefficient
$p_{t,\text{out}}$: Outlet total pressure (Pa)
C_p: Pressure coefficient
μ: Dynamic viscosity (Pa•s)
ρ: Density of air (kg•m^{-3})
$T_{t,\text{in}}$: Inlet total temperature (K)
β: Exit angle (°)
φ: Flow coefficient
u: Blade velocity at mid-span (m/s)
$p_{t,\text{in}}$: Inlet total pressure (Pa)
$p_{s,\text{out}}$: Outlet static pressure (Pa)
ϕ: Dissipation function
δ: Boundary layer thickness(m)
θ: Boundary layer momentum thickness (m)

Data Availability

The numerical data used to support the findings of this study are included within the article.

Conflicts of Interest

The author(s) declare(s) that they have no conflicts of interest.

Acknowledgments

The authors acknowledge the financial support provided by Natural Science Foundation of China (No.52106041, No. 52076053), Postdoctoral Special Assistant in Heilongjiang Province(LBH-TZ2109), China Postdoctoral Science Foundation funded project (2021 M690823), National Science and Technology Major Project (No. 2019-II-0010-0030), and Natural Science Fund for Excellent Young Scholars of Heilongjiang Province [No. YQ2021E023].

References

[1] D. Liu and R. Cheng, "Current status and development direction of aircraft power technology in the world," *Journal of Beijing University of Aeronautics and Astronautics*, vol. 28, no. 5, p. 490, 2002.

[2] W. Koop, "The integrated high performance turbine engine technology program," *International Society for Air Breathing Engines*, vol. 97, p. 7175, 1997.

[3] L. M. Wright and J. C. Han, "Enhanced internal cooling of turbine blades and vanes," *The Gas Turbine Handbook*, vol. 4, pp. 1–5, 2006.

[4] L. Meng, H. Li, G. Xie, Z. Tao, and Z. Zhou, "Film cooling performance on pressure side of turbine blade with different number of hole rows under rotating state," *Aerospace Science and Technology*, vol. 126, p. 107569, 2022.

[5] W. Du, L. Luo, Y. Jiao, S. Wang, X. Li, and B. Sunden, "Heat transfer in the trailing region of gas turbines - A state-of-the-art review," *Applied Thermal Engineering*, vol. 199, p. 117614, 2021.

[6] W. Du, L. Luo, S. Wang, and B. Sunden, "Film cooling in the trailing edge cutback with different land shapes and blowing ratios," *International Communications in Heat and Mass Transfer*, vol. 125, p. 105311, 2021.

[7] S. Lu, Q. Deng, P. M. Ligrani, H. Jiang, and Q. Zhang, "Effects of coolant and wall temperature variations on impingement jet array thermal performance," *Numerical Heat Transfer, Part A: Applications*, vol. 79, no. 1, pp. 68–82, 2021.

[8] W. Zhou, Q. Deng, W. He, J. He, and Z. Feng, "Conjugate heat transfer analysis for composite cooling structure using a decoupled method," *International Journal of Heat and Mass Transfer*, vol. 149, p. 119200, 2020.

[9] J. Liu, W. Du, S. Hussain, G. Xie, and B. Sundén, "Endwall film cooling holes design upstream of the leading edge of a turbine vane," *Numerical Heat Transfer, Part A: Applications*, vol. 79, no. 3, pp. 222–245, 2021.

[10] R. J. Howell, H. P. Hodson, V. Schulte et al., "Boundary layer development in the BR710 and BR715 LP turbines—the implementation of high-lift and ultra-high-lift concepts," *Journal of Turbomachinery*, vol. 124, no. 3, pp. 385–392, 2002.

[11] R. J. Howell, O. N. Ramesh, H. P. Hodson, N. W. Harvey, and V. Schulte, "High lift and aft-loaded profiles for low-pressure turbines," *Journal of Turbomachinery*, vol. 123, no. 2, pp. 181–188, 2001.

[12] S. F. Smith, "A simple correlation of turbine efficiency," *The Aeronautical Journal*, vol. 69, no. 655, pp. 467–470, 1965.

[13] D. G. Ainley and G. Mathieson, "Performance of Axial-Flow Turbines," *ARCHIVE Proceedings of the Institution of Mechanical Engineers, 1847-1982 (vols 1-196)*, vol. 159, no. 1, p. 230-24, 1948.

[14] H. Craig and H. Cox, "Performance estimation of axial flow turbines," *Proceedings of the Institution of Mechanical Engineers*, vol. 185, no. 1, pp. 407–424, 1970.

[15] S. C. Kacker and U. Okapuu, "A mean line prediction method for axial flow turbine efficiency," *Journal of Engineering for Power*, vol. 104, no. 1, pp. 111–119, 1982.

[16] J. D. Coull and H. P. Hodson, "Blade loading and its application in the mean-line design of low pressure turbines," *Journal of Turbomachinery*, vol. 135, no. 2, pp. 21–32, 2013.

[17] I. Zhdanov, S. Staudacher, and S. Falaleev, "An advanced usage of meanline loss systems for axial turbine design optimization," in *ASME Turbo Expo 2013: Turbine Technical Conference and Exposition*, San Antonio, Texas, USA, June 2013.

[18] R. Va' Squez, D. Cadrecha, and D. Torre, "High stage loading low pressure turbines: a new proposal for an efficiency chart," in *ASME Turbo Expo 2003, collocated with the 2003 International Joint Power Generation Conference*, Atlanta, Georgia, USA, June 2003.

[19] H. P. Wang, S. J. Olson, R. J. Goldstein, and E. R. G. Eckert, "Flow visualization in a linear turbine cascade of high performance turbine blades," *Journal of Turbomachinery*, vol. 119, no. 1, pp. 1–8, 1997.

[20] X. Qu, Y. Zhang, X. Lu, J. Zhu, and Y. Zhang, "Unsteady influences of blade loading distribution on secondary flow of ultra-high-lift LPT," *Aerospace Science and Technology*, vol. 96, p. 105550, 2020.

[21] X. Qu, Y. Zhang, X. Lu, G. Han, Z. Li, and J. Zhu, "Effects of periodic wakes on the endwall secondary flow in high-lift low-pressure turbine cascades at low Reynolds numbers," *Proceedings of the Institution of Mechanical Engineers, Part G: Journal of Aerospace Engineering*, vol. 233, no. 1, pp. 354–368, 2019.

[22] M. Sinkwitz, B. Winhart, D. Engelmann, F. di Mare, and R. Mailach, "On the periodically unsteady interaction of

wakes, secondary flow development, and boundary layer flow in an annular low-pressure turbine Cascade: an experimental investigation," *Journal of Turbomachinery*, vol. 141, no. 9, article 091001, 2019.

[23] B. Winhart, M. Sinkwitz, D. Engelmann, F. Di Mare, and R. Mailach, "On the periodically unsteady interaction of wakes, secondary flow development and boundary layer flow in an annular lpt cascade: Part 2—numerical investigation," in *ASME Turbo Expo 2018: Turbomachinery Technical Conference and Exposition*, Oslo, Norway, June 2018.

[24] A. P. Darji, B. D. Baloni, and C. S. Mistry, "Numerical Investigations on Effect of Inflow Parameters on Development of Secondary Flow Field for Linear LP Turbine Cascade," in *ASME 2021 Gas Turbine India Conference*, December 2021.

[25] H. Tsujita and M. Kaneko, "Effects of Shock Wave Development on Secondary Flow Behavior in Linear Turbine Cascade at Transonic Condition," in *Proceedings of the ASME Turbo Expo 2020: Turbomachinery Technical Conference and Exposition*, 2020.

[26] D. Simoni, V. Yepmo, P. Zunino, M. Ubaldi, D. Lengani, and F. Bertini, "Turbine Cascade Profile Loss Sensitivity to Incoming Wake Parameters: Effects of Reduced Frequency, Wake Momentum Defect and Axial Gap," in *Proceedings of the ASME Turbo Expo 2019: Turbomachinery Technical Conference and Exposition*, Phoenix, Arizona, USA, 2019.

[27] H. Kodama, K. I. Funazaki, K. Ito, R. Ikehata, and Y. Koda, "A Method for Estimating Profile Loss of Low Pressure Turbine Blades from the Low Speed Cascade Test Data," in *Proceedings of the ASME Turbo Expo 2019: Turbomachinery Technical Conference and Exposition*, Phoenix, Arizona, USA, 2019.

[28] V. Dossena, G. D'Ippolito, and E. Pesatori, "Stagger angle and pitch-chord ratio effects on secondary flows downstream of a turbine cascade at several off-design conditions," in *ASME Turbo Expo 2004: Power for Land, Sea, and Air*, pp. 1429–1437, Vienna, Austria, June 2004.

[29] T. Behr, *Control of Rotor Tip Leakage and Secondary Flow by Casing Air Injection in Unshrouded Axial Turbines*, Diss, ETH Zurich, 2007.

[30] W. Du, L. Luo, S. Wang, and X. Zhang, "Heat transfer characteristics in a pin finned channel with different dimple locations," *Heat Transfer Engineering*, vol. 41, no. 14, pp. 1232–1251, 2020.

[31] L. M. Seguí, L. Y. M. Gicquel, F. Duchaine, and J. de Laborderie, "Importance of boundary layer transition in a high-pressure turbine cascade using LES," in *ASME Turbo Expo 2018: Turbomachinery Technical Conference and Exposition*, Oslo, Norway, June 2018.

[32] M. E. Nakhchi, S. W. Naung, and M. Rahmati, "DNS of secondary flows over oscillating low-pressure turbine using spectral/hp element method," *International Journal of Heat and Fluid Flow*, vol. 86, p. 108684, 2020.

Hindawi
International Journal of Aerospace Engineering
Volume 2022, Article ID 8785963, 12 pages
https://doi.org/10.1155/2022/8785963

Research Article

Experimental Study on the Aerodynamic Characteristics of Blades at the Last Stage of a Steam Turbine at Off-Design Conditions

Yunfeng Liu,[1,2] **Qiankun Jia**,[1] **Xun Zhou**,[1] **Hongtao Zhang**,[2] **Yufeng Li**,[2] **Zhongqi Wang**,[1] **and Wei Du**[1]

[1]*School of Energy Science and Engineering, Harbin Institute of Technology, Harbin, China*
[2]*Harbin Turbine Company Limited, Harbin, China*

Correspondence should be addressed to Xun Zhou; zhouxun@hit.edu.cn

Received 24 July 2022; Accepted 26 August 2022; Published 9 September 2022

Academic Editor: Qingfei Fu

Experimental investigations have been carried out on the flow characteristics of the last stage long blades operating under off-design conditions. A model turbine test rig similar to a small power station was applied. The last stage blades with a scaling factor of 1 : 4.8 was used for pneumatic experiments. The rotor blade height was 375 mm, and the rotation speed was set to 7200 rpm. Five volumetric flow coefficients were utilized, corresponding to φ =0.61, 0.77, 0.92, 1.02, and 1.15. Pneumatic probes were used to focus on measuring pressures and swirl angles. The variation of different pneumatic parameters along the span and circumferential direction was investigated. The change patterns of the three-dimensional aerodynamic characteristics of the last stage blades during the off-design conditions were revealed. Results indicated that there was a high correlation between the variation of pneumatic parameters and different off-design conditions. In particular, the large meridional expansion angle at the tip led to abrupt changes in the inlet parameters, and the overlap even occupied by 17% blade height. Due to the influence of the exhaust hood, the circumferential static pressure-unevenness was up to 77.8% at the last stage outlet.

1. Introduction

The last stage long blade is the key component of the steam turbine, which has a critical impact on the power and efficiency of the generating unit [1, 2]. The last stage of the low-pressure (LP) turbine can exceed 10% of the total power of the plant, even up to 20%. Therefore, the flow characteristics at the last stage blade seriously restrict the performance of the turbine unit. To meet the challenges posed by global warming and other environmental issues, renewable energy technologies are widely used in the civil power generation field [3]. As a consequence, the large steam turbines are facing increase of peak regulation conditions [4, 5]. The peaking regulation has led to the increase in the operation of the last stage long blades under off-design conditions. It will appear separation, blockage, and other complex turbulent flow, not only endanger the blade safety but also further increase the difficulty of the last stage blade aerodynamic performance evaluation.

Part-load operation is required to pursue the thermal-economic optimization of the plant. This has resulted in a reconsideration of the aerodynamic design of today's steam turbine last stage blades, taking greater account of part-load conditions [6]. The tip/hub ratio of the last stage blades is relatively large, and the parameters are more variable along the radial direction [7]. Thus, the distinct three-dimensional flow characteristic emerges. The nozzle gradually transitions from transonic flow at the root to subsonic flow at the tip, while the rotor blade is the opposite. Bosdas et al. [8] revealed that the long rear stage blades created a relative supersonic flow field at the tip of the rotor. With the development of the advanced steam turbines, the length of

the last stage blades has been up to 1500 mm [9] and the tip/hub ratio is 2.5 [10]. The shock waves generated by the supersonic flow interact with the steam seal leakage flow near the endwall and the secondary flow [11], forming a more complex flow, as well as the non-equilibrium characteristics of wet steam [12], making it more difficult to evaluate the aerodynamic performance of the last stage blades. In addition, the damping structures such as nozzle dehumidification, rotor lacing wire, and shroud further increased the complexity of the last stage flow.

In the previous studies, numerical and experimental methods were widely applied to research the aerodynamic performance of the long last stage blades. Due to the complex and high-cost structure of the turbine test rig, a simplified structure was used in the steam turbine pneumatic experiments. Novak et al. [13] analyzed the flow field distribution of advanced 2D tip profiles of long last stage blades by experimental and numerical methods. The results indicated that due to the supersonic inlet Mach number, a vertical inlet shock wave was observed for the tip cascade. Hála et al. [14] optimized the aerodynamic design of the rotor root section within the given strength requirements. Optical and aerodynamic measurements were performed to investigate the aerodynamic characteristics of the 2D blade cascade representing the last stage rotor mid-span section including off-design conditions by Luxa et al. [15]. The results provided information on the aerodynamic characteristics of important cascades in a wide range of flow patterns including off-design conditions. Senoo and Ono [16] introduced the development of design methods for supersonic turbine airfoils and proposed methods to reduce shock wave losses. Parvizinia et al. [17] verified the aerodynamic performance of the supersonic tip section profile of a low-pressure steam turbine through numerical and experimental studies. Chaluvadi et al. [18] studied the effect of delta-wing vortex transport on the performance of the downstream blade row of a high-pressure axial-flow turbine. The above studies about the turbine blade aerodynamic characteristics only used 2D cascade profiles and air turbines, and 3D blades and wet steam turbines were not mentioned.

The steady numerical method was a reliable way to predict the aerodynamic characteristics of the low-pressure turbine's last stage during windage [19]. Liu et al. [20] and Shao et al. [21] investigated the aerodynamic characteristics of the last stage and the exhaust hood of large-scale steam turbines under different mass flow rates. It was demonstrated that high amplitude aerodynamic fluctuations were found on the rear stage rotor blades in low mass flow cases. Long last stage blades caused an increase in steam flow excitation force under off-design conditions. Cao et al. [22] investigated the parameter variation in the last stage flow field under the low flow rate cases and summarized the condensation and distribution rule of wet steam and the interaction among them. Shibukawa et al. [23] suggested that the unsteady pressure fluctuations in the turbine blade tip region probably had a high correlation with the high dynamic blade stresses through experimental studies. Hoznedl et al. [24] compared the differences in the flow fields on the left and right sides of the final stage by experiments. These differences resulted in dynamic loads on the penultimate rotor blade and potentially shortened service life. Rotor tip leakage flow and passage vortices were the main sources of unsteady flow in the last stage blades. The unsteady fluctuation of the penultimate stage increases with the increasing volumetric flow, while the rear stage decreases [25].

In this work, the three-dimensional aerodynamic performance of the steam turbine last stage blades under different off-design conditions was investigated by experimental methods. A model turbine rig was employed and the fixed and traverse pneumatic probes were used to measure pressure and velocity. The static and total pressure distributions along the span at the inlet, inter-stage, and outlet of the last stage for different volumetric flow coefficients were analyzed. The variations of the last stage reaction degree and the absolute outlet swirl angle under different flow coefficients were compared. In particular, the influence of circumferential pressure-unevenness on the aerodynamic performance of the last stage blades was considered. Eventually, this paper summarized the effects on the last stage efficiency under different off-design conditions. This work provided the fundamental insights needed to guide the design of the turbine's last stage blades.

2. Experimental Approach

2.1. Experiment Setup. Figure 1(a) presents the schematic of the rig in this study. A model steam turbine test rig is applied. This turbine test rig is similar to the rig used by Schatz and Eberle [26], which is a simplified version of a small power plant, except that the electric generator is replaced by a hydrodynamic dynamometer. The water vapor generated by the boiler flows into the high-pressure (HP) turbine and low-pressure (LP) turbine sequentially through the steam conversion valve and pipes. Meanwhile, two dynamometers are mounted on high-pressure and low-pressure turbines, respectively. The exhaust pressure is controlled by a condenser which is connected to the LP turbine. The scaling factor for the tests reported here is 1 : 4.8. And the whole off-design test is carried out in a model scale steam turbine.

As shown in Figure 1(b), the test section includes four LP turbine stages. To perform off-design tests, the three front stages and the last stage are coupled on different shafts which are called A-Rotor and B-Rotor, respectively. The HP turbine and the three front stages of the LP turbine are connected by A-Rotor, while B-Rotor is only used to drive the last stage of the LP turbine. This configuration allows not only to change B-Rotor according to different experimental requirements but also to control the speed of the last stage experimental blades individually. Moreover, the required speed is maintained by the motor dragging the experimental B-Rotor at extremely low loads, making the test section widely applicable. Besides, two dynamometers are connected to A-Rotor and B-Rotor to measure the speed and torque under different off-design conditions.

The steam turbine last stage consists of nozzles and rotor blades. According to the scaling factor, the structural parameters of the experimental blade are calculated. The parameters at the rotor blade are provided. The geometric

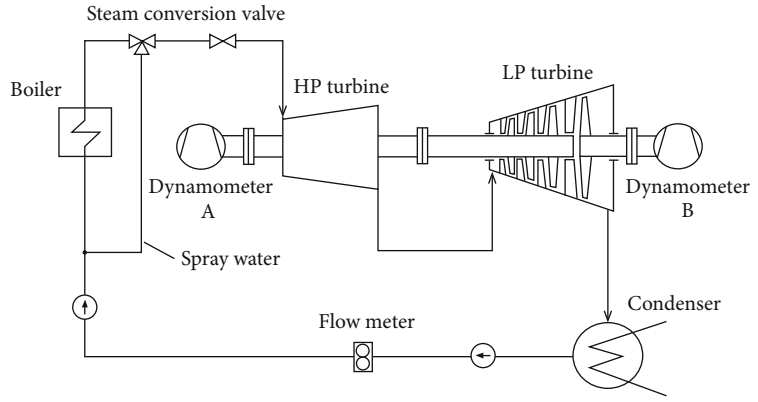

(a) Schematics of the test rig

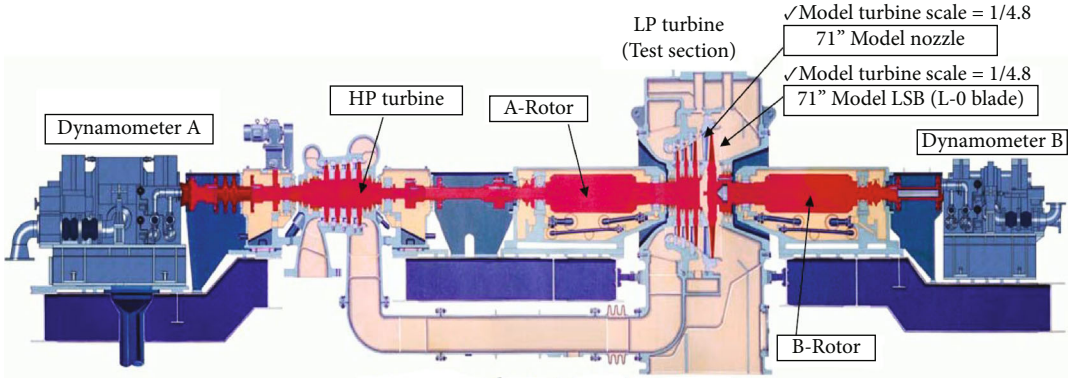

(b) Longitudinal profile of the test section

Figure 1: Model steam turbine test rig.

parameters of the experimental blades are calculated by the scaling factor. The average diameter (d) of the blade wheel and the height (h) of the rotor are 947.92 mm and 375 mm, respectively. The L-0 outlet annulus area (A_{outlet}) is 1.1167m^2 and the rotation speed (n) is set to 7200 rpm. Figure 2(a) provides some photographs of the nozzle and blade wheel, and Figure 2(b) shows the blades assembled in the model steam turbine test rig.

2.2. Pneumatic Measurement. The indication and positions of planes for measurement are shown in Figure 3. Plane 0 and plane 1 are located at the L-0 nozzle inlet and outlet, and plane 2 is positioned at the L-0 outlet. Furthermore, the effect of the non-uniform circumferential distribution of the flow on all planes is captured by circumferentially uniform arrangements of fixed and traverse probes located around the circumference. Fixed probes are used for the measurement of static pressure, while traverse probes are applied for the measurement of total pressure. Figure 3 also displays the details of the arrangement of the pneumatic probes on different measurement cross-sections. Table 1 lists the measurement parameters and probe arrangements. In particular, the velocity is measured via two five-hole probes, one located at the L-0 nozzle inlet (plane 0) and one at the L-0 outlet (plane 2).

To research the off-design aerodynamic characteristics of the last stage blades, each test has been carried out by performing volumetric flow variations whereas the exhaust pressure has been kept almost constant. Five volumetric flow coefficients are considered, φ=0.6, 0.75, 0.9, 1, and 1.1, respectively. For the model turbine test rig, the nominal volume flow (Q_{nv}) is 256.3 m^3/s, and the nominal exhaust pressure ($p_{2,nv}$) is set to 4 kPa. Actually, the measured results do not precisely match the predicted off-design conditions. To find the test conditions closest to the five predicted operating conditions, 14 operating conditions are measured during the test. Table 2 summarizes five test cases from TC1 to TC5, and the relative error of the exhaust pressure (p_2) and volumetric flow coefficients (φ) is calculated between the test value and the prediction value. The relative error of all parameters is lower than 5%. Therefore, the actual test conditions are provided, Q=0.61, 0.77, 0.92, 1.0, and 1.15 Q_{nv}. Although a slight deviation occurs, TC4 (φ=1.02) is still considered to be the design operating condition.

2.3. Parameter Definition. The volumetric flow coefficient φ is defined as [27]:

$$\varphi = \frac{Q}{Q_{nv}}, \tag{1}$$

where the volumetric flow is expressed by Q, and Q_{nv} represents the nominal volumetric flow at the design condition.

(a) L-0 nozzle and blade wheel

(b) Assembled in model steam turbine

FIGURE 2: Photos of the test rig.

Q_{nv} is calculated as:

$$Q_{nv} = A_{\text{outlet}} \cdot c_{ax}, \tag{2}$$

where A_{outlet} and c_{ax} are the L-0 stage outlet annulus area and average axial velocity.

The pressure circumferential-unevenness ξ is written as [28]:

$$\xi = \frac{p_{\max} - p_{\min}}{\bar{p}}, \tag{3}$$

where the mean static pressure is expressed by $\bar{p}$; $p_{\max}$ and $p_{\min}$ indicate the maximum and minimum static pressure.

The reaction degree Ω is defined as [29, 30]:

$$\Omega = \frac{p_1 - p_2}{p_0 - p_2}, \tag{4}$$

where p_0 and p_1 are the average static pressure for the nozzle inlet and outlet, respectively. p_2 is the average static pressure for the rotor outlet.

3. Results and Discussion

3.1. Analysis of Radial Pneumatic Parameters

3.1.1. Pressure Profile. The diameter-height ratio of the steam turbine's last stage blades is small. Therefore, the variations of the pneumatic parameters in the radial direction are highlighted. Figure 4 shows the static pressure distribution in plane 1 for different φ. It has been noticed that the static pressure distribution along the blade span of the L-0 nozzle outlet is very similar under different off-design conditions. For TC2-TC5, the static pressure increases gradually with the rise of blade span, and the max pressure appears at the tip span. The larger the flow coefficient, the higher the static pressure at the same blade span, as shown in

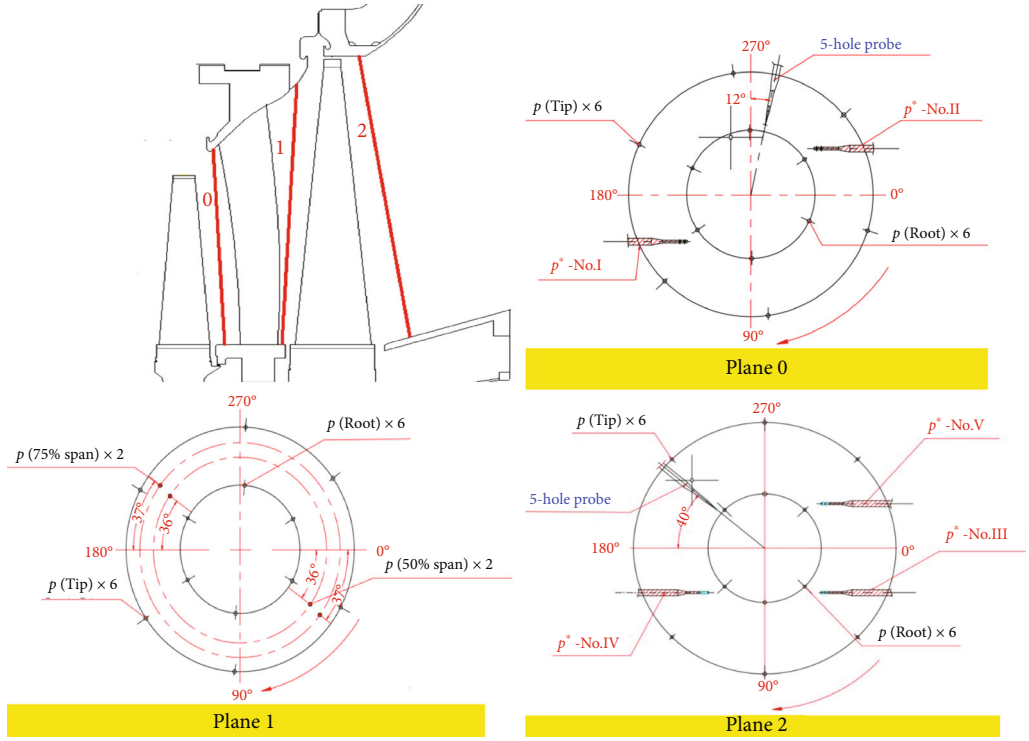

Figure 3: Indication of measurement planes and probe positions.

Table 1: Measured parameters and probe arrangements.

(a) L-0 nozzle inlet (plane 0)

Measured parameters	Probe location	Probe number	Probe type
Static pressure	Tip	6	Fixed
Static pressure	Root	6	Fixed
Total pressure	—	2	Traverse
Velocity	—	1	5-hole traverse

(b) L-0 nozzle outlet (plane 1)

Measured parameters	Probe location	Probe number	Probe type
Static pressure	Tip	6	Fixed
Static pressure	Root	6	Fixed
Static pressure	50% span	2	Fixed
Static pressure	75% span	2	Fixed

(c) L-0 outlet (plane 2)

Measured parameters	Probe location	Probe number	Probe type
Static pressure	Tip	6	Fixed
Static pressure	Root	6	Fixed
Total pressure	—	3	Traverse
Velocity	—	1	5-hole traverse

Figure 4. This demonstrates that a defined set of flow coefficients is the main driver of the pressure distribution. For all test cases, the pressure gradient presents an upward tendency at below 0.75 span. The pressure profile is relatively steep at above 0.75 span, but the pressure gradient decreases, relative to the 0.50-0.75 span. However, the static pressure is reduced at tip span for TC1. Therefore, the max pressure is noticed at 0.75 span for φ=0.61.

The variation of the reaction degrees at the different off-design conditions along the blade span is shown in Figure 5. It illustrates the significant growth of the Ω along the blade span from TC1 to TC5. It seems to present a similar distribution between reaction degrees and pressure. Correspondingly, the Ω is clearly reduced at the tip span for TC1 (φ =0.61). It indicates the decrease of Ω at the tip span as the φ decreases.

Figure 6 shows the total pressure distribution of the L-0 inlet and outlet at the different off-design conditions (TC2-TC5). In the studied test cases, an identical trend is obvious. It is demonstrated that the inlet total pressure highly depends on the changes of flow coefficient. Although the total pressure is essentially constant from the bottom to the tip, two distinct pressure pulsations are noticed at 0.55 span and tip span, as shown in Figure 6(a). It is possible that the inlet total pressure is affected by the penultimate stage rotor lacing wire at the 0.55 span. In addition, the tip overlap of the penultimate rotor blade and the rear stage nozzle accounts for 17% of the rear stage nozzle inlet, and the height is 46 mm by measurement. Due to the influence of tip leakage flow of the penultimate stage rotor blade and the diaphragm cavity, there is a significant drop in the total

Table 2: Summary of test cases.

Test condition	Exhaust pressure (p_2) [kPa]			φ		
	Test	Prediction	Relative error (%)	Test	Prediction	Relative error (%)
TC1	3.80	4	5	0.61	0.60	1.67
TC2	4.16	4	4	0.77	0.75	2.67
TC3	3.98	4	0.5	0.92	0.90	2.22
TC4	4.06	4	1.5	1.02	1.00	2
TC5	4.13	4	3.25	1.15	1.10	4.55

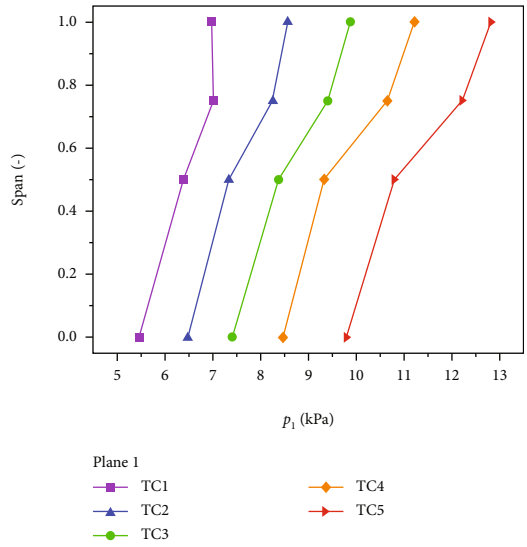

Figure 4: Static pressure distribution in plane 1 for different φ.

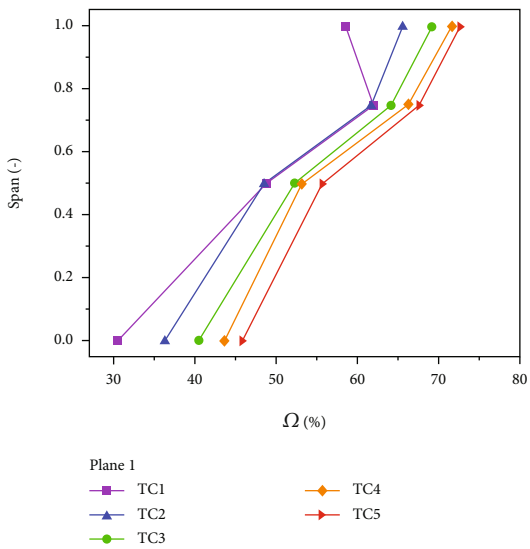

Figure 5: Reaction degree distribution for different φ.

pressure, which indicates that the loss increases in the blade tip region. Figure 6(b) depicts the distribution of total pressure in the L-0 outlet. It presents that the outlet total pressure gradually decreases along the span. For TC3, TC4, and TC5, the φ is the main driver of the total pressure variation at the same span. The pressure pulsations are also observed at the 0.4 span and tip span in all studied cases. However, the total pressure increases firstly and then decreases at the tip span, which is the opposite of the result in Figure 6(a). In particular, for the off-design conditions (TC4 and TC5) with high φ, pressure pulsation also appears at the bottom span, which is not observed in TC2 and TC3. In addition, the results show that the measured pressure difference between TC2 and TC3 is less than 0.5 kPa.

3.1.2. Swirl Angle Profile. The swirl angle is defined as the angle between the absolute velocity and the axial direction. Actually, the swirl angle is considered the key parameter to reflect the performance of the steam turbine last stage blades, especially the outlet absolute swirl angle, which has a great influence on the Leaving Loss. The α_0 and α_2 along the blade span for all test cases are displayed in Figure 7, respectively. It is easy to find the variations of the inlet and outlet swirl angles at the different φ, and also the total pressure distribution in Figure 6. As mentioned above, high correlations between some physical quantities and the flow coefficients characterizing the stage operation are displayed. The plot of the measured inlet swirl angle profile confirms the similarity for all test cases, as shown in Figure 7(a). The α_0 gradually increases along the blade span. Due to the impact of the penultimate stage rotor lacing wire, the α_0 appears at inflection points at the 0.55 span and tip span, which is generally consistent with the total pressure profile in Figure 6(a). In Figure 7(a), the α_0 is reduced suddenly at above 0.95 span, and the larger the φ, the more the swirl angle decreases.

Figure 7(b) demonstrates that the outlet swirl angle distribution is also closely related to the off-design conditions. It is indicated that the α_2 gradually decreases with the increase of φ, which is opposite to the total pressure distribution in Figure 6(b). For almost all test cases, the α_2 follows the same tendency along the span, except for the TC1 (φ =0.61). Compared with Figure 6(b), the outlet swirl angle pulsation at 0.4 span from TC2 to TC5 is also demonstrated. However, near the root (less than 0.15 span), the outlet swirl angle decreases along the span, as shown in Figure 7(b). Actually, for TC1, the α_2 increases along the blade span from α_2 =10° at the root to α_2 = 50° at the tip, which indicates a strongly radial flow at the L-0 outlet. For large flow coefficients (TC3-TC5), the negative outlet swirl angles are illustrated, as shown in Figure 7(b). For TC2, the outlet swirl angle is approximately 0. This means that the outlet steam flows out of the rotor in the axial direction. The α_2 at the same off-design condition from the root to the 0.9 span is essentially constant. However, due to the tip leakage flow at the last stage rotor blade and the diaphragm cavity, the α_2 increases sharply at above 0.9 span, and the swirl angle increases by 40° in almost all studied cases (TC2-TC5).

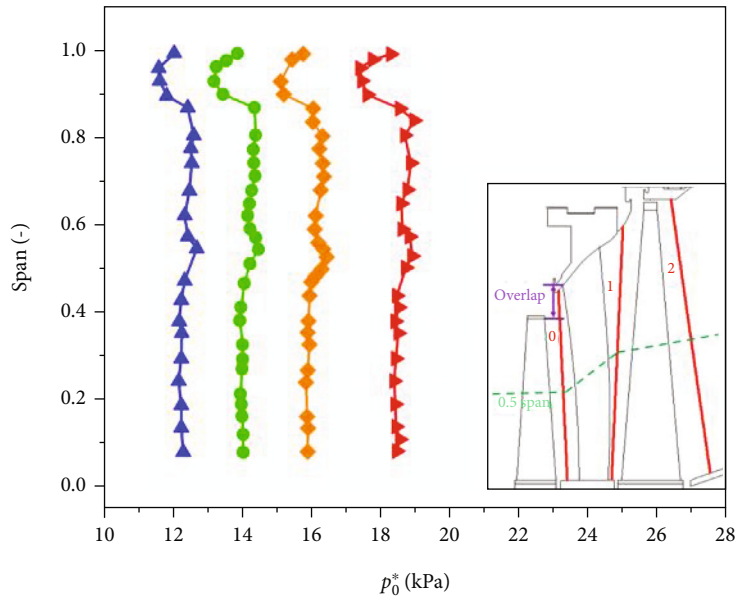

(a) Total pressure at L-0 inlet

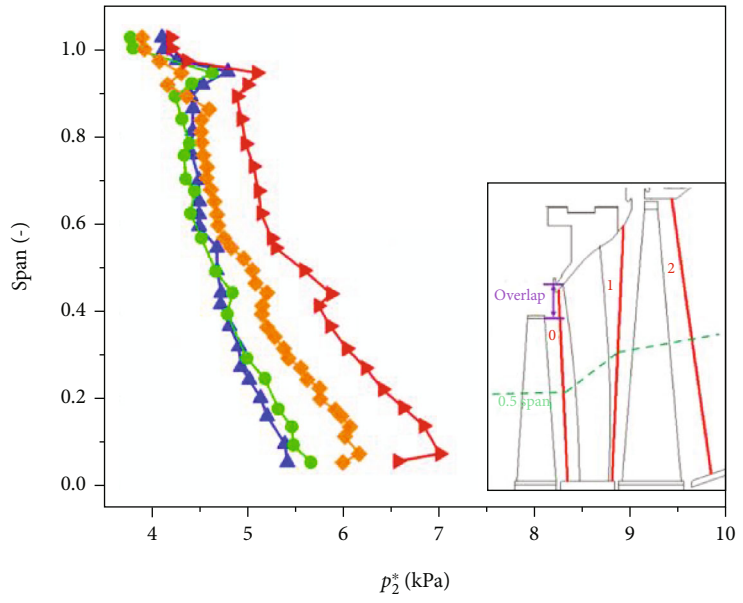

(b) Total pressure at L-0 outlet

FIGURE 6: Total pressure distribution at L-0 inlet and outlet from TC2 to TC5.

Therefore, the whole outlet swirl angle profile shows a slight C-shaped distribution.

3.2. Analysis of Circumferential Pneumatic Parameters

3.2.1. Pressure-Unevenness Study. Although the turbine final stage nozzle and rotor blades are generally symmetrically configured along the circumferential direction, the structures for extraction and exhaust are generally non-symmetrical along the circumference. The non-symmetrical arrangement structures not only cause the degradation of aerodynamic performance but even lead to uneven blade loading and bring safety problems. Figure 8 compares the variation of static pressure circumferential-

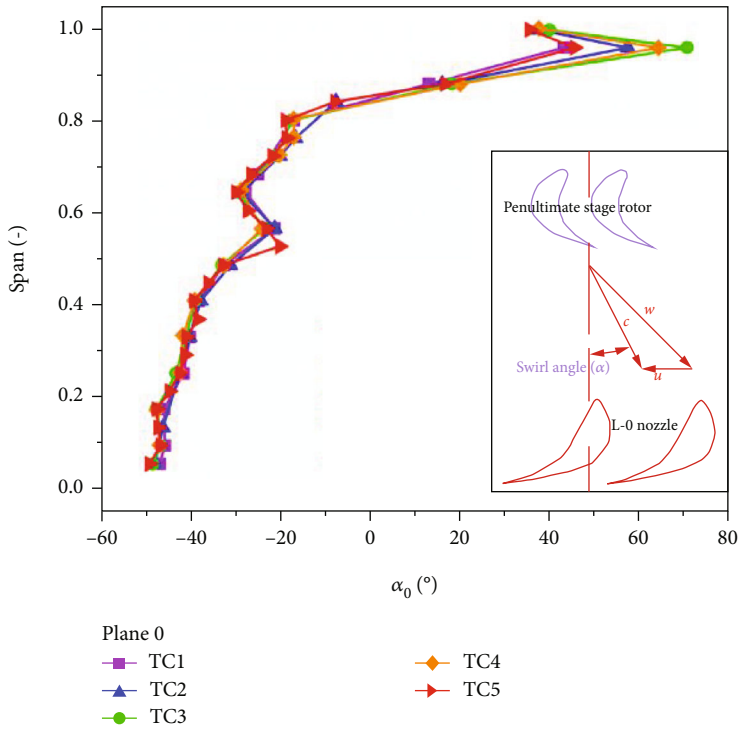

(a) Inlet swirl angle

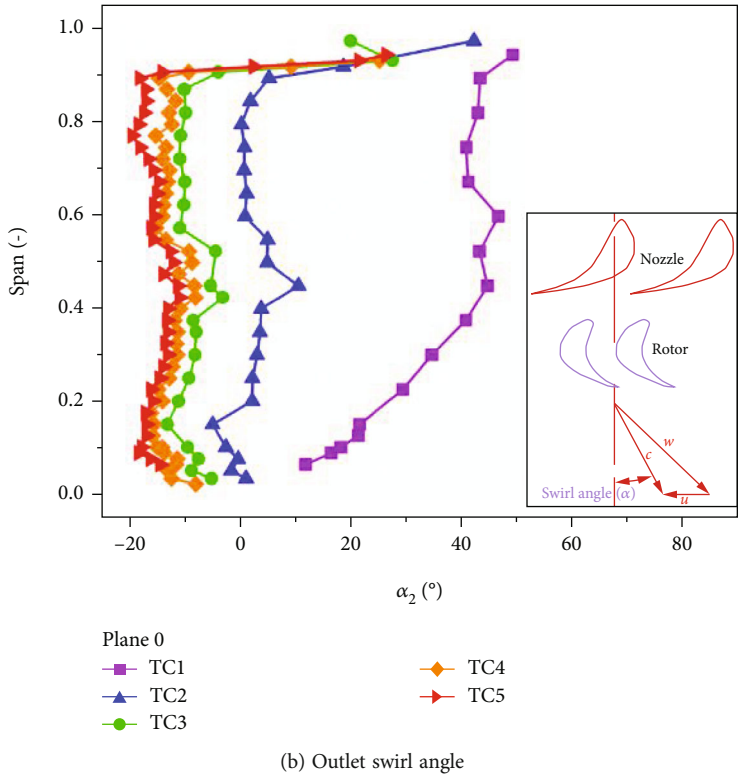

(b) Outlet swirl angle

Figure 7: Swirl angle distribution of the L-0 inlet and outlet for all test cases.

unevenness for different off-design conditions. The result indicates that the ξ at the L-0 outlet is significantly higher than that at the L-0 inlet and nozzle outlet at the different φ. In particular, the ξ at the L-0 outlet grows with the increasing flow coefficient. For the high flow coefficient cases (TC3-TC5), the ξ at the blade tip is significantly higher than at the root, and the growth rate at the tip is greater than that at the root. The measured data presents an increase of the ξ

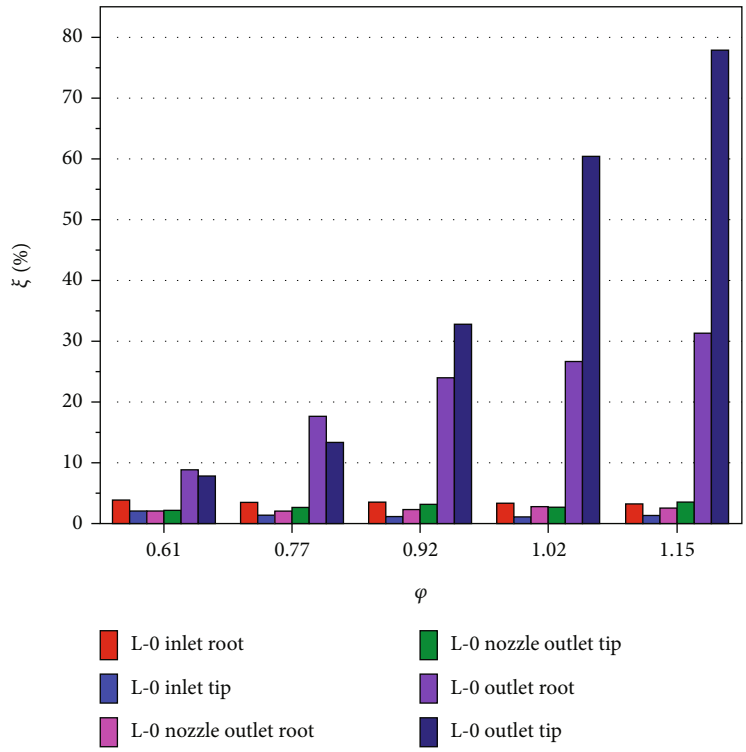

Figure 8: Comparison of static pressure circumferential-unevenness.

at the L-0 outlet root and tip by 4.7% and 17.6% from TC4 to TC5, respectively. Probably due to the effect of the rotor blade tip leakage and the diaphragm cavity, the circumferential pressure distribution at the tip presents big fluctuations in the high φ. Besides, there is the largest ξ (ξ=77.8%) at the L-0 outlet tip for TC5, as shown in Figure 8. The ξ is generally less than 5% at the L-0 inlet and nozzle outlet. It indicates that the φ is not directly relevant to the ξ of the L-0 inlet and nozzle outlet. Moreover, the ξ at the tip is distinctly lower than the root at the L-0 inlet for all test cases. However, the ξ between the tip and root remains basically at the same level at the nozzle exit. As mentioned above, the ξ displays different trends under the different off-design conditions.

3.2.2. Normalized Pressure Analysis. In Figure 9, the normalized static pressure distribution is provided to evaluate the circumferential flow non-uniformity at the root and tip of the L-0 outlet. The normalized static pressure is defined as $p/\bar{p}$. For Figure 9(a), the normalized pressure at the three measurement points (points A, B, and F) in the upper part of the outlet is higher than that in the lower part (points C, D, and E). The normalized static pressure at point A is the highest and the normalized pressure gradually increases with the increase of the φ. Meanwhile, the similar normalized pressure change strategy is shown in Figure 9(b). Most of the normalized static pressures at the points C, D, and E at the L-0 outlet root and tip are less than the average static pressure, and the higher the φ, the smaller the normalized static pressure. There is a downward exhaust facility in the model steam turbine test rig. Therefore, the closer to the bottom exhaust hood, the faster the velocity and the lower the static pressure. Compared to the root, the normalized static pressure at the tip is distinctly higher in the upper part of the L-0 outlet. However, the opposite variation is presented in the lower half. It suggests that the flow is more non-uniform at the tip, but probably more stable at the root, which is also consistent with the findings in Figure 8.

To analyze the circumferential flow non-uniformity, Figure 10 illustrates the normalized total pressure distribution at the L-0 inlet and outlet. The normalized total pressure of the inlet and outlet is defined as p^*/p_{I}^* and p^*/p_{III}^*, respectively. The arrangement of the traverse probes in plane 0 and plane 2 is illustrated in Figure 3. In Figure 10(a), the normalized total pressure is essentially uniformly distributed along the span. It confirms the flow dynamics similarity among TC1, TC3, and TC5 at the L-0 inlet. In addition, the normalized total pressure fluctuation appears at the tip span. Due to the effect of the penultimate stage tip overlap, it may lead to uneven flow across the inlet tip. As shown in Figure 9(b), the results for measurement point No. V and measurement point No. III are relatively close (the $p_{\mathrm{V}}^*/p_{\mathrm{III}}^*$ is close to 1) at the L-0 outlet. The total pressure at the measurement point 4 is relatively higher, and the $p_{\mathrm{IV}}^*/p_{\mathrm{III}}^*$ is basically between 1.05 and 1.1 at the less than 0.95 span. Probably due to the rotation direction, the rotor outlet flow deflects to the left and meets the downward flow on the left side, forming a "convergence point" that causes the local pressure (No. IV) to rise. Compared to Figure 9(b), the circumferential non-uniformity of the L-0

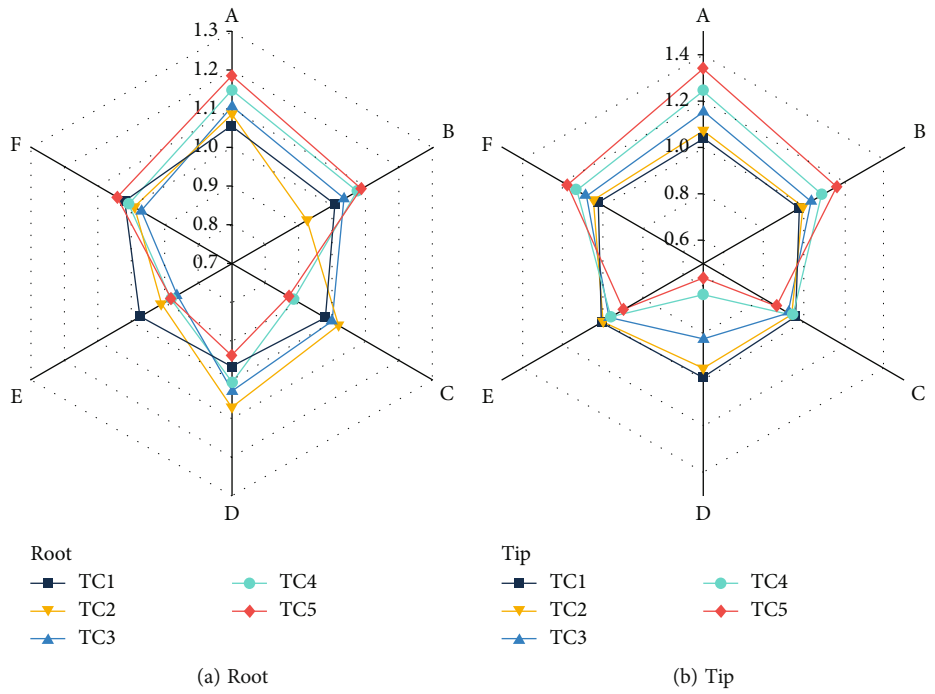

(a) Root (b) Tip

Figure 9: Normalized static pressure distribution at the L-0 outlet.

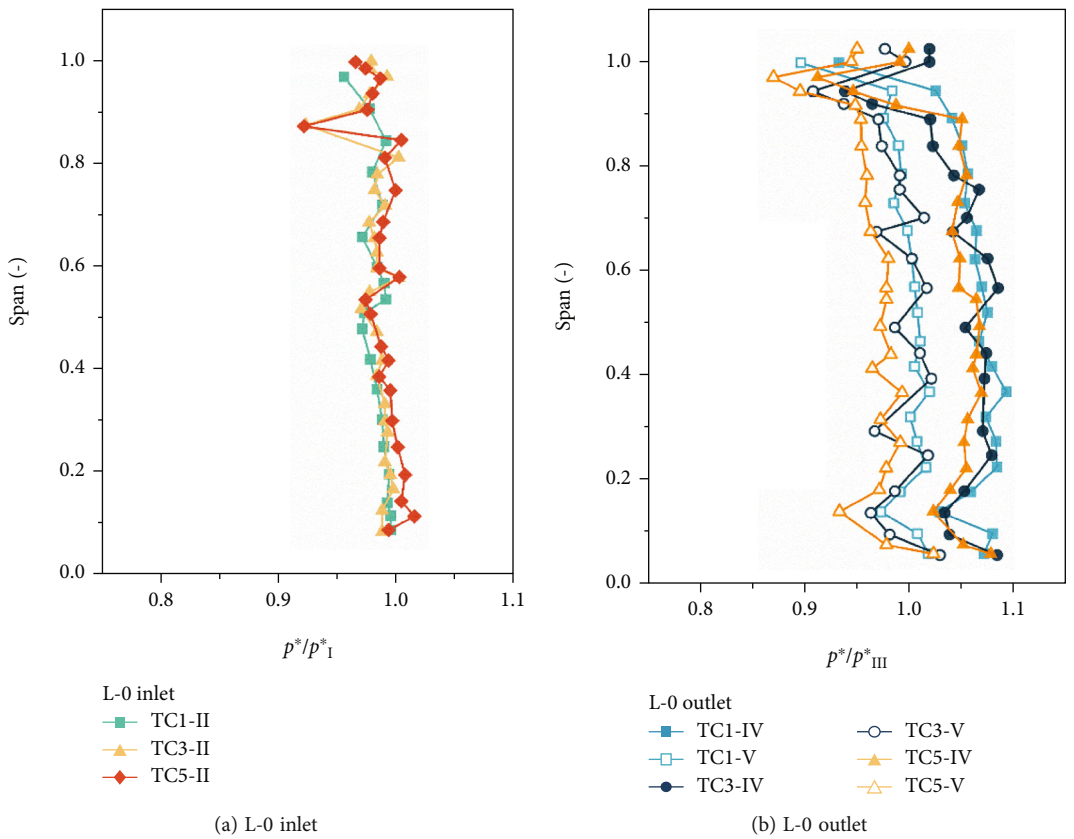

(a) L-0 inlet (b) L-0 outlet

Figure 10: Normalized total pressure distribution at the L-0 inlet and outlet.

outlet total pressure is distinctly less than the static pressure. Moreover, there is no significant correlation between the normalized total pressure distribution of the L-0 inlet and outlet and the φ.

4. Conclusions

Extensive experimental researches on the steam turbine final stage blades with five off-design conditions have been conducted. Varying the volumetric flow of the L-0 was used to characterize the off-design performance. The tests were conducted on a model steam turbine test rig with a scaling factor of 1 : 4.8. This study compared the variation of aerodynamic parameters along the radial and circumferential directions for the final stage blades with different φ. The major conclusions were summarized as follows.

(1) The off-design conditions were an essential driver of the reaction degree changes. The reaction degree gradually increases as the volumetric flow rises. For the four studied cases with the $\varphi \geq 0.77$, the reaction degree variation pattern was the same as the design condition test case (TC4). However, the reaction degree at the tip span decreased significantly for the lowest φ case (TC1). It indicated a larger shift in the three-dimensional flow, which might lead to a decrease in the final stage efficiency. Furthermore, the α_2 variation along the span was also highly correlated with different φ.

(2) The L-0 nozzle had a big meridional expansion angle, leading to a large tip overlap. Due to the influence of tip leakage flow and the diaphragm cavity, the nozzle inlet total pressure was reduced by 4% at above 0.8 span, which would lead to increased flow losses. Besides, the total pressure at the L-0 outlet decreased gradually along the span, and the effect of tip overlap was weakened

(3) The nozzle inlet circumferential flow non-uniformity was negligible, and there was no significant correlation with the off-design conditions. In addition, the flow at the L-0 outlet was non-uniform along the circumference, and the normalized static pressure was larger than the normalized total. For the five off-design conditions, the outlet total pressure non-uniformity was not clearly related to the φ, while the static pressure circumferential-unevenness increased with the increase of the φ.

(4) On the one hand, the reduction of the φ caused variations of the radial parameters, leading to a decrease in efficiency. On the other hand, the outlet circumferential non-uniformity increased with the growth of the φ, which also caused the decrease in the final stage efficiency

Nomenclature

A_{outlet}: Outlet annulus area
d: Blade wheel average diameter [mm]
h: Blade height [mm]
HP/LP: High-pressure/low-pressure turbine
L-0: Last stage
n: Rotation speed [rpm]
p: Pressure [kPa]
Q: Volumetric flow [m^3/s]
c_{ax}: Outlet average axial velocity.

Greek symbols

α: Swirl angle [°]
Ω: Reaction degree
ξ: Static pressure circumferential-unevenness
φ: Volumetric flow coefficient.

Subscripts

0/1/2: Last stage inlet/last stage nozzle outlet/last stage outlet
$*$: Total value
nv: Nominal value
I, II, III, IV, V: Total pressure traverse probe no.

Data Availability

The data used to support the findings of this study are included within the article.

Conflicts of Interest

The authors declare that there is no conflict of interest regarding the publication of this paper.

Acknowledgments

The authors acknowledge the financial support provided by National Science and Technology Major Project (No. 2017-II-0007-0021).

References

[1] A. S. Leyzerovich, *Steam Turbines for Modern Fossil-Fuel Power Plants*, River Publishers, 2021.

[2] I. McBean, S. Havakechian, and P.-A. Masserey, "The development of long last stage steam turbine blades," *Turbo Expo: Power for Land, Sea, and Air*, vol. 7, pp. 2245–2256, 2010.

[3] International Energy Agency, *World Energy Outlook 2021*, International Energy Agency, Paris, 2021.

[4] M. Richter, F. Möllenbruck, F. Obermüller et al., "Flexibilization of steam power plants as partners for renewable energy systems," in *2016 Power Systems Computation Conference (PSCC)*, pp. 1–8, Genoa, Italy, 2016.

[5] P. Eser, A. Singh, N. Chokani, and R. S. Abhari, "Effect of increased renewables generation on operation of thermal power plants," *Applied Energy*, vol. 164, pp. 723–732, 2016.

[6] A. S. Karakurt, "Performance analysis of a steam turbine power plant at part load conditions," *Journal of Thermal Engineering*, vol. 3, no. 2, pp. 1121–1128, 2017.

[7] T. Tanuma, "Development of last-stage long blades for steam turbines," in *Advances in Steam Turbines for Modern Power Plants, Woodhead Publishing*, pp. 279–305, Woodhead Publishing, 2017.

[8] I. Bosdas, M. Mansour, A. I. Kalfas, R. S. Abhari, and S. Senoo, "Unsteady flow field and coarse droplet measurements in the

last stage of a low-pressure steam turbine with supersonic airfoils near the blade tip," *Journal of Engineering for Gas Turbines and Power*, vol. 139, no. 9, 2017.

[9] H. Fukuda, H. Ohyama, T. Miyawaki, K. Mori, Y. Kadoya, and Y. Hirakawa, "Development of 3,600-rpm 50-inch/3,000-rpm 60-inch ultra-long exhaust end blades," *Mitsubishi Heavy Industries Technical Review*, vol. 46, no. 2, pp. 18–25, 2009.

[10] S. Senoo, H. Ono, T. Shibata et al., "Development of titanium 3600rpm-50inch and 3000rpm-60inch last stage blades for steam turbines," *International Journal of Gas Turbine, Propulsion and Power Systems*, vol. 6, no. 2, pp. 9–16, 2014.

[11] C. Liu, J. Zhang, D. Jia, and P. Li, "Experimental and numerical investigation of the transition progress of strut-induced wakes in the supersonic flows," *Aerospace Science and Technology*, vol. 120, p. 107256, 2022.

[12] L. Li, Y. Li, X. Xie, and J. Li, "Quantitative evaluation of wetness losses in steam turbines based on three-dimensional simulations of non-equilibrium condensing flows," *Proceedings of the Institution of Mechanical Engineers, Part A: Journal of Power and Energy*, vol. 228, no. 6, pp. 708–716, 2014.

[13] O. Novak, M. Bobcik, M. Luxa et al., "Turbine cascades of last stage blades for wide range of operating conditions," *International Journal of Turbomachinery, Propulsion and Power*, vol. 4, no. 4, p. 33, 2019.

[14] J. Hála, M. Luxa, D. Šimurda et al., "Optimization of root section for ultra-long steam turbine rotor blade," *Journal of Thermal Science*, vol. 27, no. 2, pp. 95–102, 2018.

[15] M. Luxa, D. Šimurda, P. Safarik, J. Synác, and B. Rudas, "High-speed aerodynamic investigation of the midsection of a 48 rotor blade for the last stage of steam turbine," in *10th European Conference on Turbomachinery Fluid Dynamics & Thermodynamics*, Lappeenranta, 2013.

[16] S. Senoo and H. Ono, "Development of design method for supersonic turbine aerofoils near the tip of long blades in steam turbines: part 2—configuration details and validation," *Turbo Expo: Power for Land, Sea, and Air*, vol. 55201, article V05BT25A002, 2013.

[17] M. Parvizinia, C. Berlich, F. Truckenmüller, and H. Stuër, "Numerical and experimental investigations into the aerodynamic performance of a supersonic turbine blade profile," *Turbo Expo: Power for Land, Sea, and Air*, vol. 41707, pp. 1349–1358, 2004.

[18] V. Chaluvadi, A. Kalfas, and H. Hodson, "Vortex transport and blade interactions in high pressure turbines," *Journal of Turbomachinery*, vol. 126, no. 3, pp. 395–405, 2004.

[19] R. Sigg, C. Heinz, M. Casey, and N. Sürken, "Numerical and experimental investigation of a low-pressure steam turbine during windage," *Proceedings of the Institution of Mechanical Engineers, Part A: Journal of Power and Energy*, vol. 223, no. 6, pp. 697–708, 2009.

[20] B. Liu, J. Yang, D. Zhou, X. Zhu, and Z. Du, "Numerical investigations of flow features in a low pressure steam turbine last stage under different mass flow rates," *Turbo Expo: Power for Land, Sea, and Air*, vol. 56796, article V008T26A022, 2015.

[21] S. Shao, Q. Deng, H. Shi, Z. Feng, K. Cheng, and Z. Peng, "Numerical investigation on flow characteristics of low pressure exhaust hood under off-design conditions for steam turbines," *Turbo Expo: Power for Land, Sea, and Air*, vol. 5B, article V05BT25A031, 2013.

[22] L. Cao, J. Wang, H. Luo, H. Si, and R. Yang, "Distribution of condensation droplets in the last stage of steam turbine under small flow rate condition," *Applied Thermal Engineering*, vol. 181, p. 116021, 2020.

[23] N. Shibukawa, T. Tejima, Y. Iwasaki, I. Murakami, and I. Saito, "A correlation between vibration stresses and flow features of steam turbine long blades in low load conditions," *Turbo Expo: Power for Land, Sea, and Air*, vol. 7, pp. 2437–2446, 2011.

[24] M. Hoznedl, M. Kolovratník, O. Bartoš, K. Sedlák, R. Kalista, and L. Mrózek, "Experimental research on the flow at the last stage of a 1090 MW steam turbine," *Proceedings of the Institution of Mechanical Engineers, Part A: Journal of Power and Energy*, vol. 232, no. 5, pp. 515–524, 2018.

[25] I. Bosdas, M. Mansour, A. I. Kalfas, R. S. Abhari, and S. Senoo, "Unsteady wet steam flow field measurements in the last stage of low pressure steam turbine," *Journal of Engineering for Gas Turbines and Power*, vol. 138, no. 3, 2016.

[26] M. Schatz and T. Eberle, "Experimental study of steam wetness in a model steam turbine rig: presentation of results and comparison with computational fluid dynamics data," *Proceedings of the Institution of Mechanical Engineers, Part A: Journal of Power and Energy*, vol. 228, no. 2, pp. 129–142, 2014.

[27] A. Mambro, F. Congiu, E. Galloni, and L. Canale, "Experimental study and modelling of the ventilation power and maximum temperature of low-pressure steam turbine last stages at low load," *Applied Energy*, vol. 241, pp. 59–72, 2019.

[28] J. Gao, M. Wei, W. Fu, Q. Zheng, and G. Yue, "Experimental and numerical investigations of trailing edge injection in a transonic turbine cascade," *Aerospace Science and Technology*, vol. 92, pp. 258–268, 2019.

[29] S. L. Dixon and C. Hall, *Fluid Mechanics and Thermodynamics of Turbomachinery*, Butterworth-Heinemann, 2013.

[30] W. Gardner, *Energy Efficient Engine: High Pressure Turbine Uncooled Rig Technology Report*, 1979.

Hindawi
International Journal of Aerospace Engineering
Volume 2022, Article ID 5899199, 22 pages
https://doi.org/10.1155/2022/5899199

Research Article

Fill-In and Boiling Transition Characteristics during the Liquid Oxygen Chill-Down Process in a Vertical Exit-Contracted Pipe

Jiaqi Zhang, Ke Wang, and Lanwei Chen

Science and Technology on Scramjet Laboratory, College of Aerospace Science and Engineering, National University of Defense Technology, Changsha 410073, China

Correspondence should be addressed to Jiaqi Zhang; amatyer_a@hotmail.com

Received 2 July 2022; Accepted 27 July 2022; Published 23 August 2022

Academic Editor: Yiheng Tong

Liquid oxygen chill-down in a vertical exit-contracted pipe was investigated experimentally. The wall temperatures were recorded in detail to describe the filling and chill-down process of the experimental section. Two quenching fronts, the exit one and the inlet one, were detected, and their propagations were found. Results show that the chill-down process is controlled mainly by the formation and propagation of quenching front, which are determined by the pressure level. With the increase of pressure, the roles of both propagation of quenching front and inlet quenching front undergo decreasing. On the vertical section, the effect of circumferential position was discussed in detail and the dominant point was identified, which determines the boiling transition time of the dominated points on the current cross-section. Based on the experimental data, two correlations were suggested for dominant point and dominated points, respectively, to predict heat flux on Leidenfrost, heat transfer coefficient on Leidenfrost, and critical heat flux. One equation was approved to predict heat transfer coefficient on critical heat flux point for both sorts of points. All of these correlations could produce reliable predictions.

1. Introduction

Liquid oxygen (LO_2) and liquid methane (LCH_4) are characterized by low-cost, nontoxic, high performance compared to hypergolic propellants, and both of them could be produced on Mars [1, 2]. In this way, a number of projects have been put forward to support future exploration missions using this cryogenic propellant combination [3]. Systematical demonstrations indicated that for space propulsion using this combination, the primary technical risks included the cryogenic fluid management (CFM) and the low-pressure engine technology [4–6].

A number of studies have been put forward to improve the technology readiness level (TRL) for CFM system [3]. For this system, cryogenic fluid could be the liquid phase when the container or pipe are cooled to the liquid temperature. In this way, cryogenic chill-down in the transportation pipe is one of the basic processes here, especially for refueling and transportation of the cryogenic propellants [7]. With the cryogenic fluid first flowing into the pipe with room temperature, flash vaporization would happen in the pipe. Figure 1 gives a typical process of cryogenic chill-down. With the pipe temperature decreasing, fluid pattern in the pipe undergoes film boiling, transition boiling, nucleate boiling, and single phase in sequence. These 4 flow patterns are divided by 3 boiling transition points, Leidenfrost (LFP), critical heat flux (CHF), and onset of nucleate boiling (ONB) [8].

A number of studies have been put forward to investigate the cryogenic chill-down in the transport pipeline. A series of visual studies have been put forward [9, 10], and based on them, a series of phenomenological models have been set up to model the cryogenic chill-down process [11, 12]. For setting up more reliable model, recently, a number of experimental studies have been performed [13–21] to correlate the heat transfer coefficients for various boiling patterns and boiling transition points (LFP, CHF). It is believed that in the current stage, correlations approved by Darr et al. [15, 16] could obtain general

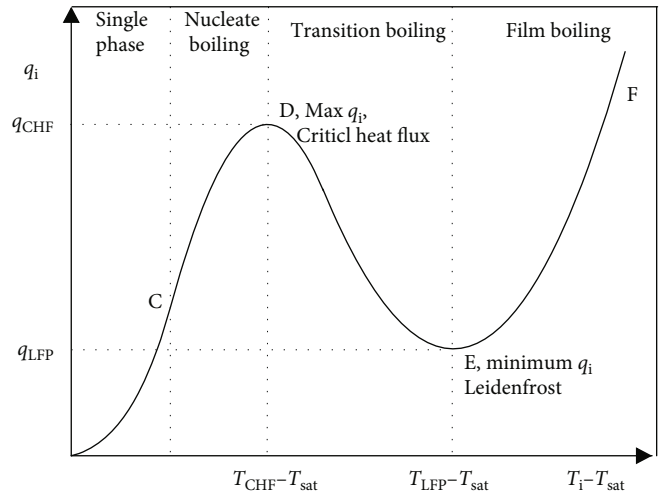

Figure 1: Typical boiling curve and flow patterns for chill-down process.

applications for transport pipe. Based on the improvement on models, a couple of reliable numerical results have been obtained [22, 23].

For low-pressure cryogenic engine, the primary technical difficulty is the instable combustion associate with the two-phase injection produced by cryogenic chill-down [24]. As Figure 2 [25] shows, taking LO_2 for example, before start-up, components upstream of point G would be chilled completely by LO_2 outflow through the prechilling valve. During the start-up process, liquid propellant flows into the components downstream of point G in ambient temperature, which produces two-phase injection and instable combustion in the combustion chamber of the engine [24]. Basically, this phenomenon could be avoided by chilling the components downstream point G before start-up [26]. However, in most cases, the feasibility of this process is determined mainly by the engine procedure. Furthermore, it has been found that two-phase injection could not be avoided even after start-up process [27].

Cryogenic chill-down in low-pressure engine is characterized by the components downstream point G, with a flow contraction on the exit, known as injector, which could be reduced to an exit-contracted pipeline as Figure 3 shows [8, 28]. This is much different from that in transportation pipe taking CFM system as the investigation background, without any flow contraction on the exit.

In the previous studies, cryogenic chill-down in exit-contracted pipe has not been distinguished from cryogenic chill-down in transport pipe. A series of pioneered experimental studies on cryogenic chill-down in the horizontal exit-contracted pipe have been performed by the present authors [8, 28, 29]. Chill-down process was discussed, and boiling transition points were correlated. It has been found that boiling transition points could be well correlated by formats from pool boiling for the exit-contracted pipe, rather than formats from flow boiling from transport pipe [8]. However, the latest study showed that the quenching front seems to be formed in the center length in the horizontal exit-contracted pipe, then propagates to the both ends of the pipe during the chill-down process. In addition, gravity or the circumferential position (bottom, top, or side) plays significant role [29]. This induces extra difficulty to model the heat transfer and transition boiling points in exit-contracted pipe, which is much different from that in transport pipe [16].

It has been concerned that the effects of both gravity and propagation of the quenching front play significant roles in the previous study that [29]. In the present study, for excluding the effect of gravity, vertical pipe would be applied instead of horizontal pipe. In this way, experimental study would be performed to investigate the chill-down process by a constant flow rate of LO_2 in a vertical exit-contracted pipe. A series of tests with the same flow rate and various pressure in the pipe would be performed. Chill-down process would be tracked, by which the propagation of quenching front would be investigated. Based on these data, boiling transition points would be discussed, and q_i and h_i on these points would be correlated for vertical pipe section.

2. Experimental Methodology

2.1. Experimental Platform. Figure 4 gives the experimental platform applied in the present study. It is the LO_2 branch of a typical test platform for cryogenic engine. Compared to the previous one applied in the previous studies [8, 28], the present platform has been upgraded, where the previous 100 L/5.5 MPa LO_2 tank is replaced by a 500 L/10 MPa one. Other parts of the present platform are the same with the previous ones. As shown in the figure, flow rate of the fluid is controlled by the Venturi nozzle.

2.2. Experimental Section and Measurement Approach. Figure 5 gives the experimental section in detail. The shape of experimental section applied could be drawn in Figure 5(a), which also indicates the necessary sensors measuring the pressure and temperature of the fluid. As shown in the figure, a pressure sensor (PT301) and a temperature sensor (PT100) are set up on the experimental section to measure the pressure and temperature of the fluid,

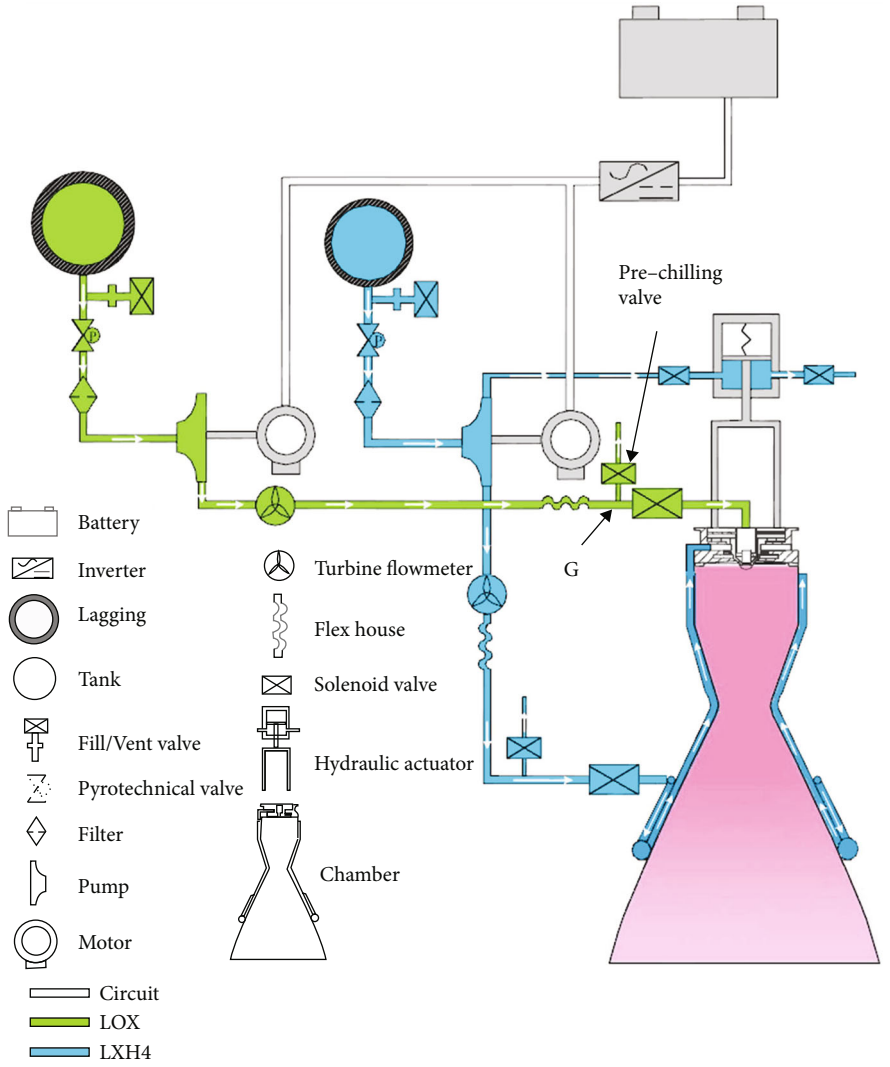

Figure 2: Sketch of a typical low-pressure cryogenic engine [25].

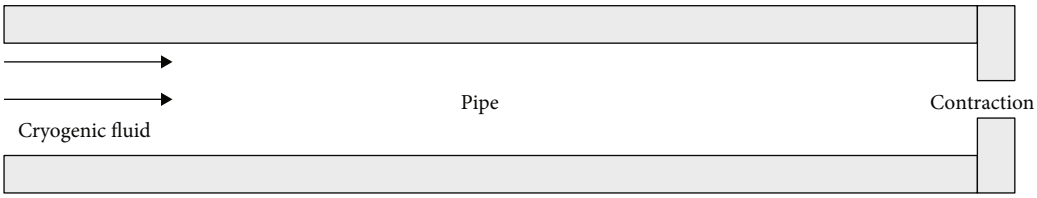

Figure 3: Pipe with a contraction on the exit.

respectively, in the section. 13 T_o sensors (T-type thermocouples) were welded on the outer surface of the experimental section, and they were distributed on 5 cross-sections (various L_{se}) as Figure 5(a) shows. Figure 5(b) gives the cross-section (vertical) on $L_{se} = 1.55$ m, where the 2 sensors, denoted by 1.55-1 and 1.55-2, were welded on the bottom and south-side of the pipe, respectively. The cross-section (horizontal) for other L_{se} could be shown in Figure 5(c), which shows for every section, 3 sensors were set up on the west, south, and east of the pipe in turn (2 sensors on the west and south for $L_{se} = 0.3$ m, denoted by 0.3-1 and 0.3-2). T_o data were recorded by temperature scanner (EX32A). All of the above sensors are with the scan rate of 1000 Hz.

2.3. Other Conditions. For minimizing the potential deviations including nitrogen solution in LO_2 and flow rate oscillations, the test process were well designed and illustrated as shown in reference [1], which would not be repeated here.

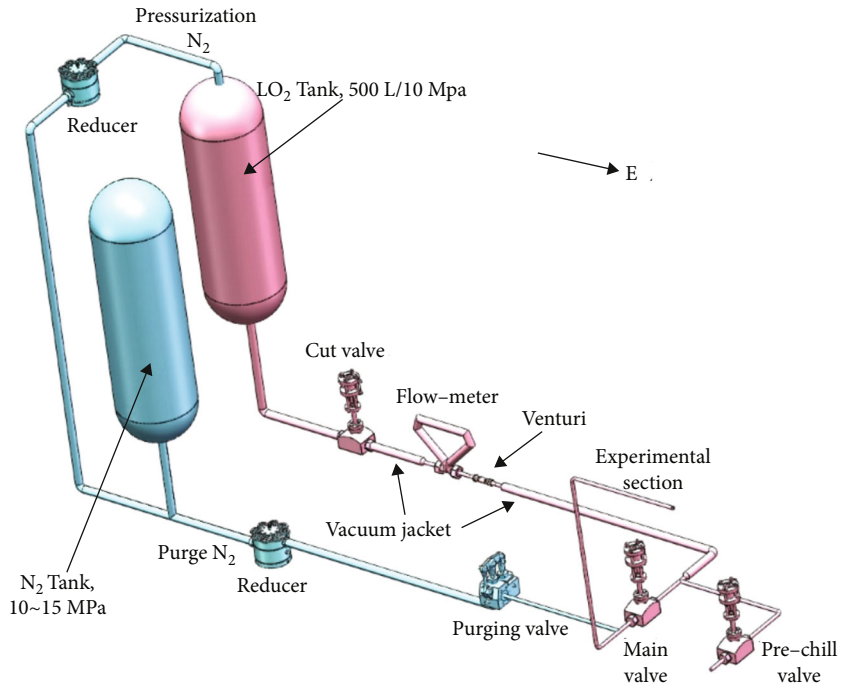

Figure 4: Experimental system of the present study.

3. Experimental Results

3.1. Basic Results. Four tests were performed, and related conditions and results could be listed in Table 1. It shows that the present series of tests are all with the similar flow rate and various A_{inj}. With the decrease of A_{inj} (Exp. 1~4), pressure in the experimental section shows the increasing manner. This indicates that the P_{ss} range is from 0.328 to 1.325 MPa.

3.2. Data Processing and Boiling Transition Points. Parameters in the pipe as well as T_o data were measured for all of the four tests. By processing T_o data, T_i and q_i were obtained because most discussions next would be based on these 2 parameters. Here, T_i would be determined according to reference [30], and q_i would be obtained by numerical methods introduced in the previous studies [28], which would not be repeated here anymore.

Based on T_i and q_i data, boiling curves could be drawn. In this way, boiling transition points, LFP, and CHF could be determined as well. These two points could be identified in the boiling curve easily, which indicate the minimum q_i point and maximum q_i point, respectively.

3.3. Uncertainty. The present study focuses on the comparison between experimental values and predicted values for T_{LFP}, q_{LFP}, T_{CHF}, and q_{CHF}. The experimental values depend mainly on the T_o measurement, physical properties as well as the geometric parameter of the pipe. On the other hand, as shown in the correlations, the predicted values depend mainly on the measured pressure and geometric parameter of the pipe. These factors could be shown in Table 2. Furthermore, the respective mean absolute errors (MAE) can be defined as Equation (1) shows [31].

$$\text{MAE} = \frac{1}{N}\sum \frac{\left|V_{exp} - V_{pre}\right|}{V_{exp}} \times 100\%. \quad (1)$$

3.4. Basic Chill-Down Process. Figure 6 shows all of the T_i curves as well as T_p, T_{sat}, and P_p curves to show the chill-down process for Exp. 1. As shown in the figure, during the chill-down process, T_p, T_{sat}, and P_p curves show the similar manner with the curves recorded in the previous studies [8, 28]. It also shows that a typical T_i curve is composed by three sequent phases as follows.

(1) Phase I: the initial linear decrease phase. In this phase, T_i decreases in a linear manner, which indicates the inner flow is on the film boiling. LFP, the transition point between film boiling and transition boiling, could be seen as the transition point between phases I and II as well

(2) Phase II: the sudden decrease followed by phase I. This phase is with the shortest period, in which T_i decreases dramatically. This phase involves both transition boiling section and nucleate boiling section, and CHF, the transition point between transition boiling and nucleate boiling, sometimes would be seen as the central point of it

(3) Phase III: the gradual decrease followed by phase II. In this phase, T_i decreases gradually, which indicates the inner flow is the single-phase flow. As shown in Figure 1, the transition point between phase II and phase III is denoted as ONB, which always indicates the end of chill-down

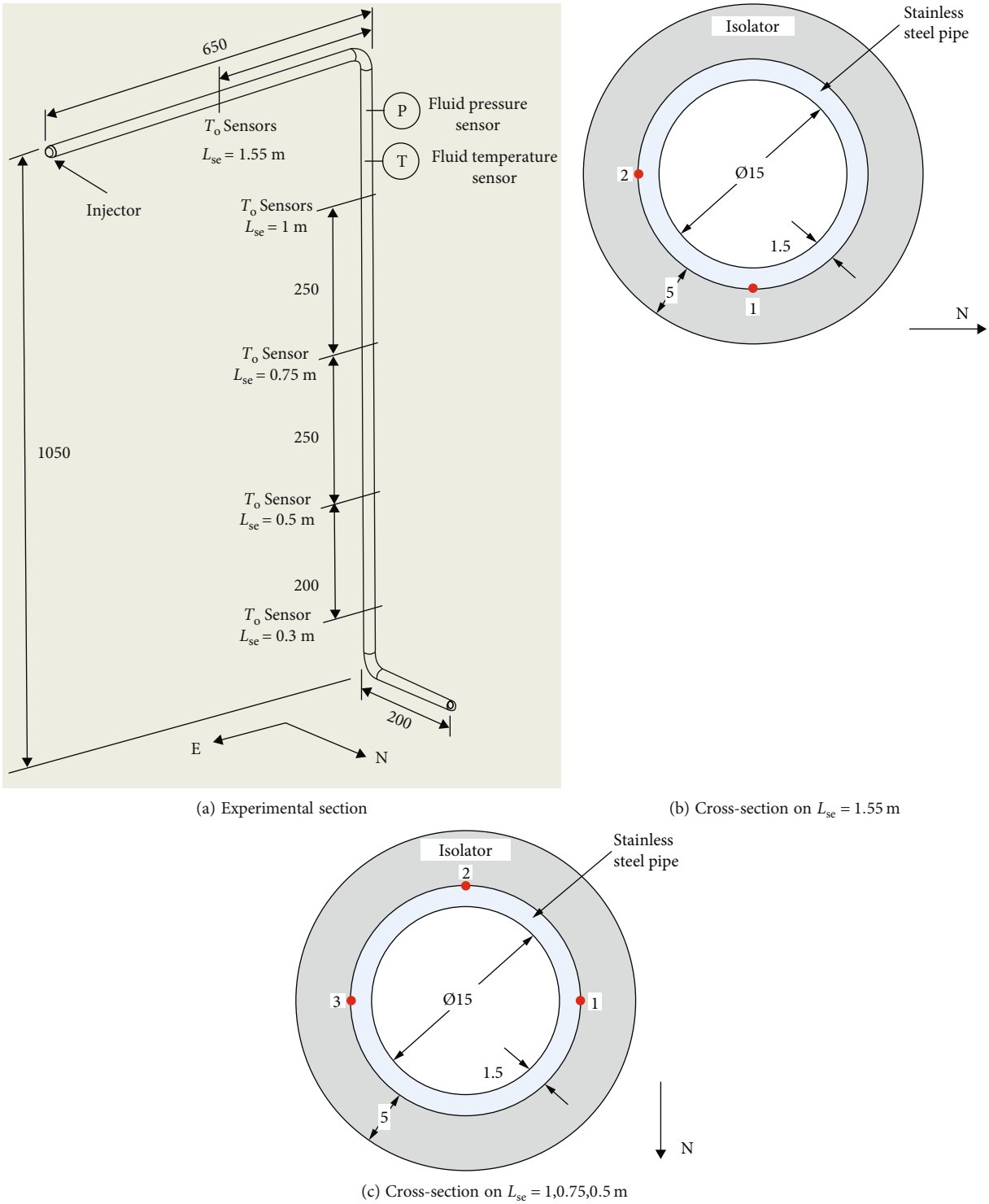

Figure 5: Details on the experimental section, unit: mm.

As shown in Figure 6, for Exp. 1, T_i on L_{se} = 1.55 m decreases at first, followed by L_{se} = 0.3 m, 1 m, 0.75 m, and 0.5 m in turn. Similarly, LFP happens in L_{se} = 1.55 m at first, followed by L_{se} = 0.3 m, 1 m, 0.75 m, and 0.5 m in turn. This indicates that two quenching fronts (QF) are formed on the exit and inlet of the experimental section independently. In the current stage, the exact positions of them could not be decided yet. However, based on the current information, the characteristics of QF formation and propagation could be approved.

It is evident that the QF formed near the exit propagates backward, from somewhere downstream of L_{se} = 1.55 m to the inlet section. It gets to L_{se} = 1.55 m, 1 m, 0.75 m, and 0.5 m in turn and produces boiling transitions on these points. On the other hand, the inlet QF propagates forward from the inlet section to the exit, and it gets to L_{se} = 0.3 m

Table 1: Experimental conditions and results.

Parameters	Exp. 1	Exp. 2	Exp. 3	Exp. 4
Injector type	Orifice	Pintle	Pintle	Orifice
A_{inj} (mm)	110.6	67.2	33	12
$\dot{m}$ (kg/s, start)	0.44	0.435	0.429	0.417
$\dot{m}$ (kg/s, end)	0.45	0.444	0.438	0.426
G (kg/(m^2•s), end)	2546	2513	2478	2411
Re (end)	259192	270824	319074	329295
T_p (K, end)	101.5	104	112	115
$T_{sat} - T_p$ (K, subcooling, end)	1.65	2.06	3.3	9.64
P_{peak} (MPa, start)	0.586	0.843	1.678	3.049
P_{ss} (MPa, end)	0.328	0.41	0.77	1.325

Table 2: Summary of the uncertainties.

Parameters	Uncertainty
Fluid pressure (%)	0.5
Fluid temperature (K)	1
Outer wall temperature (K)	1
Pipe D_i and D_o (mm)	0.01
Mass flow rate (%)	1
T_o (K)	1
T_i (K)	2
q_i (%)	5

and produces boiling transition here. It has to be noted that QFs get to $L_{se} = 1.55$ m and $L_{se} = 0.3$ m almost simultaneously at 10 s. However, after that, it seems like that the inlet QF does not propagate forward, and the vertical section is chilled by the exit QF.

As shown in Figure 7, for Exp. 2, T_i on $L_{se} = 1.55$ m decreases at first, followed by $L_{se} = 1$ m, 0.75 m, 0.3 m, and 0.5 m in turn, and LFP shows the similar manner. However, as shown in Figure 8 and Table 3, for Exp. 3, T_i on $L_{se} = 1.55$ m decreases at first, followed by $L_{se} = 1$ m, 0.75 m, 0.5 m, and 0.3 m in turn, and LFP shows the similar manner. However, as shown in Figure 9 and Table 3, for Exp. 4, T_i on $L_{se} = 1.55$ m decreases at first. After that, T_i values on $L_{se} = 1$ m, 0.75 m, and 0.5 m decrease with the similar slope, which are obvious prior to $L_{se} = 0.3$ m. This indicates that QF on $L_{se} = 0.3$ m happens at first for Exp. 1, at the fourth place for Exp. 2, and at last for Exp. 3 and Exp. 4.

3.5. Mechanisms of the Chill-Down Process and the Quenching Front Propagation. As discussed above, especially Table 3, obviously, pressure plays significant role on the chill-down process. In another word, chill-down process is controlled by the formation and propagation of QFs, which is determined by the pressure level. In this way, the key point here is how to explain the relationship between pressure and the formation and propagation of QFs.

Apparently, these relationships are obvious. For Exp. 1 and Exp. 2 (low pressure relatively), the propagation of the exit QF determines the LFP of the experimental section for $L_{se} = 0.5$ m and its downstream, and LFP on $L_{se} = 0.3$ m are likely to be controlled by the inlet QF. For Exp. 3 (medium pressure relatively), it seems like that LFPs on all of the L_{se} points measured are controlled by the backward propagation of the exit QF. However, for Exp. 4 (high pressure relatively), the exit QF gets to $L_{se} = 1.55$ m. After that, QFs form almost simultaneously on all of the measured L_{se} points except $L_{se} = 0.3$ m; then, one of the QF (formed around $L_{se} = 0.5$ m) propagates to form LFP on $L_{se} = 0.3$ m.

In this way, the overall chill-down process in the experimental section could be described. For low-pressure cases, as the LO_2 flows into the experimental section, it produces intensive evaporation, and liquid core surrounded by the vapor flows to the exit. Because of the contraction on the pipe exit, outflow of the vapor-liquid mixture would be chocked to enhance the system pressure. Simultaneously, because the flow contraction is with high temperature, only vapor could flow out, which produces the liquid accumulation around the injector. As a result of liquid accumulation, heat transfer is enhanced, and QF is formed here at first. After that, QF moves from the exit of the pipe to the upstream of the experimental section. This process is similar with that discussion before [29]. For medium pressure cases, this process does not show obvious change. The only difference is that the duration is shortened by the enhancement of h_{FB} produced by enhanced pressure. For high pressure relatively, the propagation of exit QF also plays significant role on the section near the exit. However, in most vertical section, QFs are formed almost simultaneously for all of the three L_{se}. This indicates that for this case, the role of QF propagation decreases.

On the other hand, simultaneously, the inlet QF could be formed at the inlet of the experimental section. It plays significant role for low-pressure cases and decreasing roles with the increase of pressure. In addition, another possibility is the effects of inlet QF would be reduced by the corner of the experimental section near the inlet.

Traditionally, QF propagates from the inlet to the outlet of the experimental section for transport pipe, and most correlations are independent on this characteristic [7]. However, recently, experimental studies on exit-contracted pipe show that the quenching front forms in the central length of the horizontal pipe [29]. In the present study, both inlet QF and outlet QF are found. This is different from the previous studies, in the transport pipe [7] or horizontal exit-contracted pipe [29].

4. Film Boiling Heat Transfer and the Leidenfrost Point

In the present section, film boiling heat transfer, liquid rewetting, and LFP would be discussed for $L_{se} = 0.5$, 0.75 and 1 m. This is primary because these cross-sections are set on the vertical section, and the LFPs of them are primary controlled by the exit QF, at least for lower and medium pressure cases.

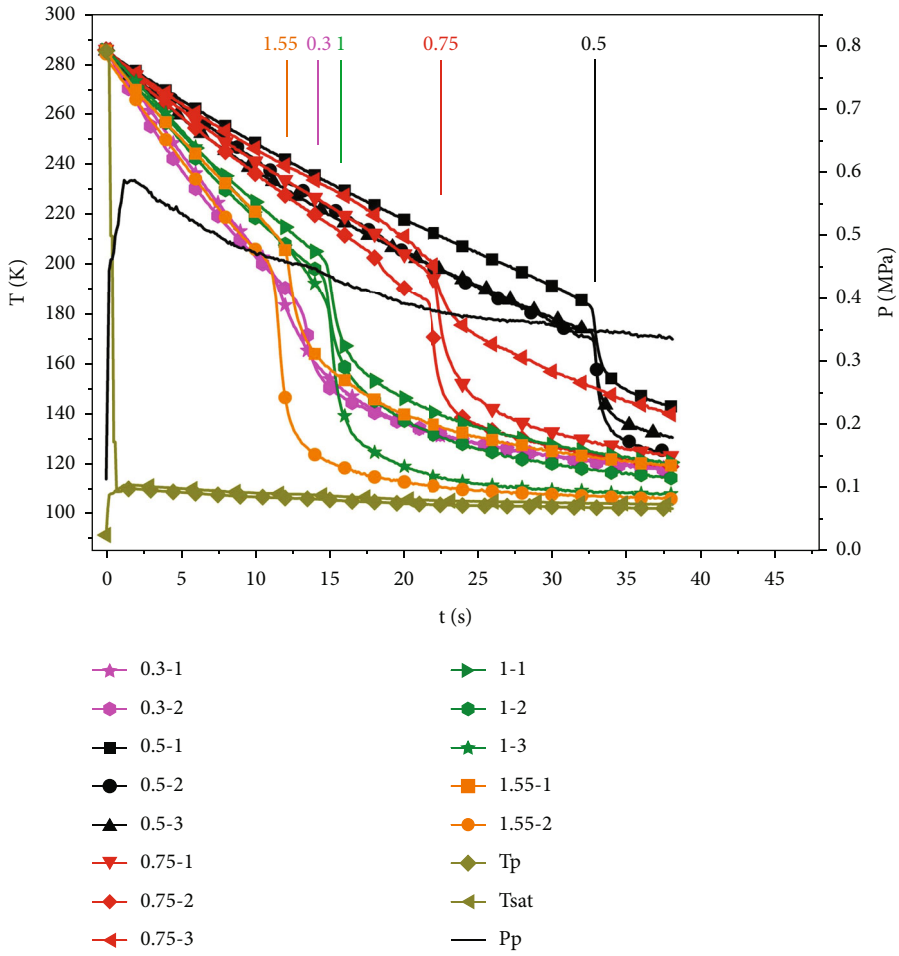

Figure 6: Tested data curves for Exp. 1 (0.45 kg/s, $P_{ss} = 0.328$ MPa).

4.1. Basic Effect of A_{inj}. The experimental ΔT_{LFP}, q_{LFP}, and h_{LFP} versus A_{inj} could be shown in Figure 10–12, respectively. It shows that, basically, with the decrease of A_{inj}, both q_{LFP} and h_{LFP} show the increasing manner (except some individual cases). On the other hand, with the decrease of A_{inj}, approximately, ΔT_{LFP} shows the increase manner for $L_{se} = 0.5$ m, the decrease manner for $L_{se} = 0.75$ m, and increase-decrease manner for $L_{se} = 1$ m. This is similar with those indicated in reference [29].

4.2. Evaluation of the Previous Correlations. Leidenfrost point (LFP), on which the liquid rewets the pipe wall, is known as the transition point from film boiling to transition boiling. This point is always identified as the point with the minimum heat flux. Historically, based on the flow instability theories, Zuber et al. [32] improved the basic correlation on q_{LFP} as shown in Equation (2) ($C_1 = 0.09$). After that, Berenson [33] approved Equation (3) ($C_2 = 0.425$) to evaluate h_{FB}, the heat transfer coefficient on film boiling, and suggested Equation (4) ($C_{LFP} = 0.127$) on LFP to evaluate ΔT_{LFP} based on basic heat transfer equation, Equation (6). After that, most correlations on q_{LFP} and ΔT_{LFP} for both pool boiling and flow boiling were based on these 2 equations. In the previous studies, ΔT_{LFP} and q_{LFP} were tried to be correlated. In this way, Equation (4) and Equation (2) were applied to predict ΔT_{LFP} and q_{LFP}, respectively, for horizontal exit-contracted pipe [8, 29].

$$q_{LFP} = C_1 \rho_v H_{vl} \left(\frac{\sigma_{vl} g (\rho_l - \rho_v)}{(\rho_l + \rho_v)^2} \right)^{0.25}, \tag{2}$$

$$h_{FB} = C_2 \left[\frac{k_v^3 H_{vl} \rho_v g (\rho_l - \rho_v)}{\mu_v \Delta T_i \sqrt{\sigma_{vl} / g (\rho_l - \rho_v)}} \right]^{0.25}, \tag{3}$$

$$\Delta T_{LFP} = T_{LFP} - T_{sat} = C_{LFP} \cdot E_{LFP}, \tag{4}$$

$$E_{LFP} = \frac{\rho_v H_{vl}}{k_v} \left(\frac{g (\rho_l - \rho_v)}{\rho_l + \rho_v} \right)^{2/3} \left(\frac{\sigma_{vl}}{g (\rho_l - \rho_v)} \right)^{1/2} \left(\frac{\mu_v}{g (\rho_l - \rho_v)} \right)^{1/3}, \tag{5}$$

$$q_i = h_i \Delta T_i. \tag{6}$$

According to Equation (4), in the present study, for vertical experimental section, ΔT_{LFP} could be plotted versus E_{LFP} in Figure 13, where C_{LFP} could be correlated to be 0.0576 and produces the MAE of 16.62%. As shown in the

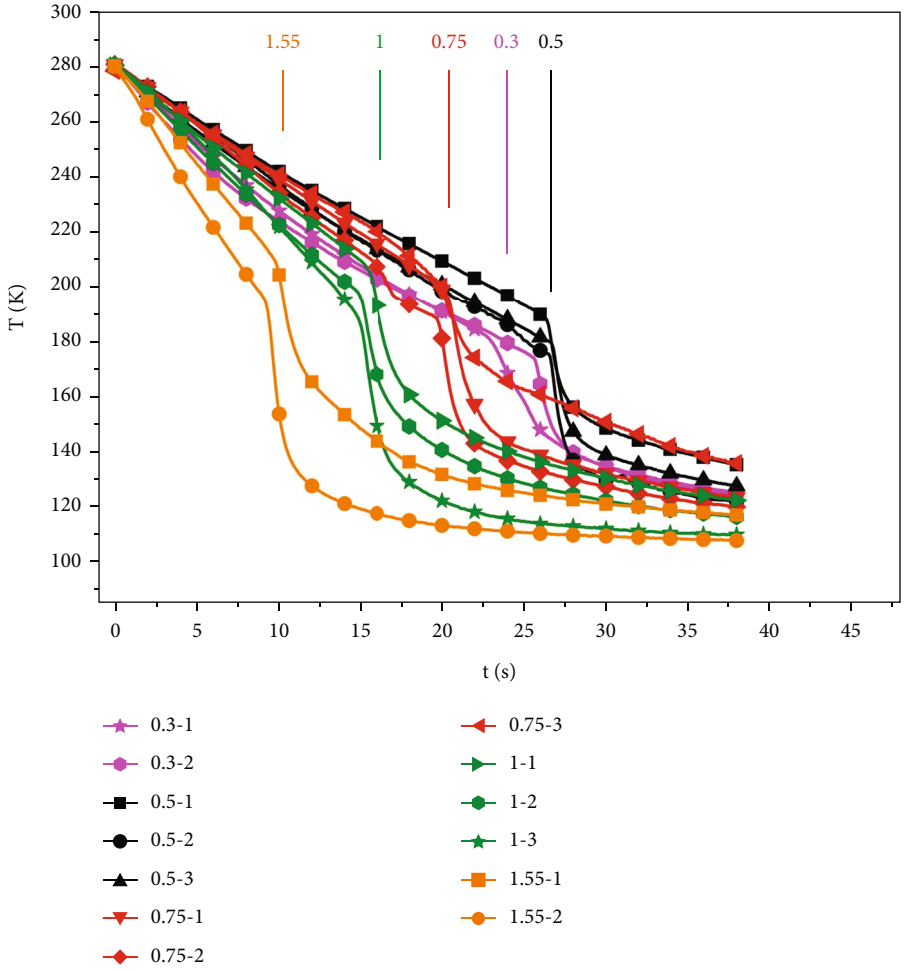

Figure 7: Tested data curves for Exp. 2 (0.444 kg/s, $P_{ss} = 0.41$ MPa).

figure, the point distribution and constant C_{LFP} do not show significant differences from the previous studies [29]. It shows that with the increase of A_{inj}, ΔT_{LFP} shows the overall increasing manner for $L_{se} = 0.5$ m and overall decreasing manner for other L_{se}. This indicates the similar difficulties on correlation, which has been discussed in the previous studies in horizontal pipes [29].

On the other hand, Zuber's correlation, Equation (2), indicates that on LFP, vapor was not produced rapidly enough to lift the interface as rapidly as it would normally collapse [34]. In this way, q_{LFP} in the present study could be correlated by this equation as shown in Figure 14, where the constant C_1 and MAE could be listed in Table 4. Generally speaking, as shown in Equation (2), the effects of fluid properties could be represented by the items in the abscissa of Figure 14, and the effects of circumferential position and L_{se} could be represented by the variable parameter C_1, which has been correlated for every point. Obviously, it is not a general correlation. However, in the current stage, this equation is important to set up the basic outline for the following investigations.

As shown in Figure 14, basically, Equation (2) could produce reliable predictions on q_{LFP} for $L_{se} = 0.5$ and 0.75 m relatively. However, for $L_{se} = 1$ m, with the increase of $\rho_v H_{vl}(\sigma_{vl} g(\rho_l - \rho_v)/(\rho_l + \rho_v)^2)^{0.25}$, q_{LFP} shows the decreasing-increasing manner. Thus, from the view of point of correlation, Equation (2) could be used to produce q_{LFP} for $L_{se} = 1$ m only on higher pressure (e.g., $P_{ss} \geq 0.4$ MPa). In this way, C_1 items listed in Table 4 for $L_{se} = 1$ m were correlated for Exp. 2~4.

4.3. Correlations on h_{LFP}. By the present set of data, h_{LFP} could be correlated by Equation (3) as shown in Figure 15, where the constant C_2 could be listed in Table 4. Basically, with the increase of pressure, the 2nd item of the right side of Equation (3) keeps increasing constantly, which is consistent to the experimental h_{LFP} data.

4.4. Primary Effect Factors. According to Carbajo [35], liquid rewetting involves the effects of pressure, liquid subcooling, liquid and solid properties, surface conditions, and flow rate. However, in the present study, throughout all of the tests, only pressure shows the obvious variations. On the other

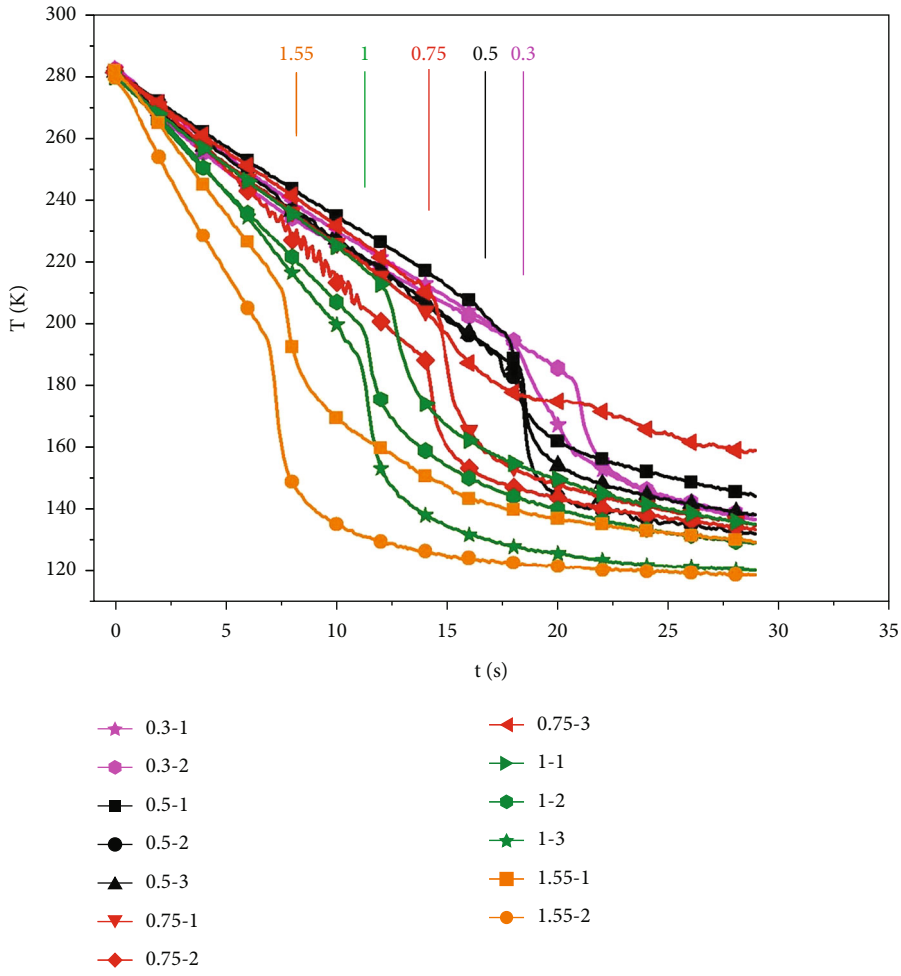

Figure 8: Tested data curves for Exp. 3 (0.438 kg/s, P_{ss} = 0.77 MPa).

Table 3: Statistical t_{LFP}/t_{CHF} data (unit: s).

Position	Exp. 1	Exp. 2	Exp. 3	Exp. 4
0.3-1	10/11.9	22/23.6	13/18.9	8/11.7
0.3-2	11/13.7	22/25.9	16/21.3	9/13
0.5-1	29/33.1	23/26.7	12/18.3	6/9.1
0.5-2	28/33.2	22/26.8	12/18.7	5/9.5
0.5-3	30/33.2	25/27	12/18.7	5/8.7
0.75-1	18/22.6	17/20.7	10/15.2	6/9.6
0.75-2	15/22.3	14/20.1	10/14.5	6/8.8
0.75-3	16/22.4	15/20.2	10/14.8	6/9.5
1-1	14/15.4	13/16	8/13	6/9.2
1-2	14/15.2	14/15.3	8/11.7	6/8
1-3	11/15.4	13/15.3	8/11.7	5/8
1.55-1	10/12.6	8/10.2	6/8	4/5.1
1.55-2	10/11.8	8/9.6	5/7.5	4/4.7

hand, L_{se} and circumferential positions are obviously different for these points. In this way, the effects of pressure, L_{se}, and circumferential positions would be discussed in the present section.

4.4.1. The Effects of A_{inj} or Pressure. The present series of tests are with the same flow rate. Thus, the effects of A_{inj} in the present study indicates the effects of pressure only. On the film boiling section, with the decrease of A_{inj} (increase of pressure), h_{FB} keeps increasing because δ_{FB} keeps almost constant and k_v keeps increasing as shown in Equation (7) [29].

$$h_{FB} = \frac{k_v}{\delta_{FB}}. \tag{7}$$

In this way, with the increase of A_{inj}, the slope of T_i decreasing increases for every point, and chill-down period (t_{LFP}) would be shortened as well. As a result, both heat flux and heat transfer coefficient would be enhanced on film boiling section, which produces the overall increasing q_{LFP} and h_{LFP} for every point.

These principles are very similar with those tendencies in horizontal exit-contracted pipe [29].

4.4.2. The Effects of L_{se}. Traditionally, h_{LFP} decreases with the increase of L_{se} according to the existing correlations [7]. However, in the present study, experimental data do not

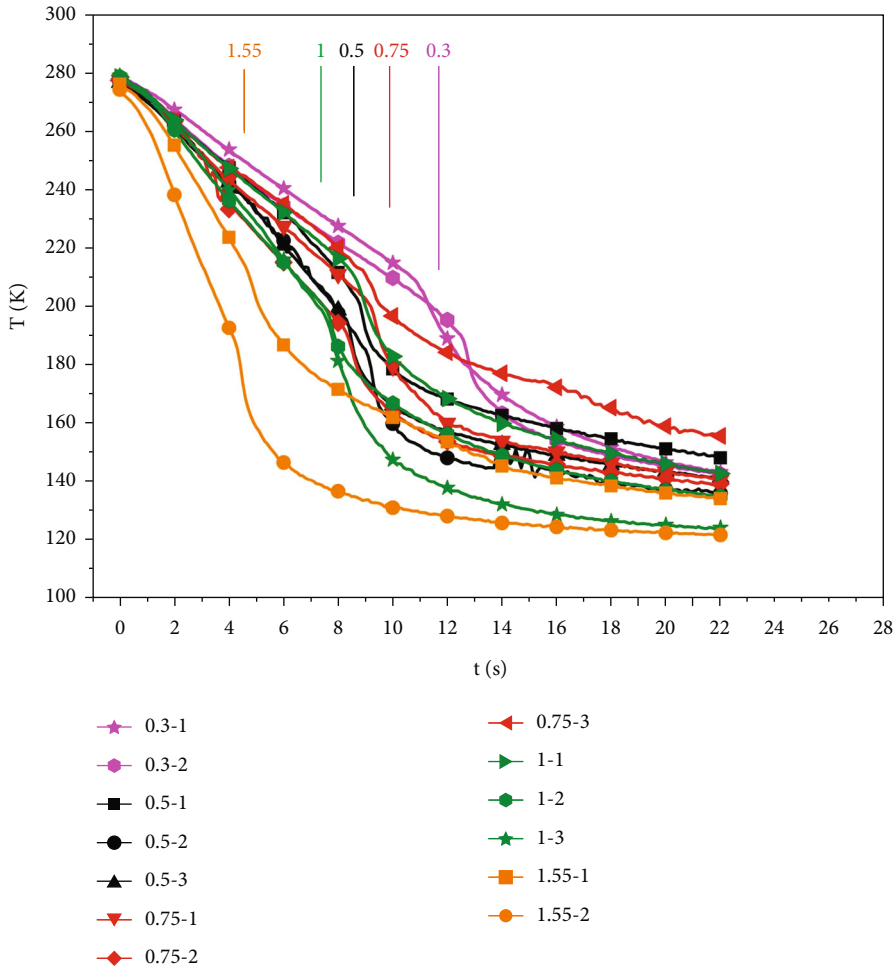

Figure 9: Tested data curves for Exp. 4 (0.426 kg/s, $P_{ss} = 1.325$ MPa).

show the similar tendency. Comparison between Figures 14 and 15 shows that, for a certain test, both q_{LFP} and h_{LFP} increase with the increase of L_{se}, which is contrary to that in transport pipe [7]. Comparison among transport pipe [7], horizontal exit-contracted pipe [29], and vertical exit-contracted pipe indicates that the effects of L_{se} traditionally concerned are essentially more like the effects of L_{qf}, distance from the present point to the QF formation point. In this way, experimental results in reference [29] and in the present study could be explained well. Thus, it is necessary to denote that from the view of point of pipe length, L_{qf} plays the significant role on LFP instead of L_{se}.

In general, for a certain test, along the directions of QF propagation, t_{LFP} shows the increasing manner, compared to that q_{LFP} and h_{LFP} show the decreasing manner. This characteristic plays significant roles on the LFP. This indicates the basic principle, longer L_{qf} is corresponding to greater t_{LFP}, lower q_{LFP} and h_{LFP}. This principle is always the case independent on L_{se} and the dominant QF, even for $L_{se} = 0.3$ m, on which even the LFP is controlled by various QF.

For a certain L_{se}, with the increase of A_{inj}, t_{LFP} shows the decreasing manner, and q_{LFP} and h_{LFP} show the increasing manner. This indicates that with the increase of pressure, both h_{FB} and M (magnitude of instable waves) undergo corresponding increase. According to results in horizontal exit-contracted pipe [29], LFP is controlled by the competition between heat transfer and the increase of M. However, according to the present study, QF propagation also plays a significant role on. In the present study, for Exp. 1~3, QF propagation could be well tracked according to the experimental data, which indicates that the latter one is the dominant factor. However, for Exp. 4, LFP happens almost simultaneously on $L_{se} = 0.5$, 0.75, and 1 m, which indicates that the former is the dominant factor in this case.

Another key point is where is the QFs formed. In the present study, both inlet QF and exit QF are identified. Analysis indicates that QF formation is controlled by the fill process of the cryogenic fluid in the exit-contracted pipe.

4.4.3. The Effects of Circumferential Position. As shown in Table 3, for every L_{se}, t_{LFP} values for circumferential position (1, West; 2, South; 3, East) are quite similar to each other. This indicates the propagation of QF circumferentially also plays significant role. This is similar with those in horizontal exit-contracted pipe [29]. However, traditionally,

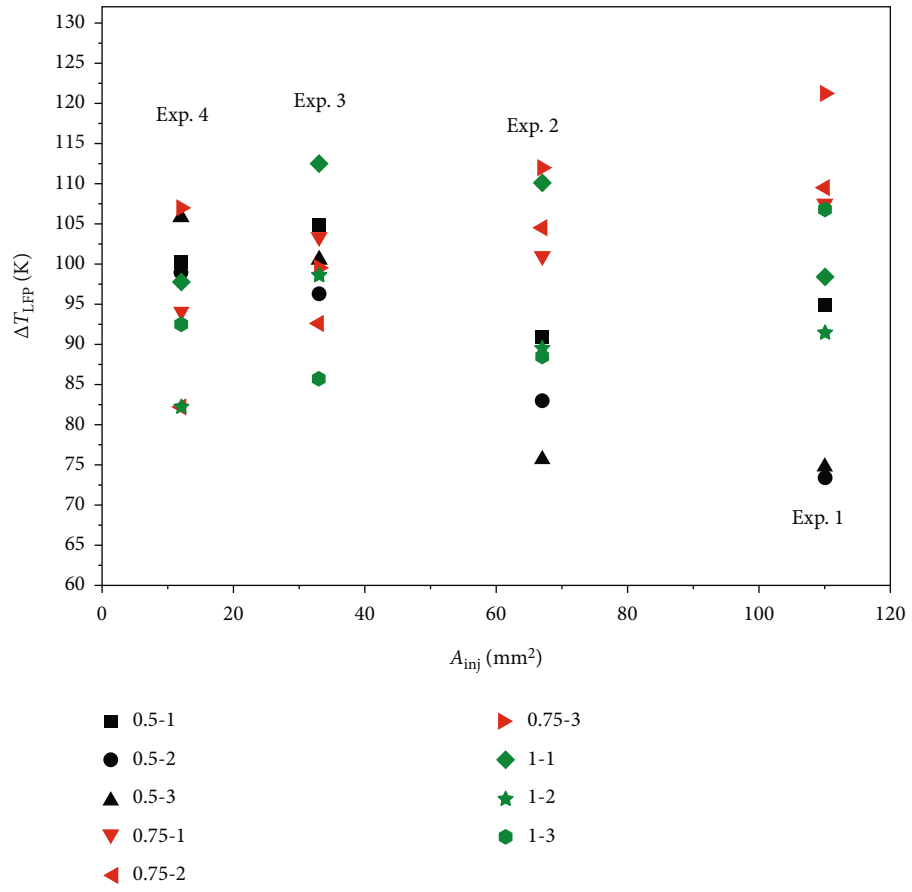

Figure 10: Experimental ΔT_{LFP} versus A_{inj}.

circumferential position plays ignorable role in the vertical transport pipe [7]. In the present study, vertical section (L_{se} = 1, 0.75, and 0.5 m), as shown in Table 4, could produce around 50% variation on h_{LFP} and q_{LFP} and q_{CHF} for L_{se} = 1 and 0.75 m and 30% for L_{se} = 0.5 m.

In this way, for a certain L_{se}, h_{FB} always dominates the decrease of T_i on points 1~3. After that, once one of them gets to LFP, boiling transitions would happen immediately on other two points, which produces the h_{FB} at that time as h_{LFP}. In another word, on the same L_{se} cross-section, various points are with the similar t_{LFP}.

In this way, three points, 0.5-2, 0.75-2, and 1-3 are the dominant points for L_{se} = 0.5, 0.75, and 1 m, respectively, and determines the t_{LFP} point on the present section in the present study. For other points (dominated points), during the chill-down process, q_i and T_i keep decreasing, and h_{FB} keeps increasing. Once LFP happens at t_{LFP} on the dominant point on the same section, liquid rewetting would happen on the dominated points. Thus, q_i, T_i, and h_{FB} at that time would be identified as q_{LFP}, T_{LFP}, and h_{LFP}.

This implies that on a certain L_{se} cross-section, the liquid rewetting mechanism for the dominant point is different from that for the dominated points. For the dominant point, liquid rewetting is more likely to be controlled by flow instability, which is similar with that on pool boiling or flow boiling. According to the series of data, this process is dominated by the QF propagation axially. However, for the dominated points, liquid rewetting is controlled by both the dominant point and the local heat transfer. This process is dominated by the QF propagation circumferentially.

The difference between the dominant point and dominated points could be also found in the horizontal exit-contracted pipe. Obviously, because of the gravity, the dominant point is the bottom point for horizontal pipe [29]. However, for the vertical pipe, the effect of gravity could be ignored. According to Carbajo [35], liquid rewetting involves the effects of pressure, liquid subcooling, liquid and solid properties, surface conditions, and flow rate. In this way, on the same L_{se} cross-section, this sort of difference between the dominant point and dominated points is probably caused by the inner surface conditions.

4.4.4. Summary on the Basic Effect Factors. As discussed above, the effects of pressure, L_{se}, and circumferential position could be summarized and concluded as follows.

(1) For a certain point, the increase of A_{inj} produces overall increasing q_{LFP} and h_{LFP} and deceasing t_{LFP}

(2) With the increase of L_{qf}, overall decreasing q_{LFP} and h_{LFP} and increasing t_{LFP} could be obtained

(3) Because of the propagation of QF circumferentially, on a certain L_{se} (cross-section), there are both dominant point and dominated points, which are

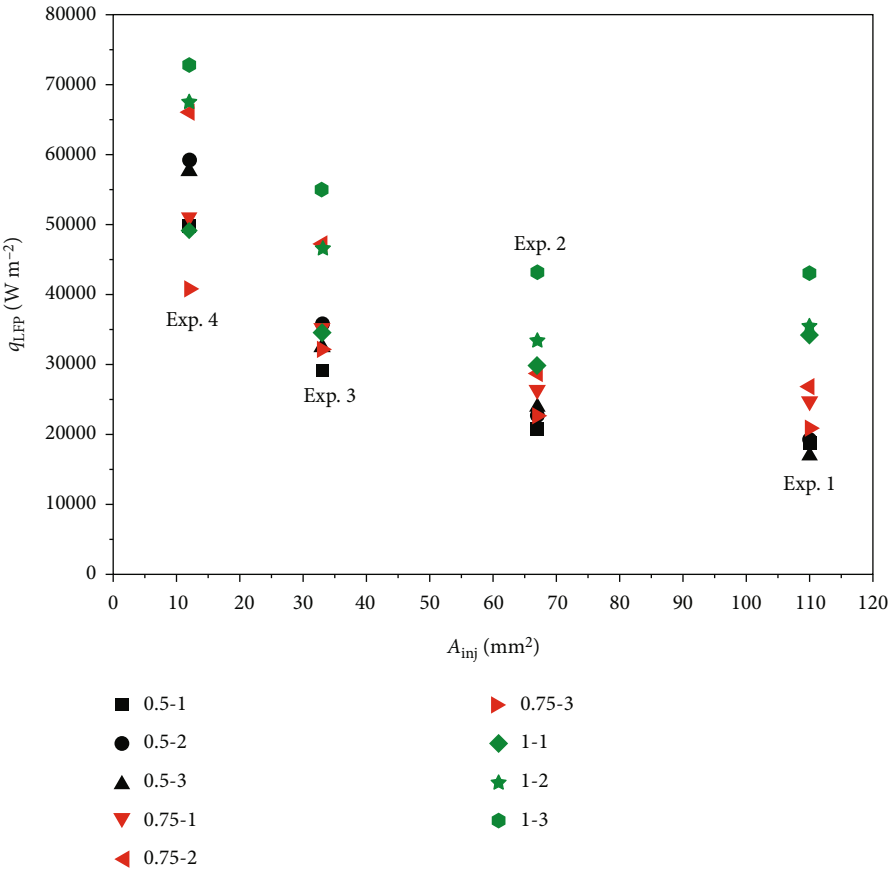

Figure 11: Experimental q_{LFP} versus A_{inj}.

controlled by flow instability and both dominant point and h_{FB} and, respectively. In the present study, 0.5-2, 0.75-2, and 1-3 are the dominant points for these sections, respectively.

4.5. Discussions

4.5.1. Correlations on the Dominant Points. From the view of point of correlation, all of these factors should be involved. For three dominant points, 0.5-2, 0.75-2, and 1-3, on which liquid rewetting is controlled by flow instability. According to Equation (2) and Table 4, C_1 for them are correlated to be 0.0643, 0.0748, and 0.086, respectively. It shows that C_1 increases linearly with the increase of L_{se} (decrease of L_{qf}). In this way, based on Equation (2), q_{LFP} on the dominant points for $L_{se} = 0.5$, 0.75, and 1 m could be correlated by Equation (8). This correlation could be approved for dominant points in vertical section.

$$q_{LFP} = (0.0425 + 0.0434L_{se})\rho_v H_{vl}\left(\frac{\sigma_{vl} g(\rho_l - \rho_v)}{(\rho_l + \rho_v)^2}\right)^{0.25}. \quad (8)$$

As discussed above, in the present study, q_{LFP} decreases with the decrease of L_{se} for $L_{se} = 0.5$ m and its downstream. In addition, on 1.55-2, the dominant point on $L_{se} = 1.55$ m, and the horizontal section, C_1 was correlated to be 0.1335, which has not been given above. This indicates the C_1 values along the QF propagation, from 0.1335 ($L_{se} = 1.55$ m) to 0.086 ($L_{se} = 1$ m), 0.0748 ($L_{se} = 0.75$ m), and finally, 0.0643 ($L_{se} = 0.5$ m). These series of values are consistent to the literature data, in which C_1 was correlated to be 0.09 [32] for room-temperature fluid in pool boiling. At first, the deviation of C_1 between the present study and reference [32] is mainly caused by the variations between the fill-in flow in the exit-contracted pipe and pool boiling. On the other hand, the decrease of C_1 along the reverse direction of the flow in the experimental section pipe indicates the special characteristics of flow in the exit-contracted pipe.

Similarly, according to Equation (3), C_2 for 0.5-2, 0.75-2, and 1-3 are correlated to be 0.573, 0.7139, and 0.8264, respectively. Similar with q_{LFP}, h_{LFP} on the dominant points for $L_{se} = 0.5$, 0.75, and 1 m could be correlated by Equation (9). This series of data is consistent to the literature data, in which C_2 was correlated to be 0.425 [33] for room-temperature fluid in pool boiling.

$$h_{FB} = (0.324 + 0.5068L_{se})\left[\frac{k_v^3 H_{vl}\rho_v g(\rho_l - \rho_v)}{\mu_v \Delta T_i \sqrt{\sigma_{vl}/g(\rho_l - \rho_v)}}\right]^{0.25}. \quad (9)$$

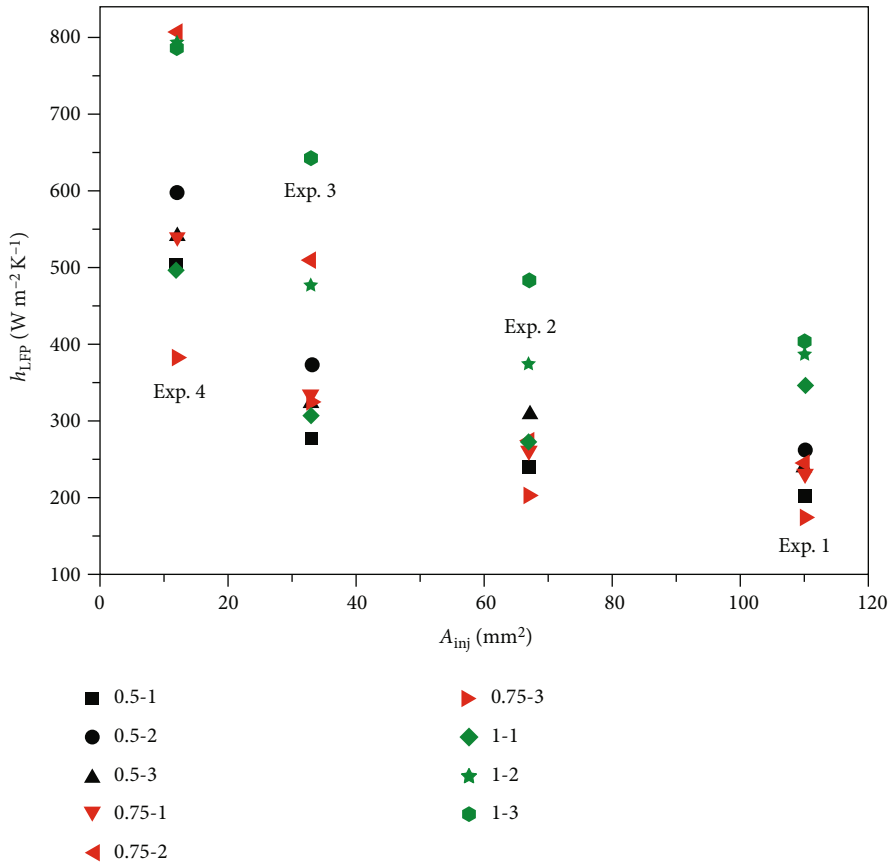

Figure 12: Experimental h_{LFP} versus A_{inj}.

Compared to the literature data from room-temperature fluid in pool boiling, dominant points in the vertical section are with lower q_{LFP}, lower ΔT_{LFP}, and higher h_{LFP}. Basically, this sort of differences is mainly caused by the variations on the system pressure and flow condition. On the other hand, the similarity on C_1 and C_2 between for exit-contracted pipe and pool boiling indicates that flow instability is the primary dominant factor, and L_{se} also plays a certain role for the dominant points on the present vertical pipe.

4.5.2. Correlations on the Dominated Points. For the dominated points, Equations (2) and (3) with constants listed in Table 4 could be suggested in the current stage. It has to be denoted that on this sort of points, liquid rewetting is not caused by local flow instability on this sort of points. On the contrary, the local instable wave has not been developed adequately. Result indicates that at t_{LFP}, liquid rewetting happens on the dominant point on the current cross-section. Almost simultaneously, all of this cross-section is rewetted by the liquid as a result of QF propagation circumferentially from the dominant point. In this way, on the dominated points, as a result of being rewetted, q_i, h_i, and T_i at t_{LFP} have to be denoted as parameters on LFP.

4.5.3. Correlation Approach and Correlation Formats. In the previous studies, q_{LFP} and ΔT_{LFP} were tried to be correlated, and h_{LFP} has not been tried to be correlated before [8]. In the present study, q_{LFP} and h_{LFP} (instead of ΔT_{LFP}) are correlated. This is the new correlation approach. In the recent studies, correlation formats for Equations (2)–(4) were approved to correlate q_{LFP}, h_{LFP}, and ΔT_{LFP}, respectively. The primary items in these equations could be plotted versus pressure as shown in Figure 16.

For ΔT_{LFP}, as discussed above, there are two difficulties on reliable correlation, which determines it would not be considered to be correlated in the current stage. The first one is, as shown in Figures 13 and 16, parameter combination, with the increase of pressure from ambient to around 2.5 MPa, E_{LFP} in Equation (4) shows the increasing-decreasing manner, which indicates that it could not represent the effects of pressure. On the other hand, with the increase of pressure, the variations of ΔT_{LFP} show different manners for various L_{se}. The primary reason is E_{LFP} and Equation (4) are approved for pool boiling in ambient-pressure, which could not be applied in high pressure cases.

For both dominant point and dominated points, q_{LFP} and h_{LFP} are well correlated on the vertical section. This is primarily because the basic effects including pressure, L_{se}, and circumferential position are well involved. At first, for dealing with the effect of circumferential position, dominant points were identified from dominated points, and they were correlated apart from each other. On the other hand, the effects of pressure and L_{se} are involved well in Equations

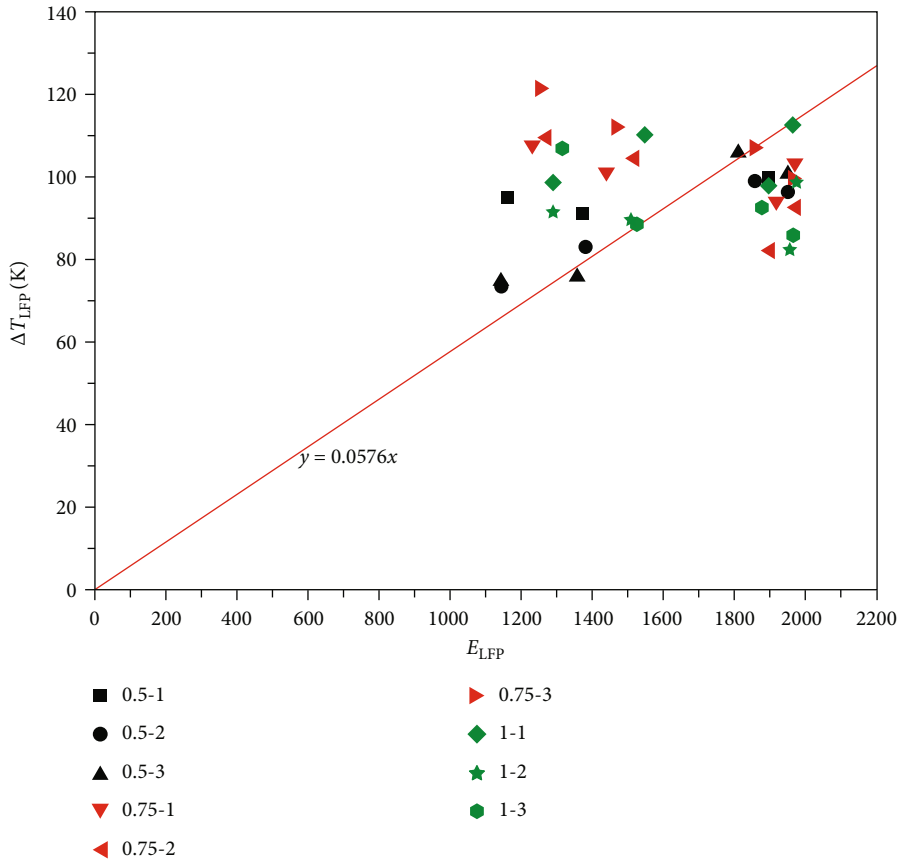

Figure 13: Experimental ΔT_{LFP} versus E_{LFP}.

(2)–(3) and Equations (8)–(9). Especially, as shown in Figure 16, in the effective LFP pressure range from ambient to around 2.5 MPa [8], the primary items in both Equations (2) and (3) (as well as (8) and (9)) increase consistently with the increase of pressure, which indicates that these equations could represent the effect of pressure well.

5. New Correlation on q_{CHF} and Discussions on the Critical Heat Flux Point

5.1. Basic Effect of A_{inj}. Figure 17–19 shows the basic experimental data, where ΔT_{CHF}, q_{CHF}, and h_{CHF} are plotted versus A_{inj}, respectively. With the decrease of A_{inj}, ΔT_{CHF} shows the overall decreasing manner, and both q_{CHF} and h_{CHF} show the overall increasing-decreasing manner, primarily. This is similar with the results in the previous study for horizontal exit-contracted pipe [29].

5.2. Evaluations on the Previous Correlations. In the previous studies, Equation (10) from transport pipe was recommended by the present authors to predict ΔT_{CHF} for horizontal exit-contracted pipe [8, 28]. However, this equation was demonstrated to produce great deviations when predicting the previous set of data, where more detailed T_o was measured [29].

$$\Delta T_{CHF} = T_{CHF} - T_{sat} = 1.345 \times 10^{-5} B, \tag{10}$$

$$B = H_{vl}\rho_v \left[\frac{g\sigma_{vl}(\rho_l - \rho_v)}{\rho_v^2}\right]^{0.25}. \tag{11}$$

Figure 20 plots the experimental ΔT_{CHF} versus parameter B in the present study. These figures show very similar with Figure 13. In this way, similar difficulties on correlations with LFP could be found, which could be discussed next.

In the previous study, new correlations on q_{CHF} have been approved for horizontal exit-contraction pipe [29] as shown in Equation (12) (Equation (13) is another version). This equation involves the effects of L_{se} and circumferential by constant C_3, the effects of u_l by $u_l^{-0.1149}$, and the effects of fluid properties by other items. In the present study, q_{CHF} values could be correlated by Equation (13) as shown in Figure 21, where the constant C_3 could be listed in Table 4, which indicates correlation equation approved from the horizontal exit-contracted pipe would be used in the present vertical exit-contracted pipe.

$$q_{CHF} = C_3 u_l^{0.1149} \rho_v^{0.1262} H_{vl}((\rho_l\text{-}\rho_v)\sigma_{vl})^{0.1667} \rho_l^{0.5405}, \tag{12}$$

$$\frac{q_{CHF}}{\rho_v H_{vl} u_l} = C_3 \left(\frac{\rho_l}{\rho_v u_l^{0.25}}\right)^{0.8738} \left(\frac{\sigma_{vl}}{\rho_l u_l^2 D_{bu}}\right)^{0.3333}. \tag{13}$$

5.3. New Correlation on h_{CHF}. For LFP, both q_{LFP} and h_{LFP} could be correlated by the existing correlation format. In this

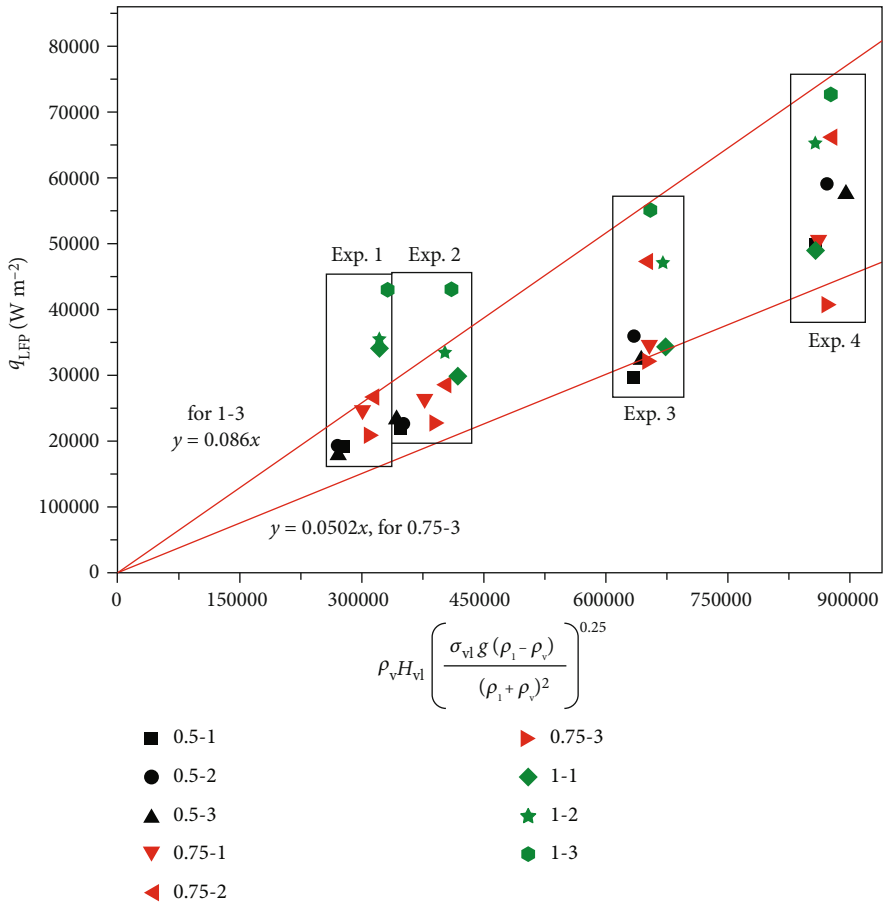

Figure 14: Correlation on q_{LFP} by Equation (2).

Table 4: Constants for every point in Equations (2), (3) and (11), respectively.

Point	Constant C_1	MAE (%)	Constant C_2	MAE (%)	C_3	MAE (%)
0.5-1	0.0555	14.28	0.4828	10.16	0.00703	11.24
0.5-2	0.0643	7.12	0.573	6.29	0.00982	4.06
0.5-3	0.0607	11.20	0.5236	6.26	0.00828	4.06
0.75-1	0.0597	14.05	0.5281	6.40	0.00769	4.00
0.75-2	0.0748	5.45	0.7139	13.60	0.00835	4.19
0.75-3	0.0502	12.26	0.4121	5.72	0.00428	13.65
1-1	0.0572*	10.49	0.4967*	7.09	0.00683	1.53
1-2	0.0749*	6.05	0.7384*	8.74	0.00725	1.63
1-3	0.086*	8.02	0.8264	4.47	0.00994	5.57

*, except Exp. 1.

way, ΔT_{LFP} could be obtained correspondingly. This approach could be adopted when discussing CHF point. In this way, the possibility of correlating h_{CHF} should be evaluated well. Basically, a number of correlations on heat transfer coefficient for nucleate boiling were approved in the previous studies.

Forster-Zuber correlation was applied widely to predict heat transfer for nucleate boiling in pool [36]. In this correlation, the variation between saturation pressure on T_i (temperature inner wall), P_{si}, and P_p (pressure in the pipe) was assumed to vary linearly versus subcooling ΔT_i, $(T_i - T_{sat})$, as Equation (14) shows. In this way, heat transfer coefficient could be predicted by Equation (15), where constant C_4 indicates $C \cdot k_{FZ}{}^{0.75}$. Experimental results show that in the present study, most T_{CHF} values are higher than the critical temperature, which gives the constant P_{si} values. Of course, another possibility is this series of equations were approved for low-pressure cases. Nevertheless, this reduces the role of k_{FZ} as shown in Equation (14), and the effects of k_{FZ} could be just represented by C_4 in Equation (15).

$$P_{si} - P_p = k_{FZ} \Delta T_i, \tag{14}$$

$$h_{NB} = C_4 \frac{\rho_l^{0.5} c_{pl}^{0.125} k_l^{1.125} \mathrm{Pr}_l^{0.333}}{\rho_v^{0.25} H_{vl}^{0.25} \mu_{vl}^{0.625} \sigma_{vl}^{0.5}} \Delta T_i. \tag{15}$$

Comparison shows that, as shown in Equation (15), for CHF, with the increase of pressure, $\rho_l^{0.5} c_{pl}^{0.125} k_l^{1.125} \mathrm{Pr}_l^{0.333} / \rho_v^{0.25} H_{vl}^{0.25} \mu_{vl}^{0.625} \sigma_{vl}^{0.5}$ shows the overall increasing manner;

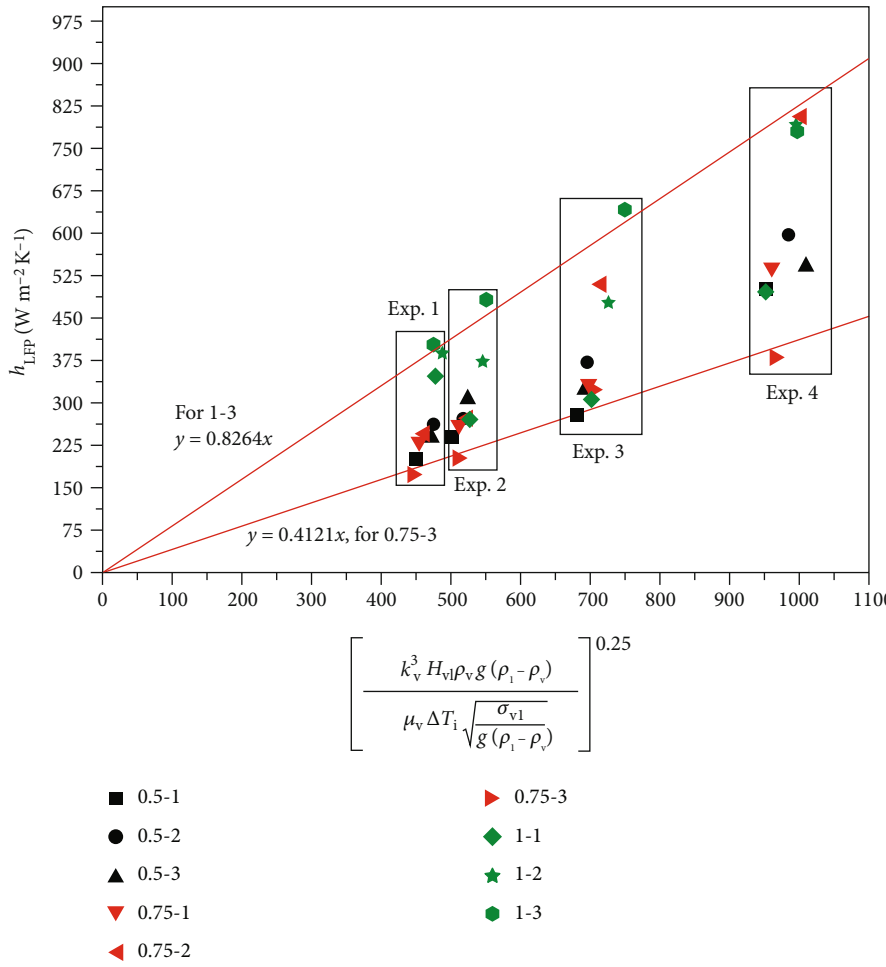

Figure 15: Correlation on h_{LFP} by Equation (3).

however, ΔT_{CHF} shows the contrary manner, which produces extra difficulties on correlation. In this way, the parameter combination could be revised as Equation (16) shows, and the present set of data could be plotted as shown in Figure 22. It shows that h_{CHF} could be correlated by Equation (17), which produces the overall MAE of 2.3% and the max deviation 13.4%. The deviation bar has been plotted in the figure, where the red lines show the ±2% deviation on the present figure, and ±17.9% for the h_{CHF} data.

$$h_{CHF} = C_4 \left(\frac{\rho_v^{0.25} H_{vl}^{0.25} \mu_{vl}^{0.625} \sigma_{vl}^{0.5}}{\rho_l^{0.5} c_{pl}^{0.125} k_l^{1.125} \mathrm{Pr}_l^{0.333}} \Delta T_{CHF} \right)^N, \quad (16)$$

$$h_{CHF} = 19511.9 \left(\frac{\rho_v^{0.25} H_{vl}^{0.25} \mu_{vl}^{0.625} \sigma_{vl}^{0.5}}{\rho_l^{0.5} c_{pl}^{0.125} k_l^{1.125} \mathrm{Pr}_l^{0.333}} \Delta T_{CHF} \right)^{0.6588}. \quad (17)$$

5.4. Primary Effect Factors. Similar with LFP, the effects of pressure, L_{se}, and circumferential positions would be discussed in the present section.

5.4.1. The Effect of A_{inj} or Pressure. CHF point could be recorded in a wide range from the ambient-pressure to around 4.0 MPa. Basically, as shown in Section 5.1, in this pressure range, with the decrease of A_{inj} (increase of pressure), primarily, q_{CHF}, ΔT_{CHF}, and h_{CHF} show the overall constant or increase-decrease manner. These factors are consistent to those approved in the previous studies [8, 29].

5.4.2. The Effects of L_{se}. For LFP, at least q_{LFP} shows the obviously decreasing manner with the increase of L_{qf}. However, for the experimental data on q_{CHF} and h_{CHF}, the effects of L_{se} do not show the obvious regulations. In this way, correlations on these parameters do not involve L_{se}. At least, this indicates L_{se} plays ignorable roles on bubble separation.

5.4.3. The Effects of Circumferential Position. The effect of circumferential position on CHF is similar to that of LFP. As shown in Table 3, for every L_{se}, t_{CHF} values for various circumferential positions (1, West; 2, South; 3, East) are quite similar to others. This indicates that the propagation of bubble separation "front" circumferentially plays significant roles on the CHF for a certain L_{se} cross-section. In

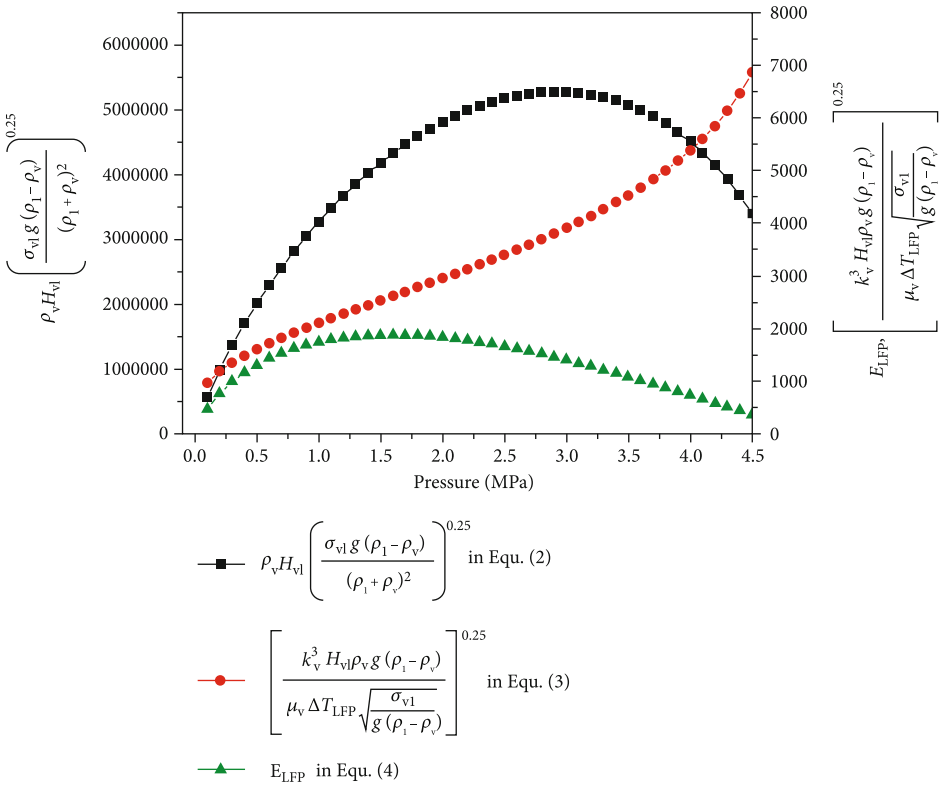

Figure 16: Parameter combinations in Equations (2)–(4) versus pressure.

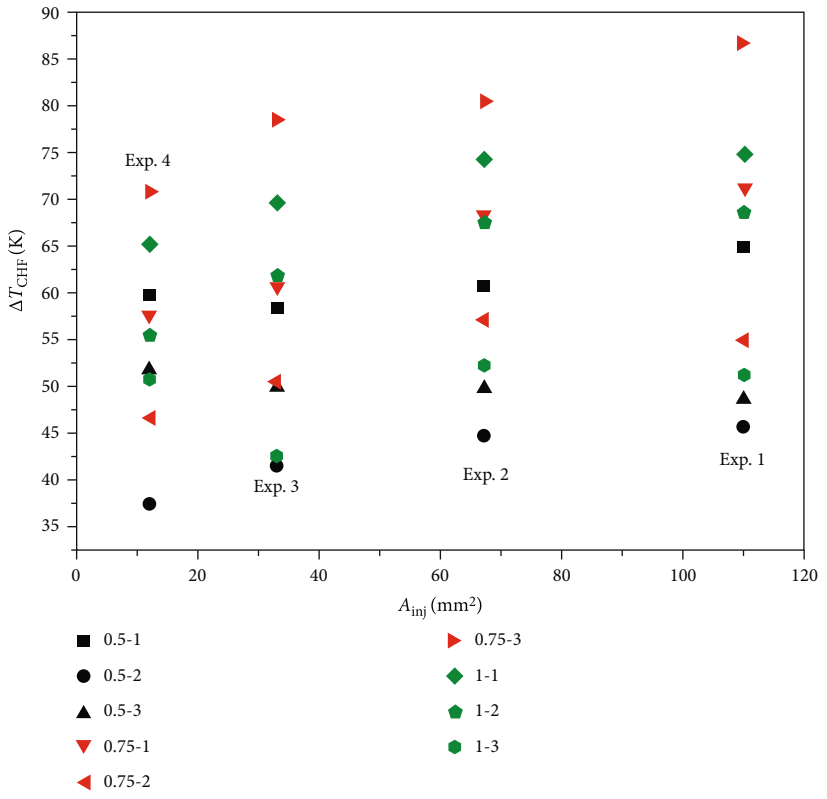

Figure 17: Experimental ΔT_{CHF} versus A_{inj}.

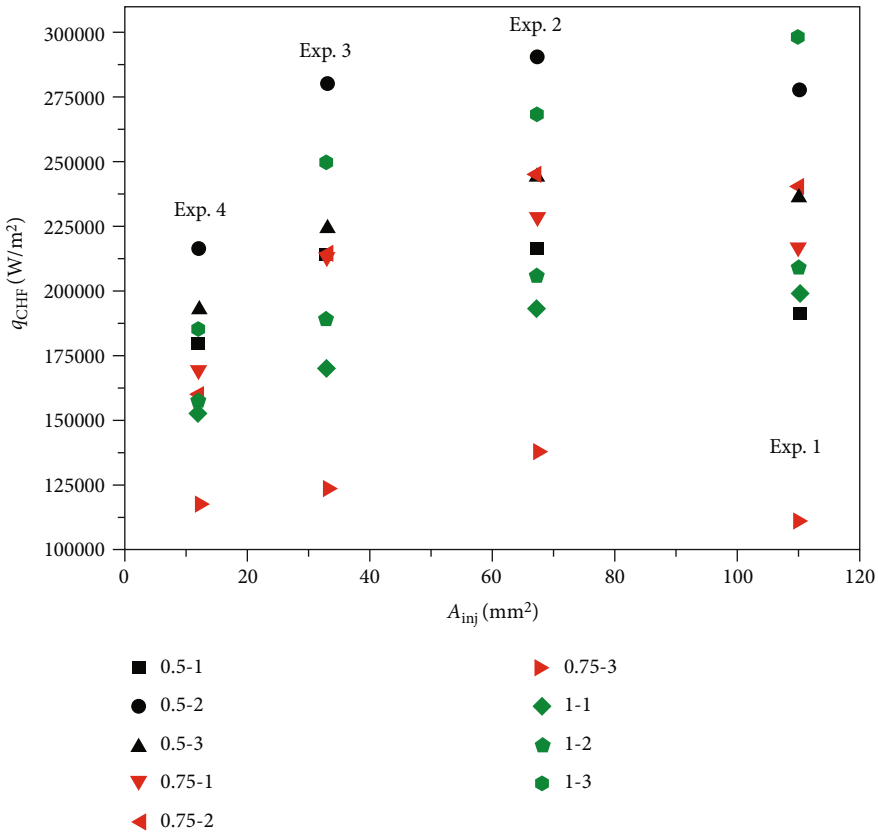

Figure 18: Experimental q_{CHF} versus A_{inj}.

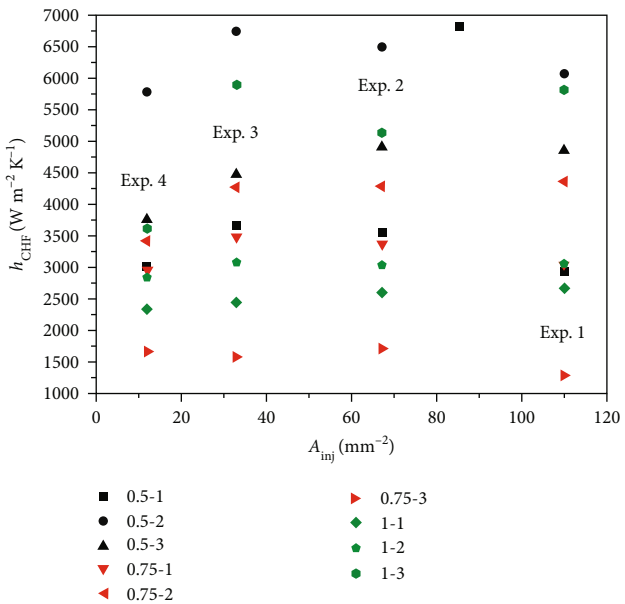

Figure 19: Experimental h_{CHF} versus A_{inj}.

addition, for a certain L_{se}, various circumferential positions are with various q_{CHF}, h_{CHF}, and T_{CHF}. This indicates that, similar with LFP, for a certain L_{se}, there are both dominant point and dominated points. As shown in Table 3, dominant points for bubble separation (CHF), 0.5-2, 0.75-2, and 1-3 are same with those for liquid rewetting (LFP). This is because on the current cross-section, T_i on the dominant point decreases prior to other points, not only on film boiling section but also on transition boiling section. In this way, T_i on the dominant point is always the lowest on the current cross-section and dominates the boiling transitions on the current cross-section.

5.4.4. Summaries on the Basic Factors. As discussed above, the effects of pressure, L_{se}, and circumferential position could be summarized and concluded as follows.

(1) For a certain point, the increase of pressure produces overall decreasing q_{CHF}, h_{CHF}, and deceasing t_{CHF}

(2) The effect of L_{se} plays ignorable roles on CHF, including q_{CHF} and h_{CHF}

(3) Similar with LFP, because of the propagation of bubble separation front circumferentially, on a certain L_{se} (cross-section), there are both dominant point and dominated points, which are controlled by flow instability and both heat transfer and the dominant points. In the present study, 0.5-2, 0.75-2, and 1-3 are the dominant points for these sections, respectively

5.5. Discussions

5.5.1. Correlation on the Dominant Points. From the view of point of correlation, the effects of both pressure and

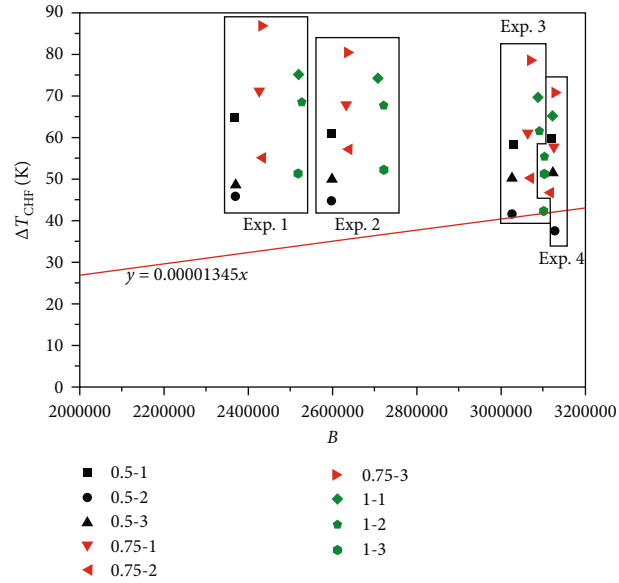

Figure 20: Experimental ΔT_{CHF} versus B.

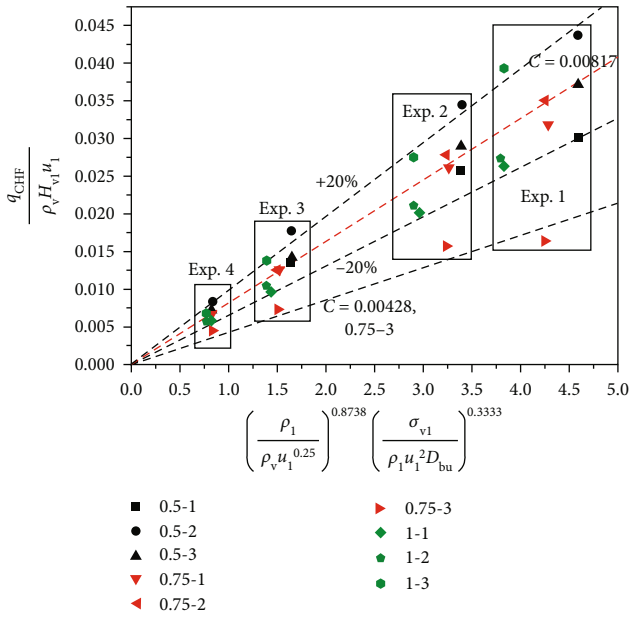

Figure 21: Correlation on q_{CHF} by Equation (12).

circumferential position should be involved. The related strategy is similar with that for LFP, by which the dominant points and dominated points would be discussed, respectively.

As shown in Equation (12) and Table 4, in the present correlation on q_{CHF}, C_3 is correlated to be 0.00982, 0.00835, and 0.00994 for dominant points, 0.5-2, 0.75-2, and 1-3, respectively. This shows that C_3 for 0.5-2 is well consistent to that for 1-3, which shows around 16% greater than that for 0.75-2. Of course, there is also another possibility that 0.75-2 is not the exactly dominant point. Nevertheless, for the dominant points in the vertical section, q_{CHF}

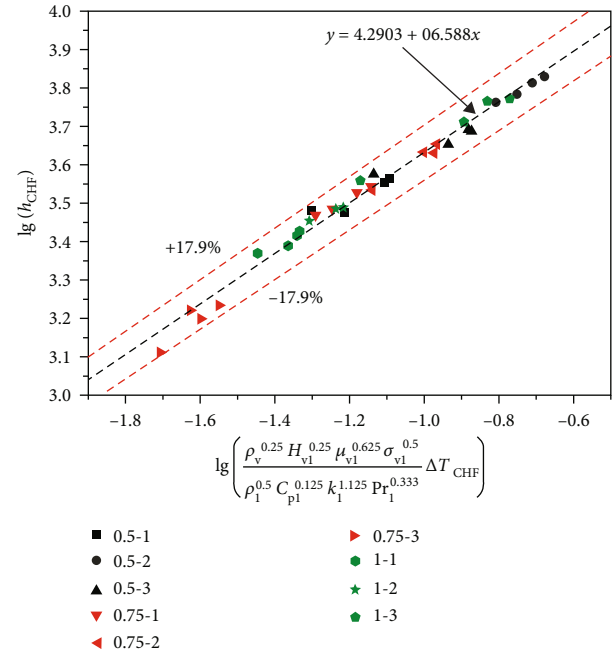

Figure 22: Correlation on h_{CHF} by Equation (17).

could be correlated by Equation (12), in which C_3 could be suggested to be 0.00935, which produces the deviation within ±12%, referring Figure 21.

Correlation format as Equation (12) shows for q_{CHF} is much different from that in the pool boiling, in which q_{CHF} was correlated to be linear versus parameter B as shown in Equation (11) [37]. Equation (12) was approved by the present authors, which represents the effects of bubble size and fluid properties by parameter combination and the effects of L_{se} and circumferential position by C_3 [29]. Figure 21 shows that on the dominant points of the vertical section, q_{CHF} is primarily controlled by bubble size and fluid properties, which are determined primarily by system pressure. In this way, on the vertical section of the present study, q_{CHF} could be well correlated by Equation (12) with the C_3 of 0.00935. Here, previous flow instability theories could not be used here, which has been discussed before [29].

On the other hand, Equation (17) gives good correlations on h_{CHF} for both dominant points and dominated points. With the increase of pressure, all of the parameters including q_{CHF}, ΔT_{CHF}, and h_{CHF} show the overall decreasing manner. In this way, a new parameter combination has been set up referring F-Z equation, as shown in Equation (16), and reliable correlations have been obtained by Equation (17).

5.5.2. Correlation on the Dominated Points. In the current stage, Equation (12) and C_3 listed in Table 4 could be suggested to predict q_{CHF} values for the dominated points. Similar with LFP, on this sort of points, bubble separation is not caused by local flow instability. Result indicates that at t_{CHF}, bubble separation happens on the dominant point of the current cross-section. Almost simultaneously, bubbles are

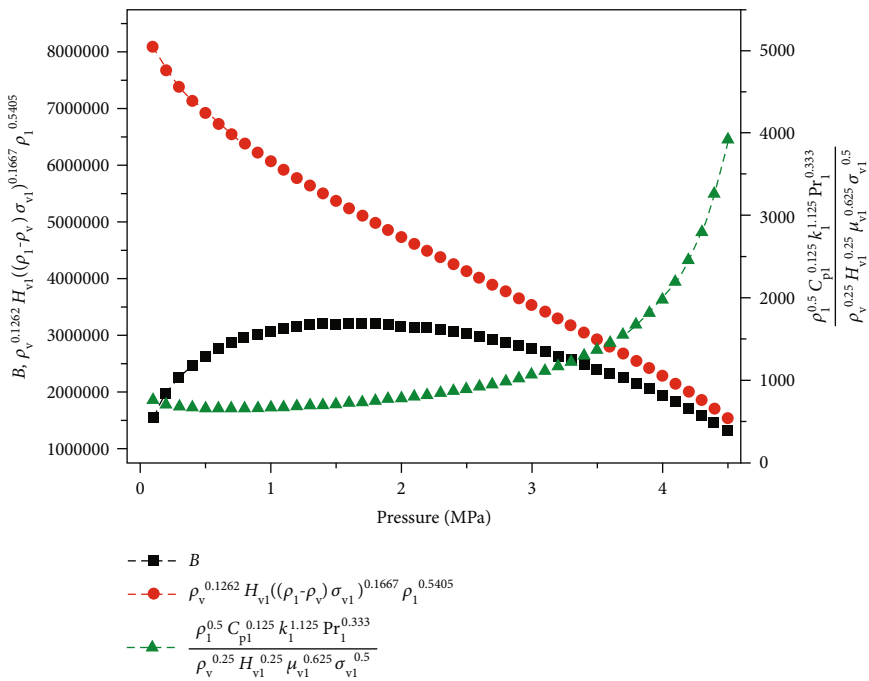

Figure 23: Pressure versus parameter combinations for CHF.

separated from the inner wall on all of this cross-section as a result of bubble separation front propagation circumferentially. In this way, on the dominated points, as a result of being separated, q_i, h_i, and T_i at t_{CHF} have to be denoted as parameters on CHF.

5.5.3. Correlation Formats and Analyses. In the previous studies, q_{CHF} and ΔT_{CHF} were always correlated [8]. However, in the present study, q_{CHF} and h_{CHF} were tried to be correlated instead of ΔT_{CHF}. This is the new correlation approach, similar with LFP. The primary parameter combinations in Equation (11), (12), and (17), used to predict ΔT_{CHF}, q_{CHF}, and h_{CHF}, respectively, could be plotted versus pressure in Figure 23.

As shown in Figure 23, for ΔT_{CHF}, the correlation difficulties are more or less similar to those for ΔT_{LFP}. The key point is the primary parameter combination B in Equation (11) could not represent the effect of pressure.

For q_{CHF}, analysis shows that the effects of pressure and circumferential position should be involved. In the present study, the strategies are similar with those for LFP. For involving the effect of circumferential position, dominant points and dominated points are identified. Results show that q_{CHF} could be well correlated by Equation (12). For three dominant points, C_3 in Equation (12) is approved to be 0.00935, and for dominated points, C_3 in Equation (12) is listed in Table 4. On the other hand, parameter combination in Equation (12) decreases linearly with the increase of pressure as shown in Figure 23. This indicates the effect of pressure, determining bubble size, and fluid properties could be represented well by this correlation.

For h_{CHF}, Equation (17) could be suggested for both dominant points and dominated points. It shows that on the vertical section, it is determined by ΔT_{CHF} and fluid properties, which are dominated by pressure.

6. Conclusion

LO_2 chill-down in a vertical exit-contracted pipe was studied experimentally. Wall temperature was detected in detail (various L_{se} and circumferential position, 1-east, 2-south, and 3-west) to investigate the filling and chill-down process. The filling and chill-down process was described in detail, on which the propagation of quenching front (QF) was detected. Two QFs were found, one for the exit QF and another for the inlet QF. It has been found that the chill-down process is controlled mainly by the formation and propagation of QFs, which are determined by the pressure level. Based on the experimental data, q_{LFP}, h_{LFP}, q_{CHF}, and h_{CHF} were correlated, respectively, for the vertical section. Primary conclusions could be listed as follows.

(1) During LO_2 chill-down process in the vertical exit-contracted pipe, both exit QF and inlet QF are detected. Results show that on most cases, the propagation of the exit QF dominates the liquid rewetting for $L_{se} = 0.5$ m and its downstreams

(2) For both LFP and CHF, circumferential position plays significant roles. On the vertical section, because of the proportions of QF or bubble separation front circumferentially, when LFP or CHF happens on the dominant point, LFP or CHF would happen on the same cross-section (dominated points) in a short period. On the dominant points, LFP is controlled by the flow instability, and CHF is controlled by the bubble size and fluid properties.

However, on the dominated points, both LFP and CHF are determined by the dominant points and heat transfer themselves

(3) Both ΔT_{LFP} and ΔT_{CHF} have not been tried to be correlated. A series of difficulties have been discussed. At first, these two parameters are not independent themselves, and they are both determined by other parameters. On the other hand, the current parameter combinations could not represent the effects of pressure in such a wide range of pressure

(4) Equations (8) and (9), involving the effects of pressure and L_{se} could be suggested to predict q_{LFP}, and h_{LFP} on the dominant points. Equations (2) and (3), with the similar formats with Equations (8) and (9) could be suggested to predict q_{LFP} and h_{LFP} on the dominated points by constant in Table 4

(5) For q_{CHF}, Equation (12) would be suggested, with C_3 of 0.00935 for dominant points and C_3 listed in Table 4 for dominated points. Equation (17) could be strongly suggested to predict h_{CHF} for both sorts of points.

Nomenclature

A: Area, m^2
B: Parameter combination in correlations
C: Constant in correlations
c: Specific heat, $J \cdot kg^{-1} \bullet K^{-1}$
D: Diameter, m
E: Parameter combination in correlations
G: Mass flux in the experimental section, $kg \cdot m^{-2} \bullet s^{-1}$
g: Gravity acceleration, $m \cdot s^{-2}$
H: Latent heat or enthalpy, $J \cdot kg^{-1}$
h: Heat transfer coefficient, $W \cdot m^{-2} \cdot K^{-1}$
k: Heat conductivity, $W \cdot m^{-1} \cdot K^{-1}$, or constant in k_{FZ}
L: Distance, m
$\dot{m}$: Mass flow rate, $kg \cdot s^{-1}$
N: Number of data
P: Pressure, Pa
Pr: Prandtl number, $c_p \cdot \mu \cdot k^{-1}$
q: Heat flux, $W \cdot m^{-2}$
Re: Reynolds number, $D_i G \cdot \mu_l^{-1}$
T: Temperature, K
t: Time, s
u: Velocity, m/s
V: Variables mainly represent T_{LFP}, q_{LFP}, T_{CHF}, and q_{CHF} data.

Subscripts

bu: The bubble
CHF: Critical heat flux point
cr: Critical properties
exp: Experimental data
FZ: Forster-Zuber parameter
FB: Film boiling
i: The inner wall of the pipe
inj: Injector on the pipe exit
LFP: Inner wall data of the Leidenfrost point
l: Liquid phase
NB: Nuclear boiling
o: The outer wall of the pipe
p: Fluid in the experimental section, or constant pressure in c_p
peak: Value of the pressure peak
pre: Predicted data by correlations
s: The solid material
sat: Saturation condition
se: From main valve to outer wall temperature sensors
si: Saturation parameter on inner wall temperature
ss: Steady-state condition, the chill-down finishes
v: Vapor phase
vl: From vapor phase to liquid phase.

Greek Symbols

μ: Viscosity, Pa•s
ρ: Density, $kg \cdot m^{-3}$
σ: Surface tension, $N \cdot m^{-1}$
δ: Thickness of film, m.

Data Availability

Data have been uploaded by "supplemental files" with manuscript file.

Conflicts of Interest

The authors declare that they have no conflicts of interest.

Supplementary Materials

In the "Supplementary files" section, a file named "Data_B," including the LFP and CHF data in the format of table has been uploaded with the manuscript. Related description has been given in the precious section "Data Availability." *(Supplementary Materials)*

References

[1] D. Conte, D. Budzyń, H. Burgoyne et al., "Innovative Mars Global International Exploration (IMaGInE) mission," in *AIAA Space 2016*, Long Beach, California, 2016.

[2] E. A. Hurlbert, R. Whitley, M. D. Kelm et al., "International space exploration coordination group assessment of technology gaps for LOx/methane propulsion systems for the global exploration roadmap," in *AIAA Space 2016*, Long Beach, California, 2016.

[3] H. C. Hansen, W. L. Johnson, M. L. Meyer, A. H. Werkheiser, and J. R. Stephens, "Cryogenic fluid management technologies enabling for the Artemis program and beyond," in *ASCEND 2020*, Virtual Event and Cincinnati, Ohio, 2020.

[4] T. D. Smith, M. D. Klem, and K. L. Fisher, "Propulsion risk reduction activities for non-toxic cryogenic propulsion," in *AIAA SPACE 2010 Conference & Exposition*, Anaheim, California, 2010.

[5] T. Polsgrove, D. Thomas, S. Sutherlin, W. Stephens, and M. Rucker, "Mars ascent vehicle design for human exploration," in *AIAA SPACE 2015 Conference and Exposition*, Pasadena, California, 2015.

[6] J. Collins, E. Hurlbert, K. Romig, J. Melcher, A. Hobson, and P. Eaton, "Sea-level flight demonstration and altitude characterization of a LO2/LCH4 based ascent propulsion lander," in *45th AIAA/ASME/SAE/ASEE Joint Propulsion Conference & Exhibit*, Denver, Colorado, 2009.

[7] S. R. Darr, J. W. Hartwig, J. Dong et al., "Two-phase pipe quenching correlations for liquid nitrogen and liquid hydrogen," *Journal of Heat Transfer*, vol. 141, no. 4, 2019.

[8] J. Zhang, K. Wang, and L. Chen, "Characteristics of boiling transitions during liquid oxygen chill-down in a horizontal pipe with an injector on the exit," *Applied Thermal Engineering*, vol. 182, article 116068, 2021.

[9] J. N. Chung, "Cryogenic two-phase flow and boiling heat transfer during pipe chilldown (invited)," in *37th AIAA Thermophysics Conference*, Portland, Oregon, AIAA, 2004.

[10] K. Yuan, Y. Ji, and J. N. Chung, "Cryogenic boiling and two-phase flow during pipe chilldown in earth and reduced gravity," *Journal of Low Temperature Physics*, vol. 150, no. 1-2, pp. 101–122, 2008.

[11] K. Yuan, Y. Ji, and J. N. Chung, "Cryogenic chilldown process under low flow rates," *International Journal of Heat and Mass Transfer*, vol. 50, no. 19-20, pp. 4011–4022, 2007.

[12] J. Chen, R. Zeng, X. Zhang, L. Qiu, and J. Xie, "Numerical modeling of flow film boiling in cryogenic chilldown process using the AIAD framework," *International Journal of Heat and Mass Transfer*, vol. 124, pp. 269–278, 2018.

[13] H. Hu, T. K. Wijeratne, and J. N. Chung, "Two-phase flow and heat transfer during chilldown of a simulated flexible metal hose using liquid nitrogen," *Journal of Low Temperature Physics*, vol. 174, no. 5-6, pp. 247–268, 2014.

[14] R. Shaeffer, H. Hu, and J. N. Chung, "An experimental study on liquid nitrogen pipe chilldown and heat transfer with pulse flows," *International Journal of Heat and Mass Transfer*, vol. 67, pp. 955–966, 2013.

[15] S. R. Darr, H. Hu, N. G. Glikin et al., "An experimental study on terrestrial cryogenic transfer line chilldown I. Effect of mass flux, equilibrium quality, and inlet subcooling," *International Journal of Heat and Mass Transfer*, vol. 103, pp. 1225–1242, 2016.

[16] S. R. Darr, H. Hu, N. G. Glikin et al., "An experimental study on terrestrial cryogenic tube chilldown II. Effect of flow direction with respect to gravity and new correlation set," *International Journal of Heat and Mass Transfer*, vol. 103, pp. 1243–1260, 2016.

[17] L. Jin, C. Park, H. Cho, C. Lee, and S. Jeong, "Experimental investigation on chill-down process of cryogenic flow line," *Cryogenics*, vol. 79, pp. 96–105, 2016.

[18] L. Jin, H. Cho, C. Lee, and S. Jeong, "Experimental research and numerical simulation on cryogenic line chill-down process," *Cryogenics*, vol. 89, pp. 42–52, 2018.

[19] L. Jin, H. Cho, and S. Jeong, "Experimental investigation on line chill-down process by liquid argon," *Cryogenics*, vol. 97, pp. 31–39, 2019.

[20] L. Jin, J. Lee, and S. Jeong, "Investigation on heat transfer in line chill-down process with various cryogenic fluids," *International Journal of Heat and Mass Transfer*, vol. 150, article 119204, 2020.

[21] J. Johnson and S. R. Shine, "Transient cryogenic chill down process in horizontal and inclined pipes," *Cryogenics*, vol. 71, pp. 7–17, 2015.

[22] J. Wang, Y. Li, L. Wang, K. Zhu, F. Xie, and C. Li, "Transient modeling of cryogenic two-phase flow boiling during chill-down process," *Applied Thermal Engineering*, vol. 143, pp. 461–471, 2018.

[23] A. C. LeClair, J. W. Hartwig, D. M. Hauser, M. Kassemi, P. G. Díaz-Hyland, and T. R. Going, "Modeling cryogenic chilldown of a transfer line with the generalized fluid system simulation program," in *2018 Joint propulsion conference*, p. 4756, Virtual Event and Cincinnati, Ohio, 2018.

[24] J. C. Melcher and R. L. Morehead, "Combustion stability characteristics of the project morpheus liquid oxygen/liquid methane main enginE," in *50th AIAA/ASME/SAE/ASEE Joint Propulsion Conference*, Cleveland, OH, 2014.

[25] P. Cui, Q. Li, P. Cheng, and L. Chen, "System scheme design for LOX/LCH4 variable thrust liquid rocket engines using motor pump," *Acta Astronautica*, vol. 171, pp. 139–150, 2020.

[26] R. L. Morehead, J. C. Melcher, M. J. Atwell, E. A. Hurlbert, and P. Desai, "Vehicle-level oxygen/methane propulsion system hotfire demonstration at thermal vacuum conditions," in *53rd AIAA/SAE/ASEE Joint Propulsion Conference*, Atlanta, GA, 2017.

[27] N. Cho, S. Kim, Y. Kim, and S. J. J. Jung, "Two-phase flow characteristics of liquid oxygen flow in low pressure liquid rocket engine," *Cryogenics*, vol. 44, no. 6-8, pp. 493–500, 2004.

[28] J. Zhang, K. Wang, and L. Chen, "Experimental study on liquid oxygen chilldown in the horizontal pipe with an injector on the exit," *Applied Thermal Engineering*, vol. 173, article 115212, 2020.

[29] J. Zhang, K. Wang, and L. Chen, "Experimental study on liquid oxygen chill-down in a horizontal exit-contracted pipe," *Cryogenics*, vol. 120, article 103387, 2021.

[30] H. Hong, N. Jacob, A. Chung, and S. H. Amber, "An experimental study on flow patterns and heat transfer characteristics during cryogenic chilldown in a vertical pipe," *Cryogenics*, vol. 52, no. 4-6, pp. 268–277, 2012.

[31] J. Hartwig, S. Darr, and A. Asencio, "Assessment of existing two phase heat transfer coefficient and critical heat flux correlations for cryogenic flow boiling in pipe quenching experiments," *International Journal of Heat and Mass Transfer*, vol. 93, pp. 441–463, 2016.

[32] N. Zuber, M. Tribus, and J. W. West, "The hydrodynamic crisis in pool boiling of saturated and subcooled liquid," *International Development in HEAT Transfer*, pp. 230–236, 1961.

[33] P. J. Berenson, "Film-boiling heat transfer from a horizontal surface," *Journal of Heat Transfer*, vol. 83, no. 3, pp. 351–356, 1961.

[34] Y. Katto and C. Kurata, "Critical heat flux of saturated convective boiling on uniformly heated plates in a parallel flow," *International Journal of Multiphase Flow*, vol. 6, no. 6, pp. 575–582, 1980.

[35] J. J. Carbajo, "A study on the rewetting temperature," *Nuclear Engineering and Design*, vol. 84, no. 1, pp. 21–52, 1985.

[36] H. K. Forster and N. Zuber, "Dynamics of vapor bubbles and boiling heat transfer," *AICHE Journal*, vol. 1, no. 4, pp. 531–535, 1955.

[37] N. Zuber, "Nucleate boiling. The region of isolated bubbles and the similarity with natural convection," *International Journal of Heat and Mass Transfer*, vol. 6, no. 1, pp. 53–78, 1963.